Development and Characterization of Catalytic Systems for Biomass-Derived Chemical Feedstocks

Thesis by

Marat Orazov

In Partial Fulfillment of the Requirements
for the Degree of
Doctor of Philosophy

CALIFORNIA INSTITUTE OF TECHNOLOGY
Pasadena, California

2017
(Defended July 15, 2016)

ACKNOWLEDGEMENTS

The tremendous opportunity to study at Caltech and the completion of the works presented here would not have been possible without the various contributions from the outstanding mentors, collaborators, friends, and family who have shaped and influenced me as a person and a scientist.

First, I would like to express my deep gratitude to my advisor, Professor Mark E. Davis, for the privilege of working and learning under his guidance. In addition to his kind support and encouragements that have only grown from our first interactions, I value his far-reaching perspective in science and life, as well as his tendency to foster independence and uniqueness of thought – all qualities that have made him a consistently great mentor.

Additionally, I thank my undergraduate mentors at UC Berkeley, Professors Alexander Katz and David B. Graves, for their willingness to take me into their groups, thereby starting my research career. In doing so, they invested valuable personal time and resources into my development – the benefits of which I continue to cherish. Their encouragements to apply to top graduate programs, and specifically Professor Katz's advice regarding his experience as an alumnus of the Davis group, have brought me to Caltech.

At Caltech, I would like to further thank the members of my thesis committee: Dr. Jay A. Labinger, Professor Richard C. Flagan, and Professor Theodor Agapie. I have benefited from the various academic and social interactions we have had over the years. I am also thankful for the various experts around Caltech that have assisted in acquiring and/or interpreting data: Dr. Sonjong Hwang for Solid State NMR, Dr. David VanderVelde for liquid NMR, Dr. Chi Ma for SEM/EDS, and Dr. Mona Shahgholi for MS. I thank the Chemical Engineering staff that have been exceptionally helpful: Kathy, Martha, and Suresh.

Within the Davis group I would like to thank its current members and alumni that I have gotten to interact with during my time here. I am especially grateful to Raj and Ricardo for all of their help and advice in sugar and Lewis acid chemistries, and for our collaboration that resulted in my first publication with the group. Also, I explicitly thank the other senior lab members that trained me on various instruments and techniques: Bingjun, Joel, Josh, and Mark. A special thanks goes to Kramer for his valuable help and discussions regarding experiments and beyond, and to Ben and Michiel for their unique scientific perspectives. Finally, I thank all of the aforementioned and remaining group members (and a number of Caltech friends outside of lab) for their friendship and fun times shared.

I thank many people outside of Caltech for enriching collaborations or valuable advice regarding science and my career: Dr. Stacey I. Zones, Professor Michael Tsapatsis and members of his group (especially Dr. Limin Ren), Professors Abraham M. Lenhoff, Dionisios G. Vlachos, Raul F. Lobo, and Yushan Yan, and various members of the CCEI.

Most importantly, I would like to thank my family: my parents, for all of their love, upbringing, and emotional and tangible support; my brother, for setting a good example and for help throughout the years.

ABSTRACT

Heterogeneous catalysis by Brønsted and/or Lewis acid sites isolated within microporous environments is a topic that is perpetually growing in scope and importance. While Brønsted acid sites in zeolites have been studied and applied extensively in the petrochemical industry, new opportunities for green processes based on renewable chemical feedstocks call for applications of new microporous materials that possess Lewis acid sites (e.g., zeotypes with framework Sn, Ti, Zr, or Hf). Characterization of such materials and the specific structures of the Lewis acid sites provides insights for rational catalyst design and application.

This work provides experimental evidence for the identities of the active sites in Sn-Beta zeotype for the 1,2-intramolecular hydride shift (1,2-HS) reaction that results in D-glucose isomerization to D-fructose, and for the 1,2-intramolecular carbon shift (1,2-CS) reaction that results in D-glucose isomerization to D-mannose. Specifically, by selective poisoning experiments, the partially-hydrolyzed, "open" Sn site is shown to be the active site for the 1,2-HS reaction. The participation of the proximal silanol of such an open Sn site in the 1,2-HS reaction is demonstrated thorough alkali-exchange experiments. Such experiments also reveal that the active site for the 1,2-CS reaction is an open Sn site with a cation-exchanged proximal silanol.

1,2-CS catalysts, in general, are shown to also catalyze retro-aldol reactions of hexoses at moderate temperatures (ca. 100 °C), and to be compatible with microporous 1,2-HS catalysts in tandem catalytic schemes that enable production of alkyl lactates.

Finally, the Lewis acidity of framework Zn in zincosilicate microporous materials is demonstrated through probe-molecule infrared spectroscopy. One such material is then shown to catalyze Diels-Alder cycloaddition-dehydration reactions of oxygenated furans and

ethylene. To the best of our knowledge, these materials are the first heterogeneous catalysts reported to catalyze the direct formation of terephthalate esters from ethylene and dimethyl 2,5-furandicarboxylate with appreciable selectivity.

PUBLISHED CONTENT AND CONTRIBUTIONS

The contents of the following publications were used as the basis for Chapters 2-4 of this thesis:

Basis for Chapter 2:

Bermejo-Deval, R.***; Orazov, M.***; Gounder, R.; Hwang, S.; Davis, M. E. "Active Sites in Sn-Beta for Glucose Isomerization to Fructose and Epimerization to Mannose" *ACS Catal.*, **2014**, *4*, 2288–2297. DOI: 10.1021/cs500466j

***Equal author contribution**

Role: M.O. and R.B.D. made equal contributions, namely, both participated equally in the design of research, execution of research, analysis of data, and the writing of the manuscript

Basis for Chapter 3:

Orazov, M.; Davis, M. E. "Tandem catalysis for the production of alkyl lactates from ketohexoses at moderate temperatures" *Proc. Natl. Acad. Sci. USA*, **2015**, *112*, 11777–11782. DOI: 10.1073/pnas.1516466112

Role: M.O. and M.E.D. designed research; M.O. performed research; M.O. and M.E.D. analyzed data; and M.O. and M.E.D. wrote the paper.

Basis for Chapter 4:

Orazov, M.; Davis, M. E. "Catalysis by framework zinc in silica-based molecular sieves" *Chem. Sci.* **2016**, *7*, 2264–2274. DOI: 10.1039/C5SC03889H

Role: M.O. and M.E.D. designed research; M.O. performed research; M.O. and M.E.D. analyzed data; and M.O. and M.E.D. wrote the paper.

The contents of the following publications were **NOT** used directly in this thesis:

Ren, L.; Guo, Q.; **Orazov, M.**; Xu, D.; Politi, D.; Kumar, P.; Alhassan, S. M.; Mkhoyan, K. A Sidiras, D.; Davis, M. E.; Tsapatsis, M "Pillared Sn-MWW prepared by solid-state-exchange method and its use as a Lewis-acid catalyst" *ChemCatChem*, **2016**, *8*, 1867-3899.

DOI: 10.1002/cctc.201600120

Ren, L.; Guo, Q.; Kumar, P.; **Orazov, M.**; Xu, D.; Alhassan, S. M.; Mkhoyan, K. A.; Davis M. E.; Tsapatsis, M. "Self-Pillared, Single-Unit-Cell Sn-MFI Zeolite Nanosheets and Their Use for Glucose and Lactose Isomerization" *Angew. Chemie Int. Ed.*, **2015**, 54, 10848-10851.

DOI:10.1002/anie.201505334

Hwang, S.-J.; Gounder, R.; Bhawe, Y.; **Orazov, M.**; Bermejo-Deval, R.; Davis, M. E. "Solid State NMR Characterization of Sn-Beta Zeolites that Catalyze Glucose Isomerization and Epimerization" *Top. Catal.*, **2015**, *58*, 435-440.

DOI: 10.1007/s11244-015-0388-7

TABLE OF CONTENTS

LIST OF FIGURES

Number *Page*

LIST OF TABLES

Chapter 1

Introduction to Catalytic Systems Relevant to Biomass Processing

This chapter introduces some of the motivations, challenges, and approaches in the endeavor of producing chemicals from biomass feedstocks. Various statistics for U.S. industries are used to get a sense of scales. Finally, contributions to the development and characterization of catalytic systems discussed in the remainder of this thesis are briefly outlined.

1.1 Motivation for biomass feedstocks in chemical industries

Fossil fuel resources (coal, natural gas, and oil) have been the dominant sources of energy and organic matter during the industrialization of the world in the last century.[1–3] However, environmental concerns associated with fossil fuel extraction and usage, including emission of greenhouse gasses and pollution of air, water, and land have motivated significant efforts to transition towards renewable and sustainable resources.[2] The U.S. Energy Information Administration reports that, in 2015, coal, natural gas, and oil constituted 16%, 29%, and 36% of the U.S. energy consumption, respectively.[3,4] Though solar and wind energy generation has grown substantially over the past decade, unless significant increases in oil and gas prices occur, projections for energy consumption over the next 25 years suggest that fossil fuels will remain as the primary source of energy.[1,3]

Outside of transportation fuels, 3% of natural gas and 7% of oil consumed in the U.S. are used as chemical feedstocks.[5] The processing of these feedstocks to chemicals of interest incurs an additional energy expenditure roughly equivalent in magnitude to that contained in the feedstocks.[5] Inherently, for the chemical industry to be viable, the economic value of products based on these feedstocks must exceed the value of their energy content. The environmental benefit of the replacement of fossil-fuel-based chemical feedstocks with renewable alternatives may not be insignificant, but the energy and transportation industries arguably have much bigger potential roles in addressing these concerns. Nevertheless, academia and industry remain interested in developing processes that rely on non-fossil fuel feedstocks for the chemical industry, motivated by the possibility of positive environmental impact and economic advantages over the conventional.[2,6–8] Specifically, production of oxygenated or functionally complex molecules from biomass may be economically more viable than from hydrocarbons, and result in net greener processes.

1.2 Biomass composition and availability

The majority of terrestrial biomass is lignocellulosic, consisting of lignin, cellulose, and hemicellulose.[2] Lignin is a complex, heterogeneous polymer of crosslinked aromatics, with typical monomers being paracoumaryl, coniferyl, and sinapyl alcohols (Fig. 1.1).[9,10] These monomers are polymerized through C-O-C and C-C linkages that are difficult to cleave, requiring high temperature hydrogenolysis.[11] Cellulose is a polymer of glucose (Fig. 1.2) that has a varying degree of crystallinity.[2] Glucose in cellulose is linked through glycosidic β-(1→4) bonds that make it much easier to depolymerize than lignin.[2] Depolymerization by

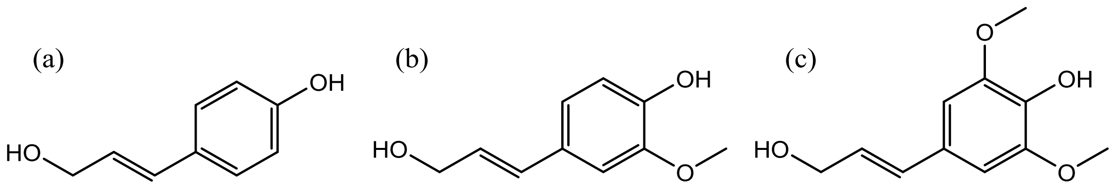

Figure 1.1 The three common monomers of lignin: (a) paracoumaryl, (b) coniferyl, and (c) sinapyl alcohols.

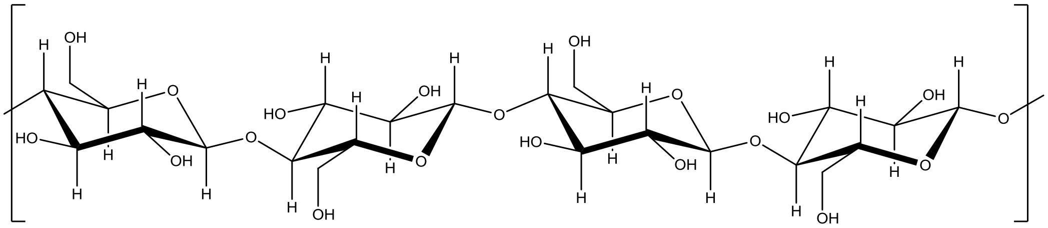

Figure 1.2 Structure of cellulose. Glycosidic β-(1→4) bonds link glucose monomers in a linear chain (which allows for facile crystallization), and dangling –OH groups contribute to intra- and inter-strand hydrogen bonding.

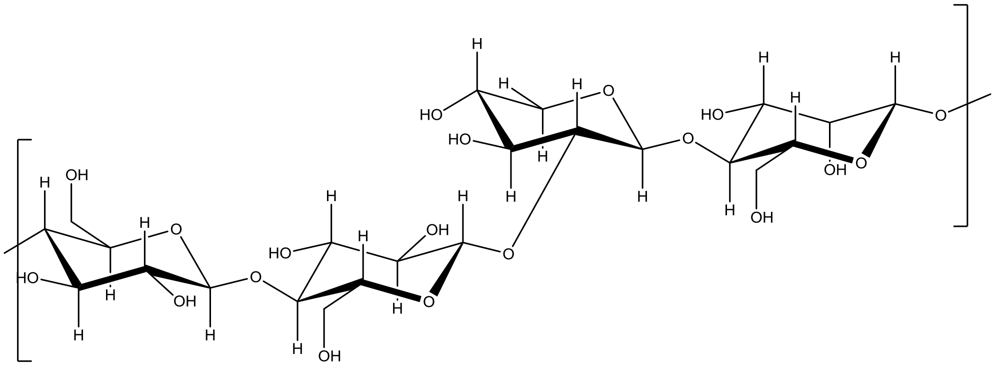

Figure 1.3 A possible structure of a hemicellulose segment. Glycosidic (1→3) bonds, and monomeric isomers disrupt the regularity of structure that is found in glucose, preventing crystallization.

hydrolysis of the glycosidic bonds can be implemented with enzymatic systems or with mineral acids; susceptibility to hydrolysis increases with decrease in crystallinity of cellulose.[6] Hemicellulose is a random, mixed polymer of hexose and pentose monosaccharides, also linked through glycosidic bonds, but not exclusively in β-(1→4) configuration (Fig 1.3).[2,12] Unlike cellulose, due to its irregular structure, hemicellulose does not crystallize and is easier to solubilize and hydrolyze.[2] The composition of lignocellulosic biomass varies depending on the source, but the typical ranges are 15-30 wt% lignin, 30-50 wt% cellulose, 20-30 wt% hemicellulose.[2] Because polysaccharides are more abundant and more easily processed into monomers than lignin, saccharide monomers have been the substrates of choice in this work. However, recent advances in lignin hydrogenolysis have made lignin depolymerization products a topic of renewed interest in various laboratories.[11,13]

Oak Ridge National Laboratory (ORNL) estimates that the U.S. has the potential to annually produce on the order of 10^9 tons of dry terrestrial lignocellulosic biomass, without compromising productivity of agriculture for food and livestock feed.[2,6,14] For such production capacity, the farmgate price (i.e., all costs excluding transportation from farm) is estimated to range from $40 to $60 per dry ton.[14] In comparison, in 2015, the total U.S. consumption of oil and natural gas was also on the order of 10^9 tons, each.[4] The specific energy density of dry biomass is approximately 35% of oil and natural gas.[14] Thus, the projected annual production of biomass cannot meet even the current energy demand associated with fossil fuels, let alone its projected growth.[3] However, a naive analysis based on carbon content of such biomass (ca. 50 wt%) suggests that this capacity exceeds the current total carbon demand in chemical feeds by an order of magnitude.[2] Similarly, a naive analysis of the cost per mass of carbon indicates that the carbon in such biomass is an order of magnitude less expensive than in oil. These simple calculations ignore the costs and energy expenditures of long distance transportation costs, as well as utilization efficiency. Extensive economic analyses of various feedstocks and target molecules exist and provide more reasonable estimates on feasibility of biomass-derived chemicals. For instance, Pacific Northwest National Laboratory (PNNL) and National Renewable Energy Laboratory (NREL) have published their analyses and recommendations of compounds that can be derived from both the lignin and the polysaccharide components of biomass, and hold potential as platforms for the chemical industry.[15,16] The conclusions from these and other reviews suggest a potential for economic viability of processes targeting high-value molecules that do not require extensive reduction, and have functional complexity comparable to the monomers.[8,15,16] The following discussion will focus on a small selection of such products that are relevant to chemocatalytic chemistries studied in this work.

1.3 A selection of target molecules

The vast majority of monomers in biomass are hexoses and pentoses. However, only a few of the possible enantiomers of hexoses and pentoses are abundant. D-glucose is the exclusive monomer of cellulose, which makes it is the most abundant hexose. In addition to D-glucose, hemicelluloses contain variable amounts of the hexose isomers D-mannose and D-galactose.[12] D-Xylose and D-arabinose are the most abundant pentoses found in hemicellulose, though other pentoses are found in trace quantities.[12] While this relative homogeneity of isomerism is advantageous for process design, it also limits access to potentially interesting chemicals. Many of the rare sugars (i.e., those not readily isolable from biomass) have exorbitant prices and low volumetric availability because they are produced through costly many-step reaction-separation chemical synthesis sequences or through fermentative routes.[17,18] These rare sugars have direct applications in various biological research areas, and hold potential as important precursors to pharmaceuticals.[17,18] Thus, selective and inexpensive chemocatalytic systems for sugar isomerization have the potential to make these high-value sugars more widely accessible.

All of the abundant sugars in lignocellulose are aldoses, i.e., sugars with carbonyl groups at the C1 position. Ketoses are an important class of isomers that have the carbonyl group located at a non-terminal carbon position; 2-ketoses are most common and stable. Fructose is a well-known food additive, and is produced from starch-derived glucose in the largest immobilized enzymatic process in the world.[19–21] However, the pretreatment of the lower-purity, lignocellulose-derived hydrolysate that is required for compatibility with the enzymatic catalyst makes the upscaling of fructose production costly. Furthermore, high temperatures (ca. 100 °C) result in more favorable equilibrium distributions of the isomerization reaction, but are incompatible with current enzymes.[20] Thus, robust and inexpensive aldose-ketose isomerization catalysts are required to make the economics more favorable for this route of biomass processing.

Inexpensive routes to ketoses are also required for selective dehydration pathways to furans. Furans are heterocyclic aromatic compounds that have been identified as a group of platform chemicals; i.e., feasible routes to many industrially relevant compounds from furans exist.[15,22] One potential area of application for furans is in plastics. Furanic monomers, especially 2,5-furandicarboxylic acid (FDCA), have been proposed as substitutes for arenes, but the transformation of furans to arenes is also an area of active research.[23–25]

Finally, because the polysaccharides in lignocellulosic biomass are made of C_5 and C_6 monomers, selective catalytic routes to carbon chain elongation or cleavage would greatly expand the number of accessible industrially-relevant products.[6–8] Many commodity chemicals fall in the range of C_2-C_4 products. Highly functionalized small molecules, such as α-hydroxy carboxylic acids, are particularly attractive targets from biomass. Lactic acid, a C_3 α-hydroxy carboxylic acid, is also viewed as a platform molecule, with potential in green polymers and solvents, and as a precursor to specialty chemicals.[6–8] Currently, the primary industrial route to lactic acid is through fermentation of glucose derived by hydrolysis of starch.[6] Developments of chemocatalytic routes from biomass has the potential to significantly lower the costs and improve the sustainability of the process. Such improvements may make lactic acid a more attractive substitute for some of the existing petrochemical based platforms. A summary of potential products is provided in Fig. 1.4.

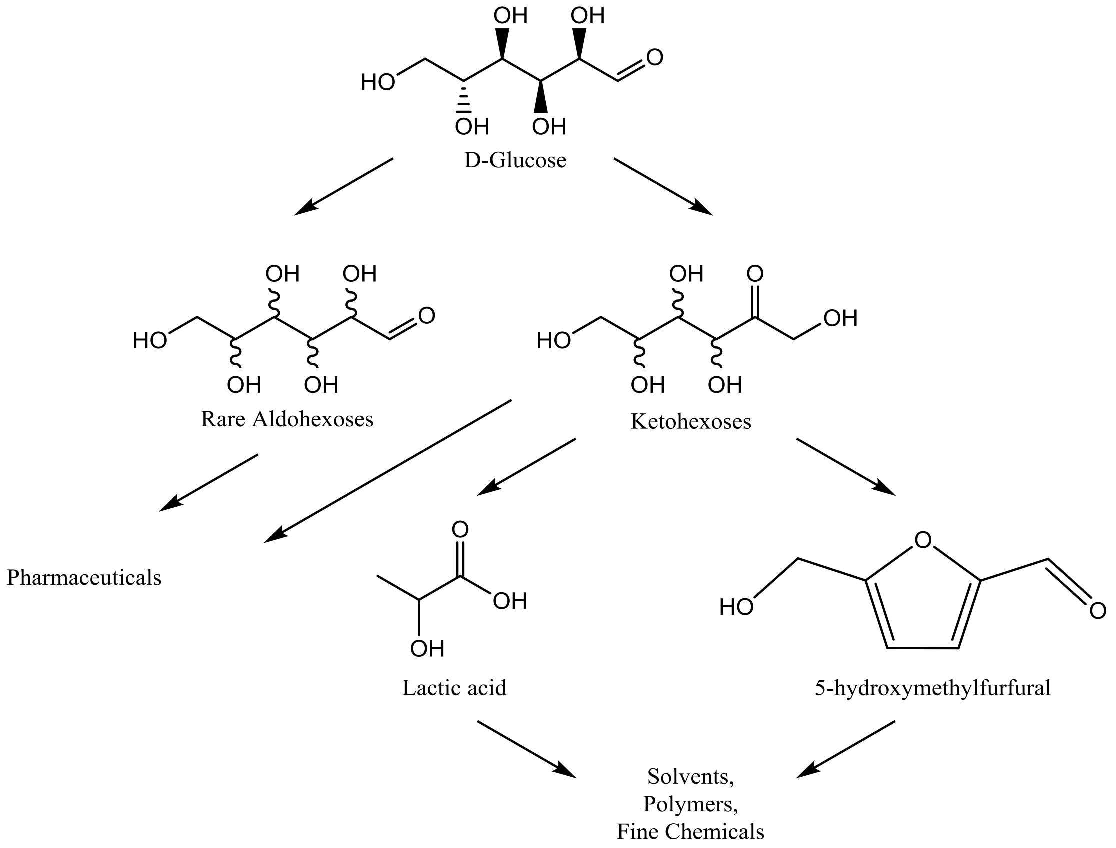

Figure 1.4 A non-comprehensive illustration of some of the feasible and desirable products attainable from glucose. Analogous diagrams exist for other, minor saccharides.

1.4 Reactions of interest and catalytic precedence

In order to make the production of chemicals discussed in Section 1.3 accessible, a number of chemocatalytic systems need to be improved or developed.

Saccharides can be isomerized through various mechanisms. For instance, aldose-ketose interconversion can proceed through enolate intermediates, when proton abstraction from the α-carbon is catalyzed by bases, also known as the Lobry de Bruyn–Alberda–van Ekenstein transformation (Fig 1.5).[26] Both homogeneous inorganic bases such as NaOH, as well as heterogeneous basic or amphoteric oxides such as SnO_2, can promote this reaction pathway, as evidenced by experiments tracking backbone H/D scrambling in isotopically enriched substrates or solvents.[19,27] Alternatively, the same isomerization can proceed through a formal 1,2-intramolecular hydride shift (1,2-HS), when the carbonyl is activated through an interaction with a Lewis acid.[19] This reaction mechanism is conceptually a Meerwein-Ponndorf-Verley reduction of the saccharide's carbonyl and the concerted Oppenauer oxidation of the adjacent alcohol group (MPVO).[28] Interestingly, as the name suggest, this MPVO process proceeds through a backbone migration of the hydrogen or deuterium

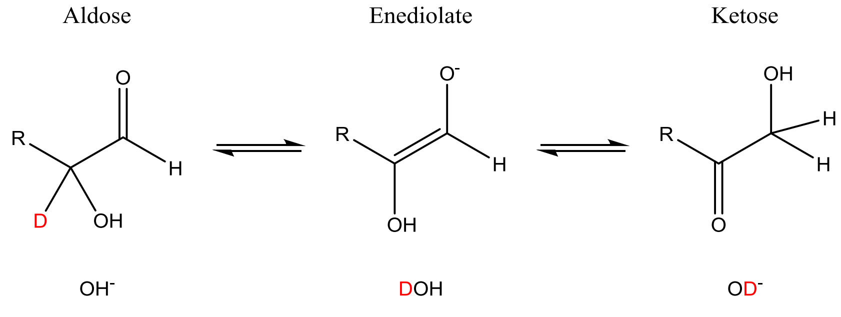

Figure 1.5 An illustration of the base-catalyzed Lobry de Bruyn–Alberda–van Ekenstein transformation that proceeds through an enediolate intermediate and results in isotopic H/D scrambling with the solvent.

attached to the carbonyl's α-carbon, as evidenced by the lack of H/D scrambling in isotopically enriched substrates or solvents (Fig. 1.6).[19] While some homogeneous Lewis acidic metal salts have been reported to catalyze aldose-ketose isomerization through the 1,2-HS route, most such reports deal with smaller sugars (e.g., trioses).[29] Heterogeneous molecular sieves with framework Lewis acid sites, such as Sn-Beta, are able to catalyze these reactions more selectively, with hexose substrates, and in aqueous solutions.[20] The latter class of catalysts will be discussed further in Section 1.5.

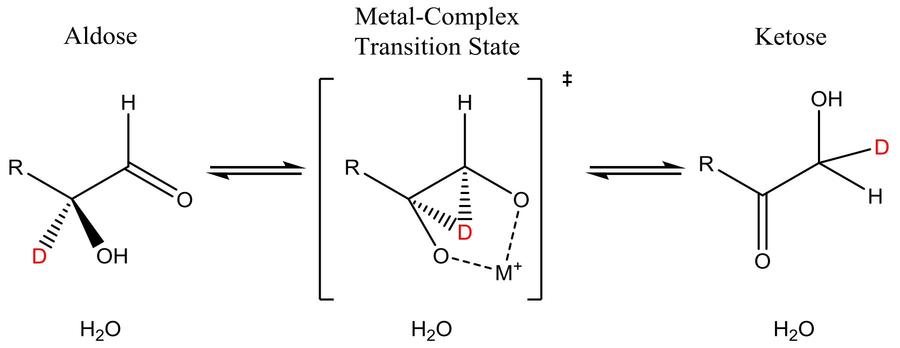

Figure 1.6 An illustration of a Lewis-acidic metal cation catalyzed 1,2-HS process that results in no H/D isotopic scrambling with the solvent.

Aldoses can also be isomerized into their epimers (epimerized) by 1,2-intramolecular carbon shift (1,2-CS) catalysts (e.g., molybdates and Ni (II) diamine complexes), while ketoses can be isomerized into branched sugars by the same catalysts.[26,30] These 1,2-CS reactions (also known as Bílik reactions) are believed to proceed through a mechanism that is conceptually similar to 1,2-HS reactions, but instead of a migrating hydrogen, the process involves the migration of the molecular fragment associated with the carbonyl's β-carbon (Fig 1.7).[30] The 1,2-CS mechanism is experimentally evidenced by product selectivities, and

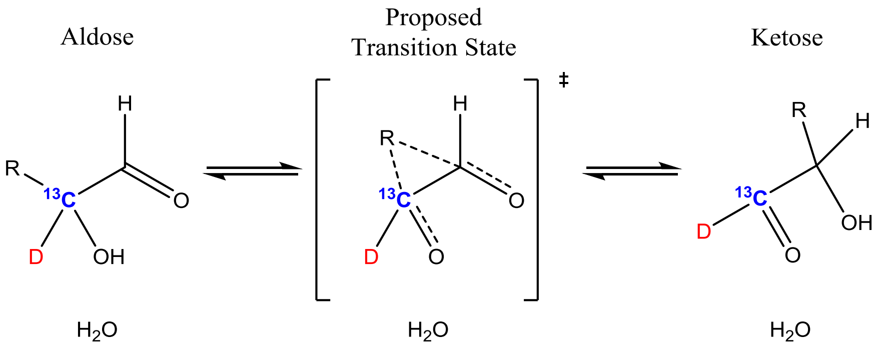

Figure 1.7 An illustration of the proposed pathway for 1,2-CS reaction that results in the migration of a carbon chain, rather than of H atom.

by tracking the position of a ^{13}C label.[27,30] Though there is no general consensus on the exact mode of activation for 1,2-CS catalysis, it appears that tri- or tetra-dentate interactions are common among the known catalysts.[30] Interestingly, in contrast to the 1,2-HS catalyzed in aqueous solutions, in alcoholic solutions some samples of Sn-Beta were reported to catalyze the 1,2-CS of glucose.[27] This anomalous behavior has prompted a further study of this reaction, and will be a topic of subsequent discussion in this thesis.

The aldol reaction of two carbonyl-bearing substrates results in C-C bond formation, leading to carbon chain elongation (Fig. 1.8).[31] Unsurprisingly, its reverse, the retro-aldol reaction, results in C-C bond cleavage and can occur if a carbonyl's β-carbon bears an alcohol group, as is the case with saccharides. Two classes of enzymes have evolved for these reversible reaction: class I aldolases activate the substrate with a primary amine residue by forming a Schiff base adduct (Fig 1.9a), while class II aldolases activate it with a Lewis-acid-induced polarization of the carbonyl (Fig 1.9b).[31] Proximal basic or acidic residues also facilitate the reactions through proton abstraction and shuttling.[31] Though the primary interactions of such enzymes may be emulated by synthetic catalysts, e.g., Lewis acid sites

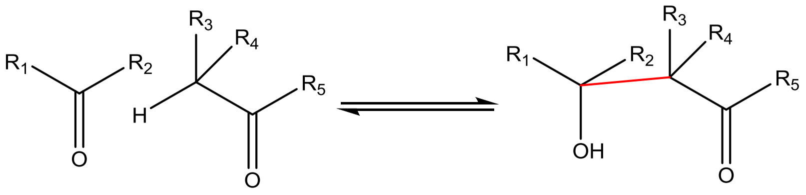

Figure 1.8 Generalized schematic of aldol/retro-aldol reactions.

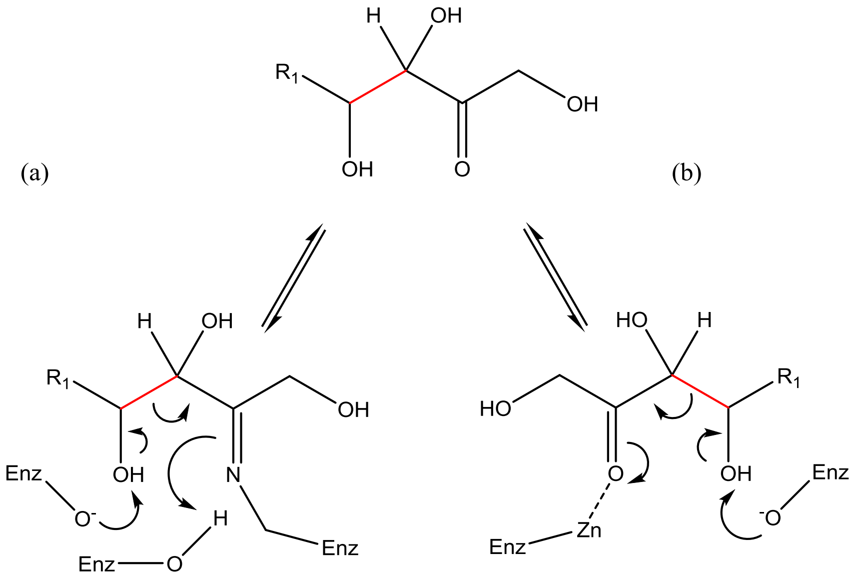

Figure 1.9 Activation of ketoses by (a) class I enzymes happens through the formation of a Schiff base, while (b) class II enzymes polarize the carbonyl through a Lewis acid-base interaction.

in molecular sieves polarizing the carbonyl of fructose, very low rates of retro-aldol reactions are observed with such catalysts and ketohexoses at temperatures as high as 100 °C.[32] Instead, most attempts to produce lactates from hexoses are performed at very high temperatures (160-200 °C) that lead to catalyst deactivation due to deposition of humins (insoluble polymers of dehydration products) on the catalyst.[33–35] Thus, while the isomerization reactions and retro-aldol reactions have some conceptual similarity, they may require slightly different approaches.

The aforementioned ketoses are also more readily dehydrated into furans by Brønsted acids than their aldose isomers.[21,36] Among the advantages of heterogeneous Lewis acid catalysts for the aldose-ketose isomerization is their compatibility with Brønsted acid catalysts. Tandem catalytic schemes based on this pairing allow for efficient production of furans directly from glucose, and potentially from polysaccharides.[21,36] While there are many applications for furans, their capacity to function as dienes and undergo Diels-Alder (DA) addition reactions with olefinic reactants (e.g., ethylene) is particularly interesting (Fig. 1.10a).[37] The resulting oxabicyclo-adducts can be aromatized into the corresponding arenes via dehydration (Fig. 1.10b).[37] The extent of catalytic involvement in the two steps depends on the structure of the diene and dienophile, but both Brønsted and Lewis acids have the potential to catalyze the net cycloaddition-dehydration chemistry.[37] DA reactions will be discussed in greater detail in Chapter 4 of this thesis, but it is important to note here that oxygenated side groups on the furan ring appear to inhibit or slow the reactions.[38] Thus, one of the strategies to facilitate such reactions is to hydrogenate the side-groups into methyl

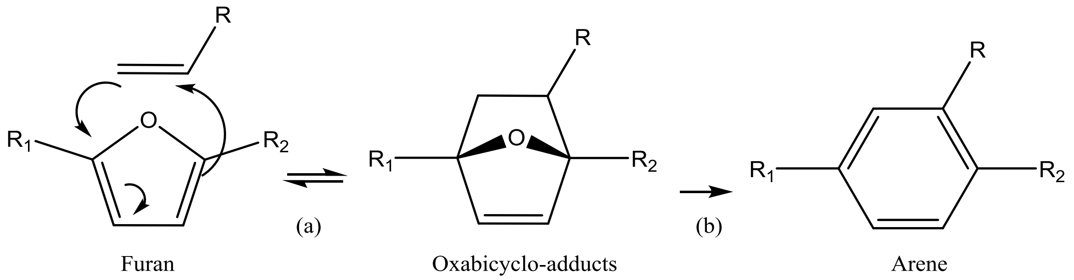

Figure 1.10 A generalized depiction of Diels-Alder (a) cycloaddition and (b) dehydrative-aromatization reactions between a furan (diene) and an olefin (dienophile).

groups.[25] While this strategy is attractive if the end-product is an alkylated arene, products with oxygenated side groups (e.g., terephthalic acid) would require subsequent re-oxidation of the substrate. From an industrial standpoint, oxidation processes already exist (and are the basis of terephthalic acid production from fossil-fuel-based p-xylene), so they are technically feasible.[38] However, such an approach is sub-optimal, as it results in wasted hydrogen, and two additional costly reaction (and potentially separation) steps. To circumvent these issues, past research in the Davis group has investigated the feasibility of DA cycloaddition-dehydration reactions of furans bearing oxygenated side-groups.[23,24,38] The results of this work suggested that certain furans with partially-oxidized side groups could be reacted with high selectivity with the Lewis-acidic Zr-Beta molecular sieves.[23] However, 2,5-furandicarboxylic acid, the furan whose DA cycloaddition-dehydration reactions would lead directly to terephthalic acid, was shown to not react with such catalyst, creating incentive for further exploration of this reaction system.[23,38]

1.5 Molecular sieve catalysts

Molecular sieves constitute an important class of materials that possess regular pore structures, with pore diameters comparable to molecular dimensions, enabling the possibility to sieve based on molecular size and/or shape.[39,40] One subset of molecular sieves is zeolites, crystalline aluminosilicates with pores that typically fall in the range of micropores (less than 2 nm in diameter).[39,40] The structure of zeolites can be understood in terms of the arrangement of SiO_4 tetrahedral building blocks.[39] These units connect in a variety of orientations, forming rings that define the pore systems. In zeolite literature pore dimensions are often discussed in terms of the number of such tetrahedral units (or members) in the narrowest ring of a pore. For instance, the MFI structure is referred to as a 10-membered- ring (MR) material, while

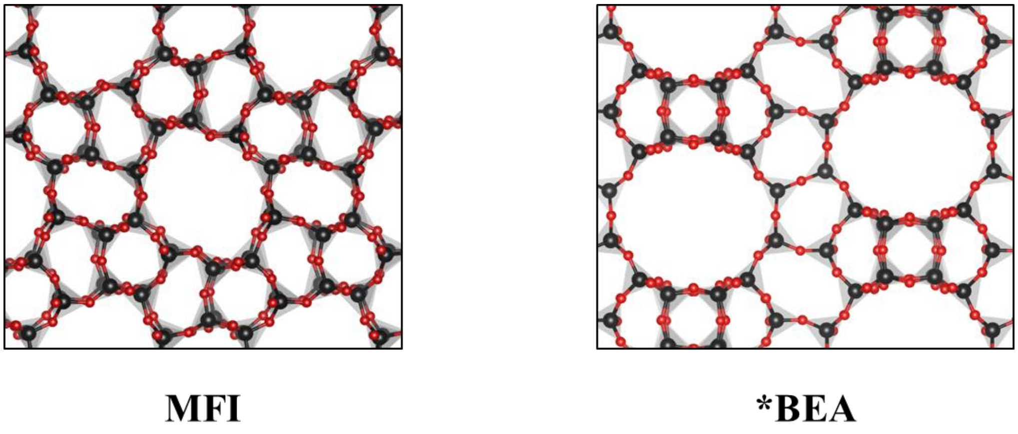

Figure 1.11 Illustration of cross-sections of MFI (10-MR) and *BEA (12-MR) zeolite structures.

the *BEA structure is a member of the 12-MR family (Fig. 1.11).[41] Correspondingly, the pore system of 12-MR materials can accommodate larger molecules than 10-MR materials.[41] Over a million unique, hypothetical zeolite crystal structures have been identified; however, to date, only about 230 natural or synthetic zeolite structures have been physically achieved.[41,42] Because Si is tetravalent, while Al is trivalent, isomorphous substitution of Si by Al in the crystal lattice generates a negative framework charge imbalance.[39] As a result, a cation (e.g., an alkali ion or a proton) balances the negative charge (Fig 1.12a).[39] This cation-bearing capacity of zeolites is crucial to their applications in ion-exchangers and in catalytic processes.[40] Fluid catalytic cracking in the petrochemical industry converts large, high-boiling hydrocarbons to smaller, more valuable products (e.g., gasoline and small olefins).[40] This process relies on the strong Brønsted acid sites that are generated in the H-form of zeolites (i.e., when protons balance the framework charge).

Zeotypes are materials with zeolite structures, but do not have strictly aluminosilicate framework compositions.[40] Isomorphous substitutions of Si by other tetravalent heteroatoms,

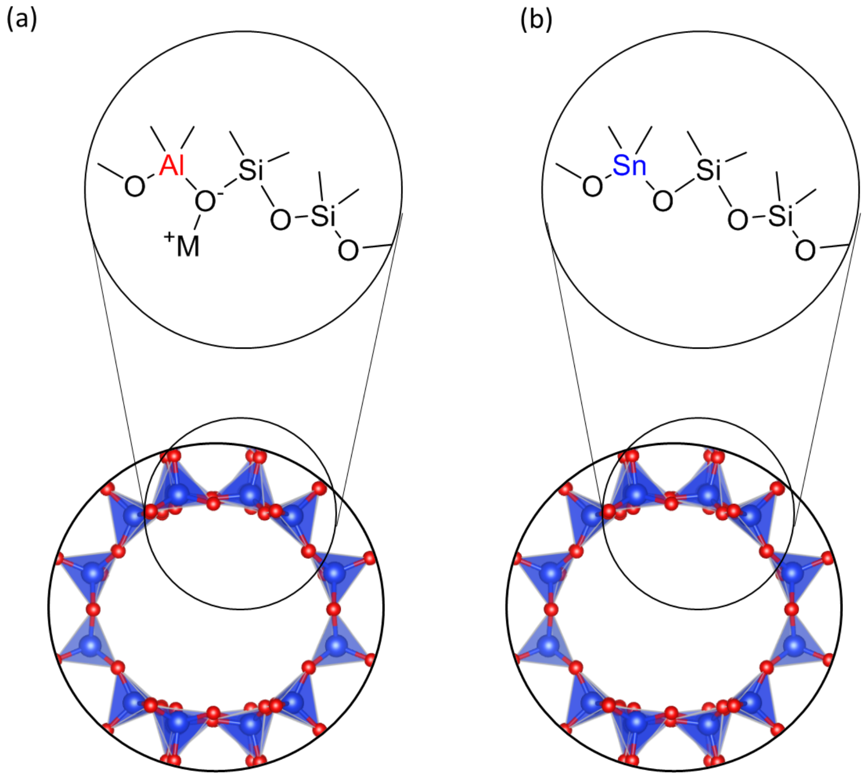

Figure 1.12 Charge imbalance (a) is generated when a trivalent cation (e.g., Al^{3+}) is isomorphously substituted into the lattice, but (b) is not generated in the case of a tetravalent cation (e.g., Sn^{4+}) isomorphous substitution.

e.g., Sn, Ti, Zr, or Hf, have been reported in otherwise pure-silica molecular sieves.[39,43] In such materials there is no framework charge imbalance (Fig. 1.12b). However, interesting catalytic properties can still emerge, as such heteroatoms can exceed tetrahedral coordination and function as Lewis acids.[44] While solid-state nuclear magnetic resonance (SS-NMR) spectroscopy may be used to characterize Si and Al, its use for characterization of most heteroatoms that have been incorporated into zeotypes is either very challenging (in the case of Sn), or essentially impossible with current instruments (in other cases).[45] Additionally, synthetic zeolite and zeotype crystals are usually too small for routine single-crystal X-ray crystallography. Though synchrotron X-ray crystallography of single crystals is often used for structure solutions of novel structures,[46] the incorporation of heteroatoms is usually random with respect to crystallographic position, eliminating the possibility of heteroatom coordination analysis. As a result, indirect characterization methods, such as probe-molecule Fourier transform infrared (FTIR) spectroscopy, temperature programmed desorption of probe adsorbates, and probe reactions, have been used to characterize such zeotype materials.

While all of the aforementioned heteroatoms may function as Lewis acids, as characterized by Lewis basic probe molecule spectroscopy, the catalytic behavior of these metal centers may vary. For instance, titanium sites in titanosilicates can activate hydrogen peroxide for epoxidation of olefins (Fig. 1.13a) or oxidation of alkanes and aromatics.[47] On the other hand, tin in stannosilicates preferably activates carbonyls, and in the presence of hydrogen peroxides, carbonyls, and double bonds, promotes Baeyer-Villiger oxidation instead of epoxidation (Fig. 1.13b).[48] Thus, while certain generalizations are possible about the behavior of Lewis-acidic zeotypes, careful characterizations of each material and reaction are required.

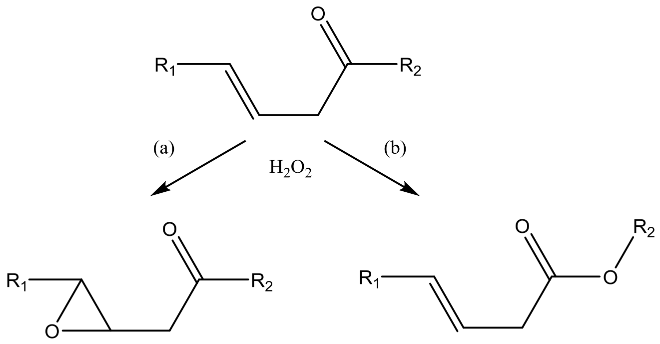

Figure 1.13 In the presence of H_2O_2 (a) Ti-Beta promotes epoxidation of olefins, while (b) Sn-beta promotes Bayer-Villiger oxidation of carbonyls.

In addition to the randomness of crystallographic site substitution by heteroatoms, further complexity in zeotype analysis comes from disorder that arises from local defects, such as partial hydrolysis of metal-oxygen-silicon bonds. In fact, in a number of systems, the partially hydrolyzed metal sites have very different reactivities from the perfectly substituted sites.[28,49,50] The capacity to alter (through synthetic or post-synthetic routes) the distribution of sites within heterogeneous catalysts is important, as it provides the opportunity to tune the activity and selectivity of a catalyst. The potential of such tunability is a motivating factor for studying the heteroatom site structure, its origin, and its effect on reactivity.

1.6 Thesis overview

The collection of works presented in this thesis strives to expand applications and understanding of catalysis in the processing of biomass-derived feedstocks and derivatives thereof. Chapter 2 discusses the outcomes of a collaborative study of the structure and reactivity of Sn sites in Sn-Beta zeotype in the context of glucose isomerization to fructose and epimerization to mannose.[51] This work provides the first (to the best of our knowledge) experimental proof that partially hydrolyzed "open" Sn sites, with proximal protonated silanols, are the primary active sites in 1,2-HS reactions of saccharides.[51] Furthermore, exchange of the open Sn sites' proximal silanols' protons by alkali cations is shown to generate Sn sites predominantly active for 1,2-CS reactions.[51] This discovery motivated further consideration of 1,2-CS catalysis. The proposed mechanisms of 1,2-CS reactions catalyzed by molybdates and Ni (II) diamines appear to have some similarity to aldol/retro-aldol reactions. The recognition of this similarity was the basis of the work presented in Chapter 3. In this chapter, a variety of 1,2-CS catalysts are shown to enhance retro-aldol rates and to be compatible with 1,2-HS catalysts in a tandem catalytic system that results in alkyl lactate yields comparable to the prior state-of-the-art non-biological catalytic systems, but at much lower temperatures.[52] Chapter 4 explores the Lewis acid chemistry of framework Zn sites in zincosilicate zeotypes.[53] Probe-molecule FTIR spectroscopy is used to demonstrate strong interactions of Lewis bases with Zn sites.[53] This knowledge is then translated to catalytic chemistry, resulting in the first (to the best of our knowledge) reported set of heterogeneous catalysts that are able to catalyze the Diels-Alder cycloaddition-dehydration of ethylene and dimethyl 2,5-furandicarboxylate with appreciable selectivity.[53] Chapter 5 provides concluding remarks regarding the work discussed in this thesis, and how it pertains to the broader field of study of zeotype Lewis acid chemistry. Finally, Chapter 5 briefly discusses the future potential of currently unpublished work regarding Diels-Alder cycloaddition-dehydration of ethylene and dimethyl 2,5-furandicarboxylate catalyzed by aluminosilicate zeolites.

1.7 References

(1) BP Global. *BP Energy Outlook 2035*; 2016.

(2) Huber, G. W.; Iborra, S.; Corma, A. *Chem. Rev.* **2006**, *106* (9), 4044–4098.

(3) U.S. Energy Information Administration. *Off. Integr. Int. Energy Anal.* **2015**, *1*, 1–244.

(4) EIA. Monthly Energy Review http://www.eia.gov/totalenergy/data/monthly/pdf/sec11_5.pdf.

(5) Lave, L. B. *Bridg.* **2009**, *39* (2), 76.

(6) Corma, A.; Iborra, S.; Velty, A. *Chem. Rev.* **2007**, *107* (6), 2411–2502.

(7) Dusselier, M.; Van Wouwe, P.; Dewaele, A.; Makshina, E.; Sels, B. F. *Energy Environ. Sci.* **2013**, *6* (5), 1415.

(8) Dusselier, M.; Mascal, M.; Sels, B. F. 2014; *Top Chemical Opportunities from Carbohydrate Biomass: A Chemist's View of the Biorefinery*, Springer Berlin Heidelberg,, pp 1–40.

(9) Lupoi, J. S.; Singh, S.; Parthasarathi, R.; Simmons, B. A.; Henry, R. J. *Renew. Sustain. Energy Rev.* **2015**, *49*, 871–906.

(10) Bañuls-Ciscar, J.; Abel, M.-L.; Watts, J. F. *Surf. Sci. Spectra* **2016**, *23* (1), 1–8.

(11) Van den Bosch, S.; Schutyser, W.; Vanholme, R.; Driessen, T.; Koelewijn, S.-F.; Renders, T.; De Meester, B.; Huijgen, W. J. J.; Dehaen, W.; Courtin, C. M.; Lagrain, B.; Boerjan, W.; Sels, B. F. *Energy Environ. Sci.* **2015**, *8* (6), 1748–1763.

(12) Scheller, H. V.; Ulvskov, P. *Annu. Rev. Plant Biol.* **2010**, *61* (1), 263–289.

(13) Zhang, J.; Teo, J.; Chen, X.; Asakura, H.; Tanaka, T.; Teramura, K.; Yan, N. *ACS Catal.* **2014**, *4* (5), 1574–1583.

(14) Boundy, B.; Diegel, S.; Wright, L.; Davis, S. C. **2011**, *4*, 254.

(15) Werpy, T.; Petersen, G. *Top Value Added Chemicals from Biomass: Volume I -- Results of Screening for Potential Candidates from Sugars and Synthesis Gas*; Pacific Northwest National Laboratory, 2004; Vol. 1.

(16) Holladay, J. E.; White, J. F.; Bozell, J. J.; Johnson, D. *Top Value-Added Chemicals from Biomass - Volume II-Results of Screening for Potential Candidates from Biorefinery Lignin*; Richland, WA, 2007; Vol. II.

(17) Beerens, K.; Desmet, T.; Soetaert, W. *J. Ind. Microbiol. Biotechnol.* **2012**, *39* (6), 823–834.

(18) Gunther, W. R.; Wang, Y.; Ji, Y.; Michaelis, V. K.; Hunt, S. T.; Griffin, R. G.; Román-Leshkov, Y. *Nat. Commun.* **2012**, *3*, 1109.

(19) Román-Leshkov, Y.; Moliner, M.; Labinger, J. A. J. A.; Davis, M. E. *Angew. Chem. Int. Ed. Engl.* **2010**, *49* (47), 8954–8957.

(20) Moliner, M.; Román-Leshkov, Y.; Davis, M. E. *Proc. Natl. Acad. Sci. USA* **2010**, *107* (14), 6164–6168.

(21) Nikolla, E.; Román-Leshkov, Y.; Moliner, M.; Davis, M. E. *ACS Catal.* **2011**, *1* (4), 408–410.

(22) van Putten, R.-J.; van der Waal, J. C.; de Jong, E.; Rasrendra, C. B.; Heeres, H. J.; de Vries, J. G. *Chem. Rev.* **2013**, *113* (3), 1499–1597.

(23) Pacheco, J. J.; Davis, M. E. *Proc. Natl. Acad. Sci. USA* **2014**, *111* (23), 8363–8367.

(24) Pacheco, J. J.; Labinger, J. A.; Sessions, A. L.; Davis, M. E. *ACS Catal.* **2015**, 5904–5913.

(25) Chang, C.-C.; Green, S. K.; Williams, C. L.; Dauenhauer, P. J.; Fan, W. *Green Chem.* **2014**, *16* (2), 585.

(26) Stütz, A. E. *Top. Curr. Chem.* **2001**, *215*, 351.

(27) Bermejo-Deval, R.; Gounder, R.; Davis, M. E. *ACS Catal.* **2012**, *2* (12), 2705–2713.

(28) Boronat, M.; Corma, A.; Renz, M. *J. Phys. Chem. B* **2006**, *110* (42), 21168–21174.

(29) Rasrendra, C. B.; Fachri, B. A.; Makertihartha, I. G. B. N.; Adisasmito, S.; Heeres, H. J. *ChemSusChem* **2011**, *4* (6), 768–777.

(30) Petruš, L.; Petrušová, M.; Hricovíniová, Z. In *Glycoscience: Epimerisation, Isomerisation and Rearrangement Reactions of Carbohydrates*; Stütz, A. E., Ed.; 2001.

(31) Fessner, W.; Schneider, A.; Held, H.; Sinerius, G.; Walter, C.; Hixon, M.; Schloss, J. V. *Angew. Chemie Int. Ed. English* **1996**, *35* (19), 2219–2221.

(32) Osmundsen, C. M.; Holm, M. S.; Dahl, S.; Taarning, E. *Proc. R. Soc. A* **2012**, *468* (2143), 2000–2016.

(33) Holm, M. S.; Saravanamurugan, S.; Taarning, E. *Science* **2010**, *328* (5978), 602–605.

(34) Osmundsen, C. M.; Holm, M. S.; Dahl, S.; Taarning, E. *Proc. R. Soc. A* **2012**, *468* (2143), 2000–2016.

(35) Tolborg, S.; Sádaba, I.; Osmundsen, C. M.; Fristrup, P.; Holm, M. S.; Taarning, E. *ChemSusChem* **2015**, *8* (4), 613–617.

(36) Román-Leshkov, Y.; Davis, M. E. *ACS Catal.* **2011**, *1* (11), 1566–1580.

(37) Nikbin, N.; Do, P. T.; Caratzoulas, S.; Lobo, R. F.; Dauenhauer, P. J.; Vlachos, D. G. *J. Catal.* **2013**, *297*, 35–43.

(38) Pacheco, J. J. New Catalysts for the Renewable Production of Monomers for Bioplastics, California Institute of Technology, 2015.

(39) Davis, M. E.; Lobo, R. F. *Chem. Mater.* **1992**, *4* (4), 756–768.

(40) Corma, A. *J. Catal.* **2003**, *216* (1-2), 298–312.

(41) Baerlocher, C.; McCusker, L. B. Database of Zeolite Structures http://www.iza-structure.org/databases/.

(42) Earl, D. J.; Deem, M. W. *Ind. Eng. Chem. Res.* **2006**, *45* (16), 5449–5454.

(43) Li, J.; Corma, A.; Yu, J. *Chem. Soc. Rev.* **2015**, *44*, 7112–7127.

(44) Moliner, M. *Dalt. Trans.* **2014**, *43* (11), 4197–4208.

(45) Hwang, S.-J.; Gounder, R.; Bhawe, Y.; Orazov, M.; Bermejo-Deval, R.; Davis, M. E. *Top. Catal.* **2015**, *58* (7-9), 435–440.

(46) Freyhardt, C. C.; Lobo, R. F.; Khodabandeh, S.; Lewis, J. E.; Tsapatsis, M.;

Yoshikawa, M.; Camblor, M. A.; Pan, M.; Helmkamp, M. M.; Zones, S. I.; Davis, M. E. *J. Am. Chem. Soc.* **1996**, *118* (31), 7299–7310.

(47) Khouw, C. B. Partial Oxidation of Hydrocarbons Using Titanium Containing Molecular Sieves, California Institute of Technology, 1995.

(48) Corma, A.; Nemeth, L. T.; Renz, M.; Valencia, S. *Nature* **2001**, *412* (6845), 423–425.

(49) Boronat, M.; Concepcion, P.; Corma, A; Renz, M.; Valencia, S. *J. Catal.* **2005**, *234* (1), 111–118.

(50) Khouw, C. B.; Davis, M. E. *J. Catal.* **1995**, *151* (1), 77–86.

(51) Bermejo-Deval, R.; Orazov, M.; Gounder, R.; Hwang, S.-J.; Davis, M. E. *ACS Catal.* **2014**, *4* (7), 2288–2297.

(52) Orazov, M.; Davis, M. E. *Proc. Natl. Acad. Sci. USA* **2015**, *112* (38), 11777–11782.

(53) Orazov, M.; Davis, M. E. *Chem. Sci.* **2016**, *7* (3), 2264–2274.

Chapter 2

Identification and Characterization of Active Sites in Sn-Beta for Glucose Isomerization to Fructose and Epimerization to Mannose

Information contained in Chapter 2 was originally published in:

(Bermejo-Deval, R.***; Orazov, M.***; Gounder, R.; Hwang, S.; Davis, M. E. *ACS Catal.*, **2014**, *4*, 2288–2297. DOI: 10.1021/cs500466j) ***Equal Contribution**

2.1 Introduction

The Davis group has previously shown that framework tetravalent Lewis acidic metal centers (Sn^{4+} and Ti^{4+}) within hydrophobic, pure-silica molecular sieves with the zeolite beta framework topology (Sn-Beta and Ti-Beta, respectively) catalyze the isomerization reactions of glucose in aqueous media.[1–4] Framework Sn sites ring-open and coordinate glucose prior to isomerization via a formal 1,2-intramolecular hydride shift from C2 to C1 position (1,2-HS) of the ring-opened glucose chain.[1] This glucose isomerization reaction pathway is analogous to that observed in metalloenzymes such as D-xylose isomerase XI that contains two divalent Lewis acid metal centers (e.g., Mg^{2+} or Mn^{2+}) confined within a hydrophobic pocket.[5–7] Extraframework SnO_x clusters located within hydrophobic micropores of pure-silica zeolite beta, but not at external crystallite surfaces or on amorphous supports, are also able to isomerize glucose to fructose in aqueous solutions. Unlike the framework Sn centers, these extraframework intrazeolitic SnO_x clusters act as solid bases that catalyze glucose isomerization via Lobry de Bruyn-Alberda van Ekenstein (LdB-AvE) rearrangements involving enolate intermediates,[2,8] and the hydrophobic surrounding voids appear to protect

SnO_x surface sites from inhibition or deactivation that otherwise occurs in the presence of bulk liquid water.

Surprisingly, in a prior report from the Davis group, certain samples of Sn-Beta reacting glucose, in a methanolic solvent, selectively produced mannose via a Lewis-acid-mediated 1,2-intramolecular carbon shift (1,2-CS) mechanism, also known as the Bílik reaction.[2] Although homogeneous molybdate anions[9–11] and nickel(II) diamine complexes[12–14] have been reported to catalyze the epimerization of glucose to mannose by the Bílik reaction, Sn-Beta was the first example of a heterogeneous microporous catalyst that could mediate this reaction.[2] Only framework Sn sites in Sn-Beta were able to form mannose via the Bílik reaction in methanol, as intrazeolitic SnO_x clusters isomerized glucose to fructose via base-catalyzed LdB-AvE rearrangement.[2] SnO_x clusters deposited on external zeolite crystal surfaces and on amorphous silica also isomerized glucose to fructose in liquid methanol by the enolate mechanism,[2] in contrast with their inability to do so in liquid water. Thus, only zeolites that contained framework Sn sites showed differences in the predominant mechanism by which glucose is reacted in aqueous and methanolic solvents.

Framework Sn centers in Sn-Beta were proposed by Corma *et al.*[15] to be present in both "closed" and "open" forms that correspond to a non-hydrolyzed Sn site ($Sn\text{-}(OSi)_4$) and a partially hydrolyzed Sn site ($(HO)\text{-}Sn\text{-}(OSi)_3$) (shown in their dehydrated states in Fig. 2.1a and 2.1b, respectively). The open sites were proposed to be more reactive in the Baeyer-Villiger oxidation of cyclic ketones.[15] By extension, this site activity was also proposed for intermolecular MPVO reactions.[16] Similarly, the Davis group has proposed the open Sn sites to be more reactive in the isomerization of glucose into fructose.[1] In attempts to increase the proportion of open Sn sites in Sn-Beta, the Davis group has investigated the substitution of

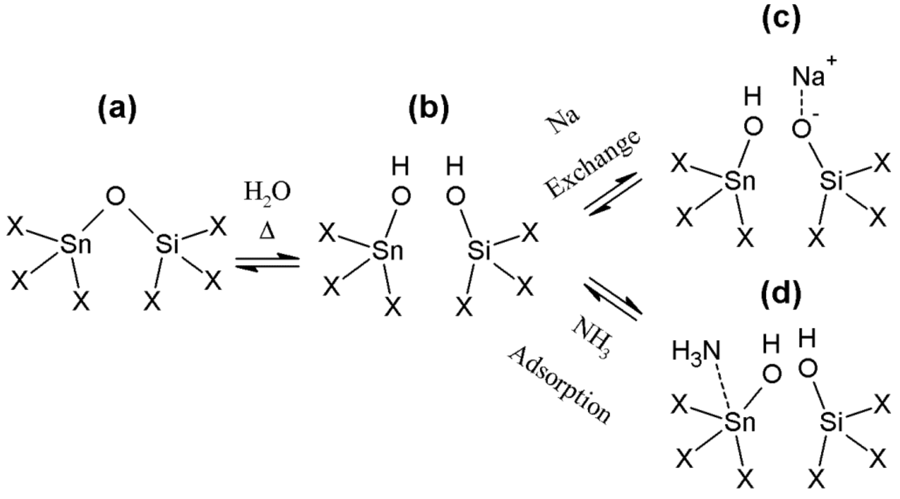

Figure 2.1 Schematic representation of the dehydrated states of (a) closed and (b) open sites in Sn-Beta, (c) the Na-exchanged open site, and (d) the NH_3-dosed open site. “X” denotes framework O-Si units.

$SnCl_4$ precursors with $Sn(CH_3)Cl_3$ during crystallization, as well as Na^+ exchanges prior to calcination, as these treatments were hypothesized to prevent condensation of proximal Sn-OH and Si-OH groups.[1] The reactivities of Sn-Beta samples prepared though these alternate routes were reported as indistinguishable from that of Sn-Beta crystallized using the normal $SnCl_4$ precursors, suggesting that open and closed Sn sites were interconvertible during calcination and reaction conditions.[1] As a result, while open and closed Sn sites in Sn-Beta were distinguished in ^{119}Sn NMR spectra, these prior experimental data could not conclusively determine if the open Sn site was the exclusive active site for glucose isomerization.[1]

Though conclusive experimental data was lacking, quantum chemical studies suggested that glucose-fructose isomerization pathways are catalyzed with lower barriers on open Sn sites than closed Sn sites.[1] Previously, Khouw and Davis[17] selectively exchanged Na^+ onto silanol groups (Si-OH) adjacent to open Ti sites ($(HO)\text{-}Ti\text{-}(OSi)_3$) in titanosilicate TS-1 and demonstrated complete inhibition of catalytic alkane oxidation by hydrogen peroxide,[17] providing evidence that open Ti sites are the active sites for alkane oxidation in TS-1. Thus, it seemed plausible that the silanol group adjacent to the open Sn site in Sn-Beta could influence the rates and selectivities of glucose isomerization catalysis. Rai *et al.*[18] used density functional theory (DFT) to calculate the energetics of glucose-fructose isomerization (1,2-HS) and glucose-mannose epimerization (1,2-CS) pathways when glucose binds to an open Sn site in a monodentate mode that involves the adjacent silanol group versus the energetics of these pathways with a bidentate binding mode that does not involve the neighboring silanol group. These calculations suggested that the monodentate pathway resulted in lower barriers for the glucose-fructose isomerization via the 1,2-HS pathway, relative to epimerization via the 1,2-CS pathway.[18] Conversely, the bidentate binding mode resulted in a lower energy pathway for the glucose-mannose epimerization via the 1,2-CS pathway.[18] If epimerization is a lower energy pathway than isomerization when silanol groups adjacent to Sn sites are not involved in the mechanism, a detail that was not addressed by Rai et al.,[18] then prior experimental results[2] suggest that active sites in Sn-Beta in methanol may be altered in a manner that precludes the involvement of the neighboring silanol in the reaction pathway.

Here, new experimental results pertaining to the structures of the active Sn sites in Sn-Beta for glucose isomerization and epimerization reactions are provided. First, through selective NH_3 poisoning, we demonstrate that the closed Sn sites appear to be essentially inactive for both 1,2-HS and 1,2-CS reactions. The mechanistic role of the silanol group adjacent to the open Sn site is examined by exchanging its proton with a sodium cation. We provide evidence that Na^+-exchanged Sn-Beta catalyzes the epimerization of glucose to mannose via 1,2-CS with high selectivity in methanolic solutions and in concentrated aqueous NaCl solutions. In water, for such materials, the selectivity for isomerization to fructose via 1,2-HS, relative to epimerization to mannose via 1,2-CS, increases with reaction time because Na^+ ions are removed from the active sites over the course of the reaction (resulting in protonated proximal silanol groups). These data clearly show that the open Sn site is the active site for both glucose isomerization and epimerization reactions, with isomerization prevailing when adjacent silanol groups are in their proton form and epimerization prevailing when adjacent silanol groups are exchanged with Na^+.

2.2 Experimental Methods

2.2.1 Synthesis of Sn-Beta, ^{119}Sn-Beta, Na-Sn-Beta and Si-Beta

Sn-Beta and ^{119}Sn-Beta were synthesized according to previously reported procedures.[1] 15.25 g of tetraethylammonium hydroxide solution (Sigma-Aldrich, 35% (w/w) in water) were added to 14.02 g of tetraethylorthosilicate (Sigma-Aldrich, 98% (w/w)), followed by the addition of 0.172 g of tin (IV) chloride pentahydrate (Sigma-Aldrich, 98% (w/w)) or of 0.121 g of ^{119}Sn enriched tin (IV) chloride pentahydrate (Cambridge Isotopes, 82% isotopic enrichment). The mixture was stirred until tetraethylorthosilicate was completely hydrolyzed and then allowed to reach the targeted $H_2O:SiO_2$ ratio by complete evaporation of ethanol and partial evaporation of water. Finally, 1.53 g of HF solution (Sigma Aldrich, 54% (w/w) in water) were added, resulting in the formation of a thick gel. The final molar composition of the gel was 1 SiO_2 / 0.0077 $SnCl_4$ / 0.55 TEAOH / 0.54 HF / 7.52 H_2O. As-synthesized Si-Beta (vide infra) was added as seed material (5 wt% of SiO_2 in gel) to this gel and mixed. The final gel was transferred to a Teflon-lined stainless steel autoclave and heated at 413 K in a static oven for 40 days. The recovered solids were centrifuged, washed extensively with water, and dried at 373 K overnight. The dried solids were calcined in flowing air (1.67 $cm^3\ s^{-1}$, Air Liquide, breathing grade) at 853 K (0.0167 $K\ s^{-1}$) for 10 h to remove the organic content located in the crystalline material. ^{119}Sn-Beta was calcined twice under the same conditions.

Na-Sn-Beta was synthesized using the same procedure as Sn-Beta, but with the addition of $NaNO_3$ (Sigma Aldrich, ≥99.0%) to the synthesis gel. The final molar composition of the gel was 1 SiO_2 / x $NaNO_3$ / 0.0077 $SnCl_4$ / 0.55 TEAOH / 0.54 HF / 7.52 H_2O, where "x" was 0.010, 0.017 and 0.033 (Na-Sn-Beta-100, 60 and 30, respectively). The gel was transferred to a Teflon-lined stainless steel autoclave and heated at 413 K in a static oven for 25 days. The recovered solids were washed, dried, and calcined using the same procedure as for Sn-Beta. Synthesis gels with Si/Na ratio lower than 30 yielded a heterogeneous material with small black particles dispersed among the zeolite. These black particles were separated from the zeolite by hand, and were found to be amorphous, having a Si/Sn and Na/Sn ratio of 15 and 2.28, respectively.

Si-Beta was prepared by adding 10.01 g of tetraethylammonium fluoride dihydrate (Sigma-Aldrich, 97% (w/w) purity) to 10 g of water and 4.947 g of tetraethylorthosilicate (Sigma-Aldrich, 98% (w/w)). This mixture was stirred overnight at room temperature in a closed vessel to ensure complete hydrolysis of the tetraethylorthosilicate. The targeted H_2O:SiO_2 ratio was reached by complete evaporation of the ethanol and partial evaporation of the water. The final molar composition of the gel was SiO_2 / 0.55 TEAF / 7.25 H_2O. The gel was transferred to a Teflon-lined stainless steel autoclave and heated at 413 K in a rotation oven (60 rpm) for 7 days. The solids were recovered by filtration, washed extensively with water, and dried at 373 K overnight. The dried solids were calcined in flowing air (1.67 cm^3 s^{-1}, Air Liquide, breathing grade) at 853 K (0.0167 K s^{-1}) for 10 h to remove the organic content located in the crystalline material.

2.2.2 Na^+ and H^+ ion exchange of zeolite samples

Each ion exchange step was carried out for 24 hours at ambient temperature, using 45 mL of exchange or wash solution per 300 mg of starting solids. For the procedures involving multiple ion-exchange steps, the ion-exchange solution was replaced every 24 hours without intermediate water washing. One, two, and three successive sodium ion exchanges (Sn-Beta-1Ex, Sn-Beta-2Ex, and Sn-Beta-3Ex, respectively) were performed by stirring calcined Sn-Beta in a solution of 1 M $NaNO_3$ (Sigma Aldrich, ≥99.0%) and 10^{-4} M NaOH (Alfa Aesar 97%) in distilled water. The final material was recovered by centrifugation, and washed three times with 1 M $NaNO_3$ in distilled water. Acid-washed Sn-Beta (Sn-Beta-AW) was made by stirring the triply-sodium-exchanged Sn-Beta (Sn-Beta-3Ex) in 1 M H_2SO_4 (Macron Fine Chemicals, >51%) for 1 h, at ambient temperature, followed by separation by filtration and washing with 1 L of distilled water in 100 mL batches. Finally, the material was dried in room temperature air and calcined in flowing air (1.67 cm^3 s^{-1}, Air Liquide, breathing grade) at 853 K (0.0167 K s^{-1}). We note that the dehydration of sodium-exchanged materials resulted in changes in their catalytic properties; therefore, to ensure comparable saturation of the samples with water, 24 h prior to reaction testing, all samples were placed in a chamber whose humidity was controlled by a saturated NaCl solution.

2.2.3 Ammonia adsorption onto Sn-Beta

Ammonia gas dosing experiments were performed on Sn-Beta samples after drying in a Schlenk flask at 473 K for 2 h under vacuum. The dried Sn-Beta was cooled under dynamic vacuum to ambient temperature, and the flask was backfilled with 101 kPa of anhydrous ammonia gas (Matheson Tri-Gas, 99.99%). After 24 h, the excess ammonia was evacuated and the sample was exposed to atmosphere (Sn-Beta-NH_3). The ammonia-saturated material was regenerated by calcination (Sn-Beta-NH_3-Cal) in flowing air (1.67 cm^3 s^{-1}, Air Liquide, breathing grade) for 6 h at 853 K (0.0167 K s^{-1}).

2.2.4 Characterization methods

Scanning electron microscopy (SEM) with Energy Dispersive X-ray Spectroscopy (EDS) measurements were recorded on a LEO 1550 VP FE SEM at an electron high tension (EHT) of 15 kV. The crystalline structures of zeolite samples were determined from powder X-ray diffraction (XRD) patterns collected using a Rigaku Miniflex II diffractometer and Cu Kα radiation.

Ar adsorption isotherms at 87 K were obtained using a Quantachrome Autosorb iQ automated gas sorption analyzer. Zeolite samples were degassed at 353 K (0.167 K s^{-1}) for 1 h, 393 K (0.167 K s^{-1}) for 3 h and 623 K (0.167 K s^{-1}) for 8 h prior to recording dry sample weight. For Sn-Beta-NH_3, the temperature during the degassing procedure never exceeded 473 K (0.167 K s^{-1}). Relative pressures (P/P_0) were measured between 10^{-7} and 1 at 87 K with precise volumetric Ar doses.

Deuterated acetonitrile dosing and desorption experiments were performed according to the procedure described elsewhere.[19] A Nicolet Nexus 470 Fourier transform infrared (FTIR) spectrometer with a Hg-Cd-Te (MCT) detector was used to record spectra in 4000-650 cm^{-1} range with a 2 cm^{-1} resolution. Self-supporting wafers (10-20 mg cm^{-2}) were pressed and sealed in a heatable quartz vacuum cell with removable KBr windows. The cell was purged with air (1 cm^3 s^{-1}, Air Liquide, breathing grade) while heating to 373 K (0.0167 K s^{-1}), where it was held for 12 h, followed by evacuation at 373 K for >2 h (<0.01

Pa dynamic vacuum; oil diffusion pump), and cooling to 308 K under dynamic vacuum. CD_3CN (Sigma-Aldrich, 99.8% D-atoms) was purified by three freeze (77 K), pump, thaw cycles, then dosed to the sample at 308 K until the Lewis acid sites were saturated. At this point, the first FTIR spectrum in the desorption series was recorded. The cell was evacuated down to 13.3 Pa, and the second spectrum was recorded. Then, the cell was evacuated under dynamic vacuum while heating to 433 K (0.0167 K s^{-1}). Concurrently, a series of FTIR spectra were recorded (2 min for each spectrum) at 5 minute intervals. The resulting spectra were baseline-corrected, and the most illustrative spectra were chosen for presentation. The spectra are not normalized by the number of Sn sites. Spectral artifacts known as “interference fringes” were removed using a computational method based on digital filtering techniques and Fourier analysis.[20]

Solid-state magic angle spinning nuclear magnetic resonance (MAS NMR) measurements were performed using a Bruker Avance 500MHz spectrometer equipped with a 11.7 T magnet and a Bruker 4mm broad band dual channel MAS probe. The operating frequencies were 500.2 MHz and 186.5 MHz for ^{1}H and ^{119}Sn nuclei, respectively. Approximately 60-80 mg of powder were packed into 4mm ZrO_2 rotors and spun at 14 kHz for MAS or cross polarization (CP) MAS experiments at ambient condition. $^{119}Sn\{^{1}H\}$ CP condition was optimized at radiofrequency pulse power of 62.5 kHz $\pm \nu_r$, where ν_r is spinning frequency, and spectra were recorded using 2 ms contact time. The recycle delay times were 20 sec and 2 sec for ^{119}Sn MAS and CPMAS experiments, respectively. Signal averaging over 8,000 scans was performed for the CPMAS spectrum of ^{119}Sn-Beta dehydrated after NH_3 dosing, while averaging over 30,000 scans was performed for the CPMAS spectrum of ^{119}Sn-Beta dehydrated after three Na-exchanges.

Liquid ^{13}C NMR spectra were recorded using a Varian INOVA 500 MHz spectrometer equipped with an auto-x pfg broad band probe. Carbon chemical shifts are reported relative to the residual solvent signal. ^{13}C NMR spectra were acquired with 2000 scans.

2.2.5 *Reaction procedures*

Reactions with D-glucose (Sigma-Aldrich, ≥99%) were conducted in 10 ml thick-walled glass reactors (VWR) that were heated in a temperature-controlled oil bath. Reactions were prepared with a 1:100 Sn:glucose molar ratio using 5.0 g of a 1% (w/w) glucose solution with approximately 20 mg of catalyst. For reactions performed to investigate the effects of addition of NaCl to aqueous glucose reactant solution, 0.2 g of NaCl were added per 1.0 g of 1% (w/w) glucose solution. Reactors were placed in the oil bath at 353 K and approximately 50 mg aliquots were extracted at 10, 20 and 30 minutes. These reaction aliquots were mixed with 50 mg of a 1% (w/w) D-mannitol (Sigma-Aldrich, ≥98%) solution as an internal standard for quantification, diluted with 0.3 ml of H_2O, and filtered with a 0.2 μm PTFE syringe filter.

Glucose conversions and product yields were calculated by:

$$X_{Gluc.}(t) = \frac{\left(n_{Gluc}(t=0) - n_{Gluc}(t)\right)}{n_{Gluc}(t=0)} \cdot 100\ [\%] \tag{1}$$

$$Y_i(t) = \frac{n_i(t)}{n_{Gluc}(t=0)} \cdot 100\ [\%] \tag{2}$$

where $X_{Gluc}(t)$ is the glucose conversion at time *t*, in percent, $Y_i(t)$ is the fructose or mannose yield at time *t*, in percent, $n_{Gluc}(t=0)$ is the initial moles of glucose in the reactor, $n_{Gluc}(t)$ is the moles of glucose in the reactor at time *t*, and $n_i(t)$ is the moles of fructose or mannose in the reactor at time t.

Recyclability experiments were performed with Sn-Beta-3Ex reacted with glucose in water and methanol under the previously stated reaction conditions (353 K for 30 min in a 1% (w/w) with 1:100 Sn:glucose molar ratio) and washed once with the solvent used in the reaction. The solids were centrifuged and dried with ambient temperature air.

Reaction aliquots were analyzed by high performance liquid chromatography (HPLC) using an Agilent 1200 system (Agilent) equipped with PDA UV (320 nm) and evaporative light scattering (ELS) detectors. Glucose, fructose, mannose, and mannitol fractions were separated with a Hi-Plex Ca column (6.5 x 300 mm, 8 µm particle size, Agilent) held at 358 K, using ultrapure water as the mobile phase at a flow rate of 0.6 mL s^{-1}.

Reactions with labeled ^{13}C glucose at the C1 position (Cambridge Isotope Laboratories,1-^{13}C D-glucose, 98-99%) and deuterium (D) in the C2 position of glucose (Cambridge Isotope Laboratories, D-glucose-D2, >98%) were conducted under the same conditions as those with D-glucose. The reaction was ended by quenching after 30 minutes. The reaction solution was filtered and rotavaporated to separate the solvent from the reactant-product mixture. These recovered solids were dissolved in deuterium oxide and analyzed using ^{13}C NMR.

2.3 Results and Discussion

2.3.1 Characterization of microporous materials

The powder X-ray patterns of Sn-Beta, Sn-Beta-1Ex, Sn-Beta-2Ex, Sn-Beta-3Ex, Sn-Beta-AW, Sn-Beta-NH_3, Sn-Beta-NH_3-Cal and Na-Sn-Beta (Si/Na=100, 60 and 30) (Figs. A1 and A2 in Appendix A) show that each of the samples is highly crystalline and has the zeolite beta framework topology. No diffraction lines were observed at 2θ values of 26.7^{o} and 34.0^{o} that are characteristic of bulk SnO_2. SEM images (Fig. A3 in Appendix A) indicate that the crystallite size of Sn-Beta is between 5-8 μm, and does not change significantly after exchange with $NaNO_3$/NaOH or treatment with NH_3. Na-Sn-Beta-30 (SEM images shown in Fig. A4 in Appendix A) and other materials with gel Na/Sn ratios > 30 (results not presented here because of the high impurity content) contain an impurity that consists of dark, amorphous (by powder XRD) particles that are not observed in Na-Sn-Beta-60 and Na-Sn-Beta-100. Thus, synthesis gels with high amounts of Na formed contaminating amorphous solids with high Na and Sn contents (*Si/Sn =15, Na/Sn = 2.28)*. Bellusi et al.[21] proposed that the insertion of titanium into the silicate framework (TS-1) is inhibited when alkali metal ions are present in the synthesis gel due to the formation of alkali titanates. Here, it is possible that the Sn atoms in the synthesis gels form alkali stannates that are part of the amorphous phase impurity, thereby lowering the Sn and Na content of the crystalline Na-Sn-Beta that is formed

The total micropore volumes of the samples were determined from Ar adsorption isotherms (87 K, Figs. A5-A14 in Appendix A) and are listed in Table 2.1. The micropore volume of all Na-exchanged materials decreased, perhaps because of excess $NaNO_3$ that remains on the solid after Na exchange. The final wash in the exchange procedure was performed with 1M $NaNO_3$ because washing with distilled water results in partial Na^+ removal from the catalytic site. The FTIR spectra (Fig. A15 in Appendix A) of the Na exchanged materials show a broad shoulder in the 1300 to 1500 cm^{-1} range as would be expected for the NO_3^- ion.[22] Sn-Beta-AW has the same micropore volume (0.19 cm^3 g^{-1}) as the parent Sn-Beta material, indicating that the measured decrease in microporosity for the Na-exchanged materials is not due to a loss of crystallinity, but likely due to the excess $NaNO_3$. Na-Sn-Beta-60 and Na-Sn-Beta-100 exhibit a similar micropore volume to Sn-Beta

(Table 2.1), but Na-Sn-Beta-30 has a lower micropore volume of 0.14 $cm^3 g^{-1}$. This significant decrease in micropore volume is likely due to the amorphous particle impurities. The ammonia-dosed Sn-Beta showed a lower micropore volume of 0.17 cm^3 g^{-1}, which increased to that of the parent Sn-Beta sample after calcination (0.19 cm^3 g^{-1}).

Table 2.1 Site and structural characterization of samples used in this study.

Catalyst	**Si/Sn**[a]	**Na/Sn**[a]	**Ar micropore volume**[b] (cm^3 g^{-1})	**IR bands** *(cm^{-1})*
Sn-Beta	95	0.00	0.19	2315, 2307, 2276 and 2266
Sn-Beta-1Ex	115	3.80	0.16	2310, 2280 and 2274
Sn-Beta-2Ex	159	4.38	0.15	2310, 2280 and 2274
Sn-Beta-3Ex	140	4.85	0.16	2310, 2280 and 2274
Sn-Beta-AW	104	0.27	0.19	2315, 2307, 2276 and 2266
Na-Sn-Beta-100	113	0.12	0.18	n.d.
Na-Sn-Beta-60	127	0.26	0.19	n.d.
Na-Sn-Beta-30	91	0.94	0.15	2310, 2280 and 2274
Sn-Beta-NH_3	105	0.00	0.17	2306 and 2270
Sn-Beta-NH_3-Cal	117	0.00	0.19	2315, 2307, 2276 and 2266

[a] Determined by Energy Dispersive X-ray Spectroscopy (EDS). The highest measured Si/Sn standard deviation for three scans of different parts of the same material was ± 30, while the highest Na/Sn standard deviation was of ± 1.25. These maximal standard deviations may be used to estimate the uncertainty of measurement for all samples.

[b] Determined from the Ar adsorption isotherm (87K).

[C] n.d., not determined

Table 2.1 lists the Sn and Na contents for all of the samples in this study. The Na/Sn ratio increased with the number of consecutive sodium ion exchanges, with the highest ratio being 4.38 after three consecutive exchanges with $NaNO_3$/NaOH. Na/Sn ratios above unity likely reflect the presence of excess $NaNO_3$ deposited on the sample and some Na exchange occurring at silanol groups other than the ones adjacent to open Sn centers. Acid treatment removed most of the sodium from the zeolite, as the Na/Sn ratio in Sn-Beta-AW decreased to 0.27. The Na/Sn ratio in the solids synthesized in the presence of sodium (Na-Sn-Beta-100, 60 and 30) increased as the sodium concentration increased in the synthesis gels.

2.3.2 Structural characterization of the Sn sites in Sn-Beta

The nature of Lewis acidic Sn sites in Sn-Beta and post-synthetically treated Sn-Beta samples was probed by monitoring changes in IR bands for C≡N stretching vibrations of adsorbed deuterated acetonitrile (2260-2340 cm^{-1})[23] during temperature-programmed desorption experiments (Figs. 2.2 and A16-A19 in Appendix A). The IR spectra for Sn-Beta exposed to CD_3CN show bands at 2315, 2307, 2276, and 2266 cm^{-1} (Fig. 2.2a). The CD_3CN IR bands at 2276 and 2266 cm^{-1} have been assigned to CD_3CN coordinated to silanol groups and physisorbed CD_3CN, respectively, while the bands at 2315 and 2307 cm^{-1} have been assigned to CD_3CN coordinated to Lewis acid sites.[23,24] These results are consistent with Corma *et al.*[15], who assigned the 2316 cm^{-1} band to CD_3CN bound at the open Sn site, and the 2308 cm^{-1} band to CD_3CN bound at a weaker Lewis acid site proposed to be the closed Sn site.

After $NaNO_3$/NaOH treatments (Figs. 2.2b, A16, and A17 in Appendix A), IR bands associated with CD_3CN bound to the open and closed sites disappear or diminish in intensity, while a single broad IR band with low intensity appears at ~2310-2312 cm^{-1}. We speculate

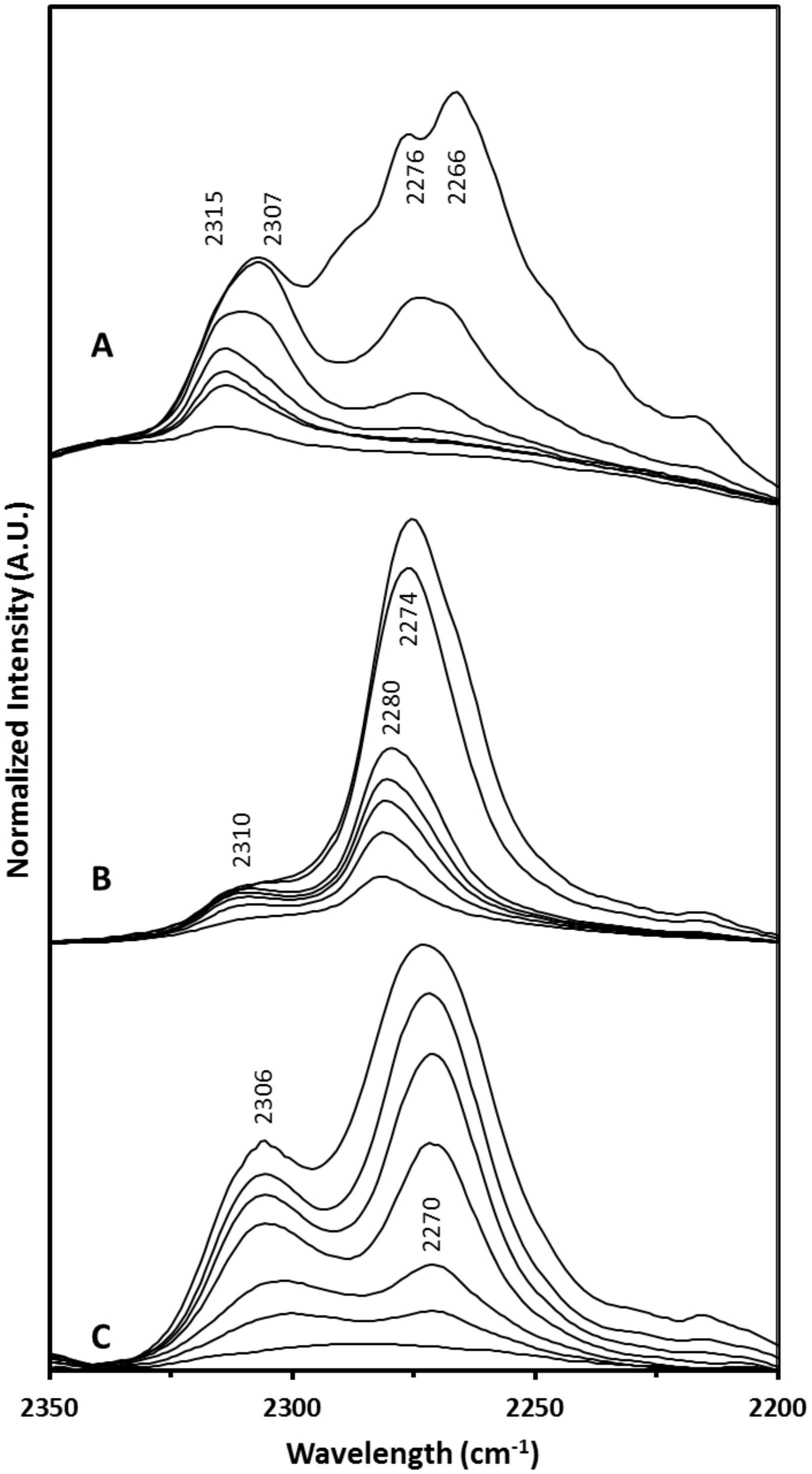

Figure 2.2 Baseline-corrected IR spectra with decreasing CD_3CN coverage on (a) Sn-Beta, (b) Sn-Beta-3Ex, and (c) Sn-Beta-NH_3.

that this broad band may reflect multiple contributions from residual non-exchanged Sn sites, by extension of previous reports by Corma *et al.*[25] showing that a similar broad band at 2310 cm^{-1} in Sn-MCM-41 may be deconvoluted into multiple bands that correspond to different Sn environments. Interestingly, a more prominent IR band appears at 2280 cm^{-1} in Na-exchanged Sn-Beta materials (Figs. 2.2b, A16, and A17 in Appendix A), which we tentatively associate with the Lewis acid site responsible for the reactivity of these samples. The lower frequency of this new band (2280 cm^{-1}) compared to the open Sn site in Sn-Beta (2315 cm^{-1}) may suggest a weaker interaction[23] of CD_3CN with Lewis acid sites in Na-exchanged Sn-Beta. The CD_3CN that gives rise to the 2280 cm^{-1} band, however, desorbs more slowly than CD_3CN bound to the closed site (2307 cm^{-1}) and at comparable rates to CD_3CN bound to the open site (Figs. 2.2a and 2.2b). These findings suggest that, in addition to the direct electron donation of CD_3CN to the Lewis acidic Sn center, secondary interactions of CD_3CN with the site or its surrounding environment may influence the binding strength and thus the $\nu(C{\equiv}N)$ of CD_3CN. Strongly-bound CD_3CN at 2280 cm^{-1} (Fig. A18 in Appendix A) was not present on Na-exchanged Si-Beta, confirming that this IR band is not a result of CD_3CN adsorbed to Na-exchanged terminal silanol groups, and requires the presence of a framework Sn site. The synthetic Na-Sn-Beta-30 sample showed a similar desorption profile to that of Na-exchanged Sn-Beta (Fig. A19 in Appendix A), suggesting that Na^+ ions introduced during or after synthesis have similar effects on the ability of Lewis acid sites in Sn-Beta to bind CD_3CN.

CD_3CN adsorption onto Sn-Beta-NH_3 gives rise to IR bands at 2306 cm^{-1}, associated with the closed Sn sites (as confirmed by ^{119}Sn NMR, vide infra), and a previously unobserved band at 2270 cm^{-1} (Fig. 2.2c) for sites that release CD_3CN at a rate similar to that of the closed sites. The IR band of CD_3CN bound to the open site at 2315 cm^{-1} was not observed (Fig. 2.2c). These data indicate that NH_3 remains bound only to open Sn sites in Sn-Beta-NH_3 after exposure to ambient air and treatment in vacuum at 373 K prior to CD_3CN exposure (Fig. 2.3), consistent with proposals that open Sn sites are stronger Lewis acid sites than closed sites.[15] We propose that open Sn sites with bound NH_3 in Sn-Beta-NH_3 (Fig. 2.1d) are more electron-rich, and in turn bind CD_3CN more weakly, than open Sn sites without NH_3 ligands in Sn-Beta (Fig. 2.1b). The open Sn site with pre-adsorbed NH_3 (Fig. 2.1d) seems to be a likely candidate for the IR band at 2270 cm^{-1} (Fig. 2.2c), which arises from weakly-bound CD_3CN that disappears more rapidly than the IR band at 2315 cm^{-1} for CD_3CN bound at open Sn sites (Fig. 2.2a). The presence of the 2306 cm^{-1} IR band in Sn-Beta-NH_3 suggests that any NH_3 initially bound to the closed site (Fig. 2.3b) desorbs after exposure to ambient air or vacuum treatment at 373 K (Fig. 2.3c), and forms a closed Sn site similar to that found in the untreated Sn-Beta.

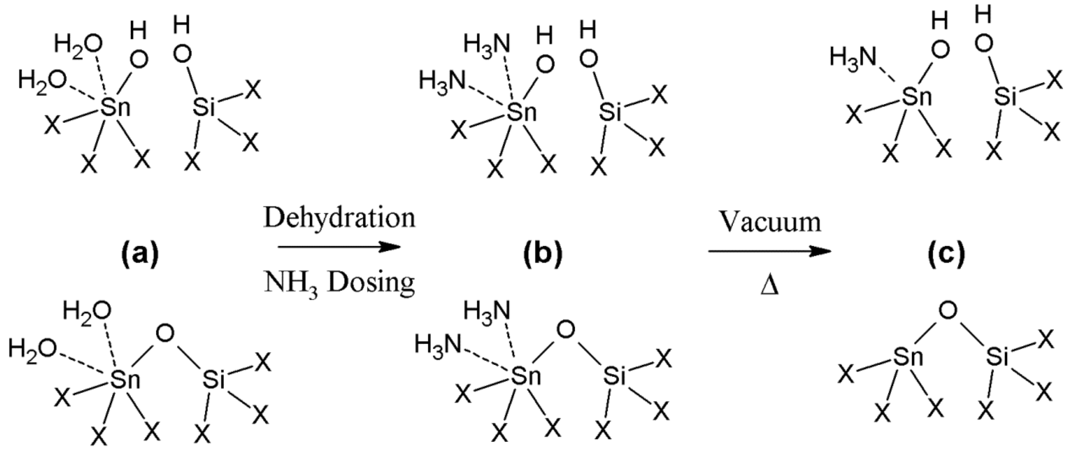

Figure 2.3 Schematic representation of open (top row) and closed (bottom row) sites in Sn-Beta after different treatment procedures. (a) Hydrated open and closed sites after (b) dehydration and saturation with NH_3, followed by subsequent (c) exposure to ambient atmosphere and heated evacuation (373 or 393 K for IR and NMR studies, respectively). “X” denotes framework O-Si units.

The ^{119}Sn NMR spectra of ^{119}Sn-Beta after calcination and exposure to ambient conditions, which allows the Sn centers to become hydrated, shows a main resonance centered at -688 ppm (Fig. 2.4a) for octahedrally coordinated framework Sn[1,2,26]. Upon treatment in vacuum at 383 K to remove the coordinating water, the Sn resonances shift to -423 and -443 ppm (Fig. 2.4d) that are characteristic of tetrahedrally-coordinated framework Sn. We have shown previously through ^{1}H-^{119}Sn CPMAS NMR that the open and closed

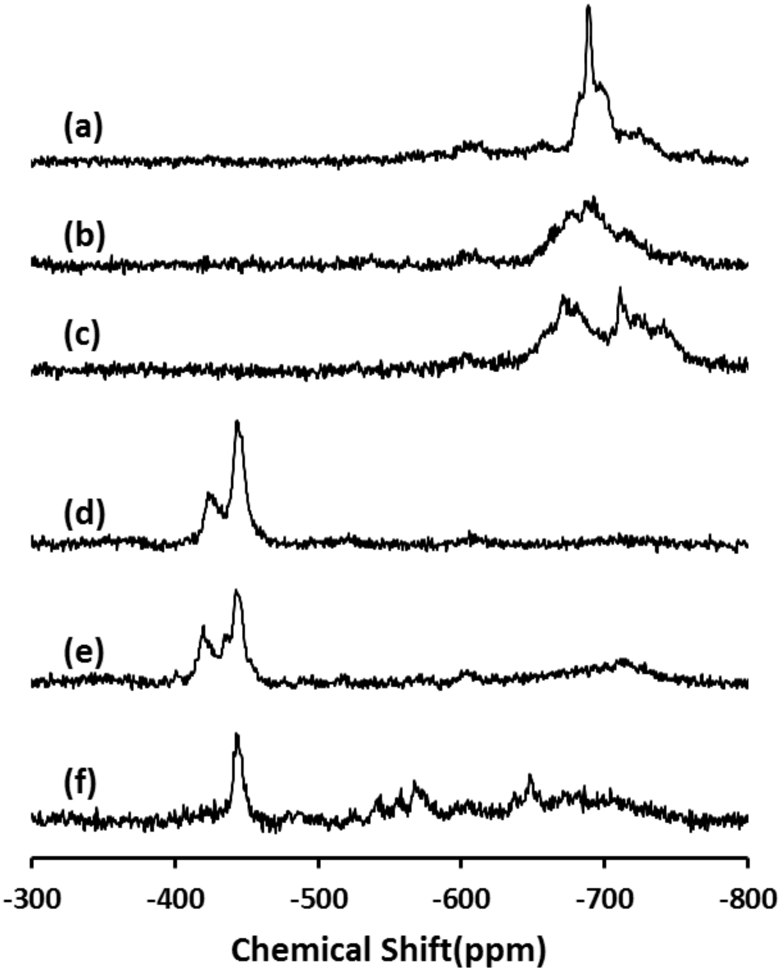

Figure 2.4 ^{119}Sn MAS Solid State NMR spectra of ^{119}Sn-Beta after different treatments: (a) calcination, (b) three Na-exchanges after calcination, (c) NH_3 adsorption after calcination, (d) dehydration after calcination, (e) dehydration after three Na-exchanges and (f) dehydration after NH_3 adsorption.

sites correspond to the resonances centered at -423 and -443 ppm, respectively, because only the -423 ppm resonance was detected when cross-polarization occurred from nearby protons.[2]

Three Na-exchanges performed on ^{119}Sn-Beta decrease the intensity of the sharp -688 ppm resonance (Fig. 2.4a) and form a broad shoulder that begins at -650 ppm and merges into the broader features of the ^{119}Sn-Beta NMR spectrum (Fig. 2.4b). ^{119}Sn NMR spectra for samples after dehydration treatments (vacuum at 398 K, 2h) are shown in Figs. 2.4d-2.4f, with magnified spectra spanning the chemical shift range from -400 to -480 ppm shown in Fig. A20 in Appendix A. Dehydration of the triply-Na-exchanged ^{119}Sn-Beta shows that the introduction of Na^+ to the sample causes a shift of the open Sn site resonance at -423 ppm (Fig. 2.4d) to -419 ppm (Fig. 2.4e), but does not shift the closed site resonance at -443 ppm (Figs. 2.4d and 2.4e). The ^{119}Sn-Beta NMR spectrum of the dehydrated triply-Na-exchanged ^{119}Sn-Beta also contains a small shoulder at -435 ppm that was confirmed not to be a spinning sideband of another resonance (Fig. 2.4e). The ^{1}H-^{119}Sn CPMAS NMR spectrum of dehydrated triply-Na-exchanged ^{119}Sn-Beta shows a resonance at -419 ppm, indicating that these Sn centers have a proton source nearby that cross-polarizes the ^{119}Sn atom (Fig. A21 in Appendix A). This observation suggests that Na^+ exchanges only one of the two available protons present in the silanol and stannanol groups in the dehydrated open Sn site (Fig. 2.1b). The silanol proton is the more likely position for Na exchange (Fig. 2.1c) in light of the proposed mechanisms for glucose isomerization and epimerization on Sn-Beta that require bonding to glucose through the stannanol group.[18] We experienced difficulties in optimizing ^{1}H-^{119}Sn CPMAS conditions, partly due to poor rf pulse coverage over 300 ppm during contact period at high spinning speeds (14 kHz in this case), that led us to acquire ^{1}H-^{119}Sn

CPMAS spectra (e.g., Fig. A21b in Appendix A) by averaging over 30,000 transients. The resonances detected in the tetrahedral range of the dehydrated Na-exchanged ^{119}Sn-Beta do not allow us to characterize the origin of the small -435 ppm shoulder (Fig. 2.4e).

Adsorption of ammonia onto ^{119}Sn-Beta gives rise to two groups of broad resonances centered at -669 and -708 ppm (Fig. 2.4c). Dehydration of this sample (evacuation at 398 K, 2h) gives rise to a resonance for the closed tetrahedral site (-443 ppm, Fig. 2.4f), but not for the open tetrahedral site found in ^{119}Sn-Beta (-423 ppm, Fig. 2.4d). New resonances are detected in the dehydrated spectrum of Na-^{119}Sn-Beta in the -500 to -600 ppm range suggesting the presence of a different Sn coordination environment, which may originate from the open site of Sn-Beta depicted in Fig. 2.1d. The ^{1}H-^{119}Sn CPMAS NMR spectrum of the ^{119}Sn-Beta dehydrated after ammonia adsorption confirms that there is no proton source in the neighborhood of the closed site (-443 ppm), or of any tetrahedrally-coordinated Sn sites, after these treatments (Fig. A22 in Appendix A).

These ^{119}Sn NMR results are consistent with the interpretations of the IR spectra of Sn-Beta-NH_3 after CD_3CN adsorption, and lead us to propose the Sn structures and coordinations in Fig. 2.3. Our findings suggest that the open Sn site is a stronger Lewis acid site than the closed Sn site (Fig. 2.3a), and that it retains adsorbed NH_3 (Fig. 2.3b) after vacuum treatment at 373 K (Fig. 2.3c). Open Sn sites that coordinate one NH_3 ligand would appear as penta-coordinated Sn sites in ^{119}Sn NMR spectra, which we *speculate* could give rise to the resonances detected in -500 to -600 ppm range (Fig. 2.4f). Penta-coordinated open Sn sites with one NH_3 ligand would also bind CD_3CN more weakly than open Sn sites without coordinated NH_3, and may give rise to the 2270 cm^{-1} CD_3CN band observed in IR spectra (Fig. 2.2c). These NMR data also suggest that NH_3 bound to the closed Sn sites desorbs upon dehydration (Fig. 2.3c), such that the behavior of the closed Sn sites in Sn-Beta-NH_3 is similar to their behavior in Sn-Beta samples that have not been treated with NH_3.

2.3.4 Mannose formation with Na containing Sn-Beta

Glucose conversion and fructose and mannose yields after reaction with different Sn-Beta samples in water and methanol (1:100 Sn:glucose ratio, 353 K) for 30 minutes are given in Table 2.2 (data at 10 and 20 minutes given in Table A1 in Appendix A). Fructose is the predominant product formed when Sn-Beta reacts with 1% aqueous glucose solutions (Table 2.2), with carbon balances (84%) that were similar to those we have reported previously.[3] Incomplete closure of carbon balances likely reflects the formation of side products, such as carboxylic acids, furans, and humins [27]. We have previously shown, using solid state ^{13}C MAS NMR, that such side products are present in zeolites after adsorption of sugars on Sn-Beta in water at ambient temperature[1], demonstrating that the formation of side products occurs at early reaction times and that these products remain adsorbed on the zeolite after reaction. In order avoid complications in data analysis associated with sugar degradation side reactions that become more prevalent at higher conversions, we focus here on low glucose conversions (<30%) and the initial fructose and mannose products formed.

In water, Na-exchanged Sn-Beta samples led to similar glucose conversions (6.0-6.8%, Table 2.2) as with Sn-Beta (6.4%, Table 2.2) at equivalent reaction conditions. However, the mannose yield increased systematically from 0.4% to 3.3% and the fructose yields decreased from 5.0% to ~2% with increasing Na content (Table 2.2). Similar results were observed with increasing Na content for Na-Sn-Beta samples synthesized directly (Table 2.2), suggesting that these selectivity differences do not depend on the method used to introduce Na^+ cations into Sn-Beta.

Table 2.2 Glucose conversion (X) and fructose and mannose yields (Y) in H_2O and CH_3OH solvents.

Catalyst	**Solvent**	X_{Gluc}(%)	Y_{Fruc}(%)	Y_{Mann}(%)
Sn-Beta	H_2O	6.4	5.0	0.4
	CH_3OH	23.2	10.3	3.9
Sn-Beta-1Ex	H_2O	6.0	2.1	1.8
	CH_3OH	12.6	3.2	5.0
Sn-Beta-2Ex	H_2O	6.1	1.8	2.5
	CH_3OH	12.2	2.1	6.7
Sn-Beta-3Ex	H_2O	6.8	2.3	3.3
	CH_3OH	12.4	0.0	7.9
Sn-Beta-AW	H_2O	5.4	3.9	0.0
	CH_3OH	16.9	6.1	2.8
Na-Sn-Beta-100	H_2O	6.8	5.1	1.1
	CH_3OH	19.4	8.4	3.3
Na-Sn-Beta-60	H_2O	7.3	4.0	2.7
	CH_3OH	17.2	8.0	3.0
Na-Sn-Beta-30	H_2O	5.8	1.1	3.5
	CH_3OH	6.8	0.0	4.6
Sn-Beta-NH_3	H_2O	3.8	1.9	2.4
	CH_3OH	3.0	0.0	1.9
Sn-Beta-NH_3-Cal	H_2O	5.0	3.2	0.0
	CH_3OH	17.6	7.2	2.6

Reaction conditions: 1% (w/w) glucose solutions, 1:100 metal:glucose ratio, 353 K, 30 min.

Equivalent reaction conditions in methanol led to higher glucose conversions on Sn-Beta (23.2%) and Na-containing Sn-Beta samples (12.2-12.6%) than in water (Tables 2.2 and A1 in Appendix A). As in the case of water, mannose yields increased systematically from 3.9%

to 7.9% and fructose yields decreased systematically from 10.3% to 0.0% with increasing Na/Sn ratio (Table 2.2). Similarly, increasing the sodium content in the synthesis gel of Sn-Beta led to samples that produced higher mannose yields and lower fructose yields (0.0% fructose for Na-Sn-Beta-30, Table 2.2). The large black particles of the amorphous phase impurity formed from synthesis gels with Si/Na ratios less than 30 were isolated from the crystalline solids and did not react with glucose in water, but were able to catalyze glucose-fructose isomerization in methanol.

Na-containing Sn-Beta catalysts showed a higher selectivity towards mannose for reactions in methanol than in water, and fructose-to-mannose ratios significantly increased with increasing reaction time for reactions in water (Tables 2.2 and A1 in Appendix A). These results suggest that sodium decationation could be occurring in aqueous media at a rate that would cause the selectivity to change over the timeframe of the experiment. Thus, we investigated the effects of adding sodium salt to the aqueous reaction solution in order to maintain the sodium content in the solid more effectively during reaction (Tables 2.3 and A2 in Appendix A). When glucose was reacted with Sn-Beta in aqueous NaCl solutions, mannose and fructose were produced in nearly equal yields (4.1% and 4.5%, respectively; Tables 2.3 and A2 in Appendix A), and the solid had a Na/Sn ratio of 2.65 after reaction (Tables 2.3 and A2 in Appendix A), indicating that Na^+ was exchanging into the solid during reaction. Sn-Beta pre-exchanged with Na (Sn-Beta-3Ex) maintained constant mannose selectivity during the course of the reaction when NaCl was added to the aqueous reaction solutions. No fructose or mannose formation was observed without Sn-Beta in aqueous NaCl solution, showing that NaCl does not catalyze isomerization reactions of glucose. These results indicate that the presence of a sodium cation, whether added synthetically or

Table 2.3 Glucose conversion (*X*) and fructose and mannose yields (*Y*) with 0.2g NaCl/g H_2O.

Catalyst	Solvent	X_{Gluc}(%)	Y_{Fruc}(%)	Y_{Mann}(%)
Sn-Beta[a]	H_2O-NaCl	9.8	4.5	4.1
Sn-Beta-1Ex	H_2O-NaCl	10.9	2.6	5.2
Sn-Beta-2Ex	H_2O-NaCl	10.7	2.5	6.0
Sn-Beta-3Ex	H_2O-NaCl	11.5	0.0	7.5

[a] After reaction the catalyst had a Si/Sn and a Na/Sn ratio of 115 ± 30 and 2.65 ± 1.25, respectively, determined by Energy Dispersive X-ray Spectroscopy (EDS).

Reaction conditions: 1% (w/w) glucose solutions, 1:100 metal:glucose ratio; 353 K; 30 min.

exchanged onto the material prior to or during the reaction, shifts the reaction selectivity of Sn-Beta from isomerization to fructose to epimerization to mannose. In water solvent, the Na^+ ion in the active site is replaced by a proton and reverts to a structure that favors fructose formation, while in methanol the Na^+ ion is retained in the active site for longer times and maintains its preference to form mannose. The addition of excess sodium salt to aqueous reaction mixtures increases the extent to which Na exchanges onto Sn-Beta, in turn maintaining the selectivity towards mannose during the course of reaction.

The Sn-Beta sample that was dosed with NH_3 showed lower glucose conversions in both water and methanol solvents (3.0-3.8%, Table 2.2) than Sn-Beta and the Na-containing Sn-Beta samples. Higher glucose conversions were observed with Sn-Beta-NH_3 in water and resulted in a dark yellow post-reaction solution, which may indicate the presence of humins formed from NH_4OH that may have formed *in situ* from the desorption of NH_3. Calcination of the ammonia-dosed sample led to near full recovery of the reactivity in methanol and water (17.6% and 5.0% glucose conversion, respectively, Table 2.2). The suppression of isomerization reactivity on Sn-Beta-NH_3 (Table 2.2) occurs together with the disappearance of the open site CD_3CN IR band at 2315 cm^{-1} (Fig. 2.2c) and with the disappearance of the open site ^{119}Sn NMR resonance at -423 ppm (Fig. 2.4f) in the dehydrated NH_3-dosed Sn-Beta. These data corroborate our proposal that the open site is the active site for the isomerization of glucose to fructose in the absence of sodium, and is the active site for the epimerization of glucose to form mannose in the presence of sodium.

2.3.5 Sodium removal from Sn-Beta

The Sn-Beta-3Ex sample was acid washed to remove Na^+ from the sample (Sn-Beta-AW) and probe whether the effects of sodium on the reactivity of Sn-Beta were reversible. Sn-Beta-AW had much less sodium (Na/Sn = 0.27) than Sn-Beta-3Ex (Na/Sn = 4.85). The glucose conversion and the fructose and mannose yields observed with Sn-Beta-AW were very similar to that of the parent Sn-Beta (Table 2.2). The decrease in mannose yield and concurrent increase in fructose yield after the acid treatment demonstrates that the effects of sodium addition are reversible, and are not a result of a permanent poisoning of the site active for glucose-fructose isomerization.

The effect of the reaction solvent on the recyclability of the catalyst was probed by reacting Sn-Beta-3Ex with glucose in water and methanol under the previously stated reaction conditions (353 K for 30 min in a 1% (w/w) glucose solution) and washing once with the solvent used in the reaction. This cycle was repeated twice and the reaction results after each cycle are shown in Table 2.4. The Na/Sn ratio of the material decreased in each cycle, with a greater extent of sodium loss in the case of aqueous media. A decrease in sodium content in the zeolite after each cycle also led to a decrease in the mannose yield and corresponding increase in the fructose yield (Table 2.4), consistent with the proposal that open Sn sites with Na-exchanged silanol groups are active sites for the epimerization reaction.

Table 2.4. Glucose conversion (X) and fructose and mannose yields (Y) with Sn-Beta-3Ex in CH_3OH and H_2O.

Cycle	**Si/Sn**[a]	**Na/Sn**[a]	**Solvent**	$X_{Gluc.}$(%)	$Y_{Fruc.}$(%)	$Y_{Mann.}$(%)
1	115	4.38	H_2O	8.5	1.7	4.5
2[b]	136	0.93	H_2O	8.6	4.6	3.9
3[b]	123	0.26	H_2O	9.0	6.4	1.2
1	115	4.38	CH_3OH	9.4	0.0	6.5
2[b]	132	1.26	CH_3OH	10.2	1.5	6.0
3[b]	119	0.82	CH_3OH	13.7	3.7	6.2

[a] Determined by Energy Dispersive X-ray Spectroscopy (EDS). Uncertainty in Si/Sn is ± 30. Uncertainty in Na/Sn is ± 1.25.

[b] After the first cycle the catalysts was washed with the solvent used in the reaction and reused under the same reaction and solvent conditions as the previous cycle.

Reaction conditions: 1% (w/w) glucose solutions, 1:100 metal:glucose ratio, 353 K, 30 min.

2.3.6 Glucose isomerization and epimerization mechanisms

Glucose (1% (w/w)) labeled with ^{13}C at the C1 position (^{13}C-C1-glucose) was reacted at 353 K for 30 min with Sn-Beta in water, aqueous NaCl solutions (0.2g NaCl/g H_2O), and methanol as solvents to determine the mechanism of glucose isomerization to fructose and epimerization to mannose. All ^{13}C NMR spectra in Fig. 2.5 show the presence of ^{13}C in the C1 position (resonances at $\delta = 95.8$ and 92.0 ppm) of the α and β pyranose forms of the starting labeled glucose, respectively. The fructose formed from reactions with Sn-Beta in all three solvents showed ^{13}C in the C1 position (resonances at $\delta = 63.8$ and 62.6 ppm) for β-

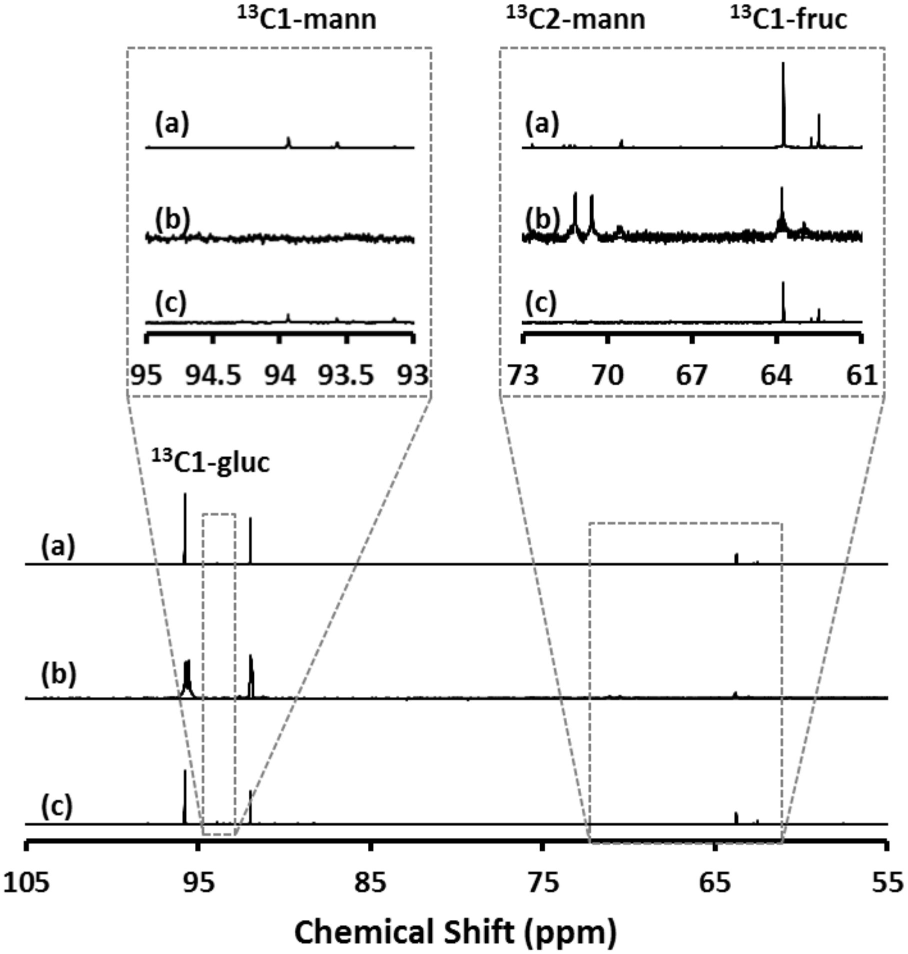

Figure 2.5 ^{13}C NMR spectra for reactant and products with Sn-Beta in a 1% (w/w) ^{13}C1-glucose solution at 353 K for 30 min with the following solvent mixtures (a) H_2O, (b) NaCl-H_2O, and (c) CH_3OH. The abbreviations "gluc", "fruc", and "mann" stand for glucose, fructose, and mannose, respectively.

---

pyranose and β-furanose forms of fructose, as expected from isomerization mediated by 1,2-HS.[1] The ^{13}C label was only observed in the C1 position (resonances at $\delta = 93.9$ and 93.5 ppm) of α and β pyranose forms of mannose with water and methanol solvents in Sn-Beta, indicating that mannose was not formed by a 1,2-CS, but likely via 1,2-HS of fructose products into mannose. In contrast, the ^{13}C label appeared in the C2 position (resonances at $\delta = 70.5$ and 71.1 ppm) of the α and β pyranose forms of mannose with Sn-Beta in aqueous

NaCl solutions, indicating that mannose was formed by the 1,2-CS mechanism of the Bílik reaction.[9]

The isotopic labeling experiments performed with Sn-Beta were also conducted with Sn-Beta-3Ex in water, aqueous NaCl solutions (0.2g NaCl/g H_2O), and methanol as solvents, and the resulting ^{13}C NMR spectra are shown in Fig. 2.6. In water, the fructose products retained the ^{13}C label in the C1 position (resonances at $\delta = 63.8$ and 62.6 ppm), with a lower intensity relative to Sn-Beta, and the mannose product showed the ^{13}C label only in the C2 position (resonances at $\delta = 70.5$ and 71.1 ppm). These results, together with reaction data for earlier reaction times in Table A2 in Appendix A, suggest that Sn-Beta-3Ex initially forms mannose through the 1,2-CS in water, but the loss of sodium from the active site results in the formation of fructose without carbon rearrangement. When methanol or concentrated aqueous NaCl solutions were used as solvents, mannose with ^{13}C in the C2 position was observed as the main product. These results confirm that the switch in reaction mechanism from isomerization to epimerization of sodium-exchanged materials is not directly dependent on the solvent, but rather on the presence of sodium in the active site.

Glucose epimerization into mannose can proceed via reversible enolization upon abstraction of α-carbonyl protons (LdB-AvE rearrangement), or via an intramolecular carbon shift between C1-C2 positions.[28] In order to confirm that the Sn-Beta containing Na^+ was not epimerizing glucose to mannose by abstraction of the α-carbonyl proton, glucose with deuterium at the C2 position (glucose-D2) was used as a reactant. The mannose formed with Sn-Beta-3Ex after 30 minutes at 353 K with 1% (w/w) glucose solution in methanol did not show resonances at $\delta = 93.9$ and 93.5 ppm (Fig. 2.7) that correspond to the C1 positions of the α and β pyranose forms of mannose, respectively. This NMR evidence indicates that with

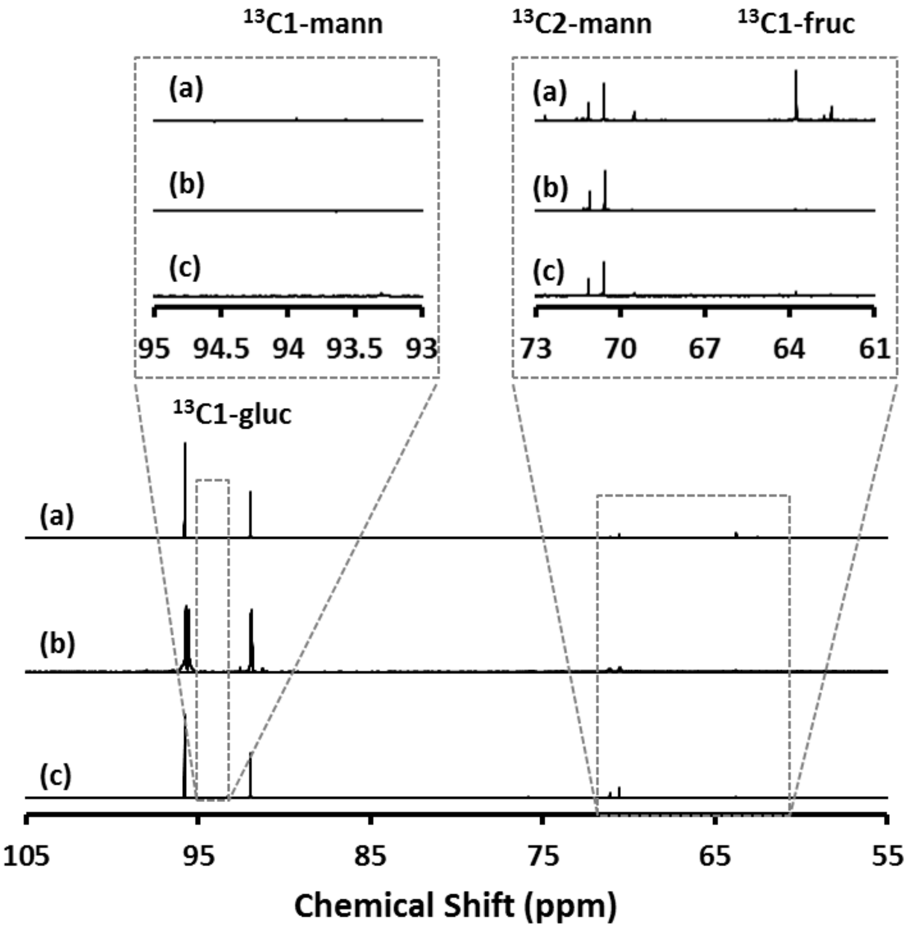

Figure 2.6. ^{13}C NMR spectra for reactant and products with Sn-Beta-3Ex in a 1% (w/w) ^{13}C1-glucose solution at 353 K for 30 min with the following solvent mixtures (a) H_2O, (b) NaCl-H_2O and (c) CH_3OH.

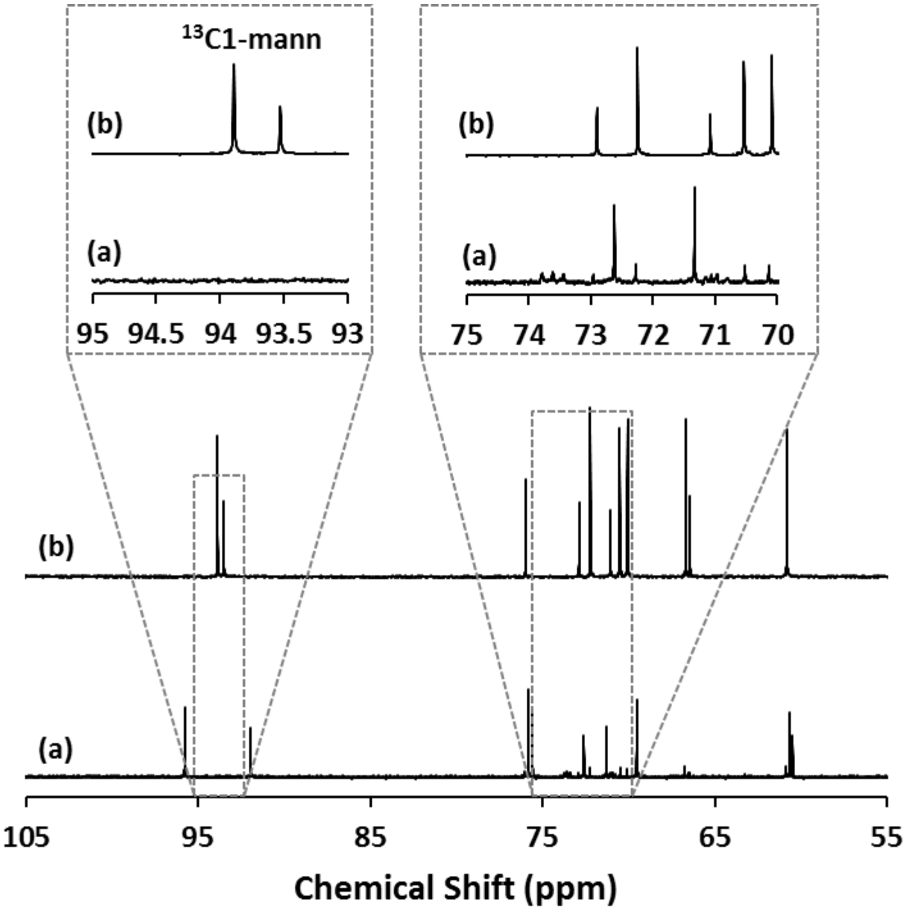

Figure 2.7. ^{13}C NMR spectra for (a) reactant and products with Sn-Beta-3Ex in a 1% (w/w) ^{13}C1-glucose solutions at 353 K for 30 min in CH_3OH and (b) mannose.

the sodium cation in the active site of Sn-Beta, the carbon in the C2 position of glucose moves along with its deuterium to the C1 position by the 1,2-CS to form mannose, as we have observed previously.[2] It is clear that the presence of alkali metal cations in Sn-Beta can determine whether epimerization can occur. In our initial report on glucose epimerization into mannose via 1,2-CS with Sn-Beta in methanol,[2] we did not purposefully add alkali metal cations to the synthesis gel for crystallizing Sn-Beta. We have analyzed the samples used in that study and found them to contain potassium. Although the exact origin of the potassium remains unknown to us at this time, its presence in those samples is likely the reason why we observed epimerization of glucose in methanol solvent.

2.4 Conclusion

Partially-hydrolyzed Sn sites in zeolite beta (denoted as open Sn sites) with proximal silanol groups are shown to be the active site for the isomerization of glucose into fructose via a Lewis-acid mediated 1,2-intramolecular hydride shift mechanism. The exchange of a sodium cation onto the adjacent silanol group of the open Sn sites results in sites that are active for the epimerization of glucose into mannose via a 1,2-intramolecular carbon shift. Sodium cations can be exchanged onto silanol groups in active Sn sites of Sn-Beta either by post-synthetic ion exchange or by addition of low amounts of sodium during synthesis. Acid washing of Na-exchanged Sn-Beta resulted in nearly full recovery of the initial reactivity of the parent alkali-free Sn-Beta, thereby showing that any alterations to the active sites by sodium are reversible. Sodium cations remain exchanged onto Sn-Beta in methanol solvent, but decationation occurs gradually with increasing reaction time in aqueous solvent. The addition of NaCl to aqueous reaction solutions appeared to preserve Na cations exchanged onto silanol groups, as it led to an enhancement in the selectivity towards epimerization of glucose into mannose. These findings, in combination with recyclability studies performed in water and methanol, indicate that Na^+ cations are labile under reaction conditions and that the nature of the solvent influences its lability.

2.5 Acknowledgements

This work was financially supported as part of the Catalysis Center for Energy Innovation, an Energy Frontier Research Center funded by the U.S. Department of Energy, Office of Science, Office of Basic Energy Sciences under Award Number DE-SC0001004. M.O.

wishes to acknowledge funding from the National Science Foundation Graduate Research Fellowship Program under Grant No. DGE-1144469. Any opinions, findings, and conclusions or recommendations expressed in this material are those of the author(s) and do not necessarily reflect the views of the National Science Foundation.

2.6 References

(1) Bermejo-Deval, R.; Assary, R. S.; Nikolla, E.; Moliner, M.; Román-Leshkov, Y.; Hwang, S.-J.; Palsdottir, A.; Silverman, D.; Lobo, R. F.; Curtiss, L. A.; Davis, M. E. *Proc. Natl. Acad. Sci. USA* **2012**, *109* (25), 9727–9732.

(2) Bermejo-Deval, R.; Gounder, R.; Davis, M. E. *ACS Catal.* **2012**, *2* (12), 2705–2713.

(3) Moliner, M.; Román-Leshkov, Y.; Davis, M. E. *Proc. Natl. Acad. Sci. USA* **2010**, *107* (14), 6164–6168.

(4) Nikolla, E.; Román-Leshkov, Y.; Moliner, M.; Davis, M. E. *ACS Catal.* **2011**, 408–410.

(5) Collyer, C. A.; Henrick, K.; Blow, D. M. *J. Mol. Biol.* **1990**, *212* (1), 211–235.

(6) Bhosale, S. H.; Rao, M. B.; Deshpande, V. V. *Microbiol. Rev.* **1996**, *60* (2), 280–300.

(7) Kovalevsky, A. Y.; Hanson, L.; Fisher, S. Z.; Mustyakimov, M.; Mason, S. A; Forsyth, V. T.; Blakeley, M. P.; Keen, D. A; Wagner, T.; Carrell, H. L.; Katz, A. K.; Glusker, J. P.; Langan, P. *Structure* **2010**, *18* (6), 688–699.

(8) Roy, S.; Bakhmutsky, K.; Mahmoud, E.; Lobo, R. F.; Gorte, R. J. *ACS Catal.* **2013**, *3* (4), 573–580.

(9) Hayes, M. L.; Pennings, N. J.; Serianni, A. S.; Barker, R. *J. Am. Chem. Soc.* **1982**, *104* (24), 6764–6769.

(10) Petrus, L. *Chem. Zvesti* **1975**, *29*, 690–693.

(11) Bílik, V.; Petrus, L.; Zemek, J. *Chem. Zvesti* **1978**, *32* (1978), 242–251.

(12) Tanase, T.; Shimizu, F.; Kuse, M.; Yano, S.; Yoshikawa, S.; Hidai, M. *J. Chem. Soc. Chem. Commun.* **1987**, *2* (9), 659.

(13) Tanase, T.; Shimizu, F.; Yano, S.; Yoshikawa, S. *J. Chem. Soc. Chem. Commun.* **1986**, No. 13, 1001–1003.

(14) Tanase, T.; Shimizu, F.; Kuse, M.; Yano, S.; Hidai, M.; Yoshikawa, S. *Inorg. Chem.* **1988**, *27* (23), 4085–4094.

(15) Boronat, M.; Concepcion, P.; Corma, A; Renz, M.; Valencia, S. *J. Catal.* **2005**, *234* (1), 111–118.

(16) Boronat, M.; Corma, A.; Renz, M. *J. Phys. Chem. B* **2006**, *110* (42), 21168–21174.

(17) Khouw, C.; Davis, M. E. *J. Catal.* **1995**, *151* (1), 77–86.

(18) Rai, N.; Caratzoulas, S.; Vlachos, D. G. *ACS Catal.* **2013**, *3* (10), 2294–2298.

(19) Gounder, R.; Davis, M. E. *J. Catal.* **2013**, *308*, 176–188.

(20) Faggin, M. F.; Hines, M. A. *Rev. Sci. Instrum.* **2004**, *75* (11), 4547.

(21) Bellussi, G.; Fattore, V. In *Zeolite Chemistry and Catalysis Proceedings of an International Symposium*; Jacobs, P. A., Jaeger, N. I., Kubelková, L., Wichterlova, B., Eds.; Elsevier, 1991; Vol. 69, pp 79–92.

(22) Miller, F.; Wilkins, C. H. *Anal. Chem.* **1952**, *24* (8), 1253–1294.

(23) Pelmenschikov, A. G.; van Santen, R. A.; Jänchen, J.; Meijer, E. *J. Phys. Chem.* **1993**, *97*, 11071–11074.

(24) Tvaru, Z.; Sobalı, Z. *Microporous Mesoporous Mater.* **1998**, *24*, 223–233.

(25) Boronat, M.; Concepcion, P.; Corma, A.; Navarro, M. T.; Renz, M.; Valencia, S. *Phys. Chem. Chem. Phys.* **2009**, *11*, 2876–2884.

(26) Corma, A.; Nemeth, L. T.; Renz, M.; Valencia, S. *Nature* **2001**, *412* (6845), 423–425.

(27) Holm, M. S.; Saravanamurugan, S.; Taarning, E. *Science* **2010**, *328* (5978), 602–605.

(28) Osanai, S. *Top. Curr. Chem.* **2001**, *215*, 43–76.

Chapter 3

Tandem Catalysis for the Production of Alkyl Lactates from Ketohexoses at Moderate Temperatures

Information contained in Chapter 3 was originally published in: (**Orazov, M.**; Davis, M. E.” *Proc. Natl. Acad. Sci. USA*, **2015**, *112*, 11777–11782. DOI: 10.1073/pnas.1516466112)

Introduction

Chemocatalytic routes for the production of α-hydroxy carboxylic acids (e.g. glycolic acid, lactic acid, 2-hydroxy-3-butenoic acid, and 2,4-dihydroxybutanoic acid) from biomass-derived sugars have been extensively studied in the recent years, as these acids, as well as their esters and lactones, have been recognized to hold large potential as renewable, green platform chemicals for a number of industries (e.g. polymers, solvents, and fine chemicals).[1–7] Considerable progress has been made on the production of lactic acid and alkyl lactates from trioses (glyceraldehyde (GLA) and dihydroxyacetone (DHA)), with nearly quantitative yields achievable with the state-of the art catalysts (e.g. tin-containing zeotypes Sn-Beta and Sn-MFI that are known for their capacity to catalyze 1,2-HS reactions), at moderate temperatures (ca. 100 ^{0}C).[8,9] Similarly, the C_2- and C_4- products (glycolic acid, 2-hydroxy-3-butenoic acid, 2,4-dihydroxybutanoic acid, and esters thereof) can be obtained in good yields when glycolaldehyde, glyoxal, or tetroses (erythrose, threose, and erythrulose) are used as substrates.[4,6] However, the substrates required for these reactions are not easily obtained or isolated from biomass, as the majority of terrestrial biomass comprises cellulose and hemicellulose (polymers of hexoses and pentoses).[5]

To enable the formation of these C_2-C_4 α-hydroxy carboxylic acids from cellulosic and hemicellulosic biomass, retro-aldol reactions are required to fragment the hexose and pentose carbon backbones (r_2 and r_3 in Fig. 3.1). For the common aldoses and ketoses, these C-C

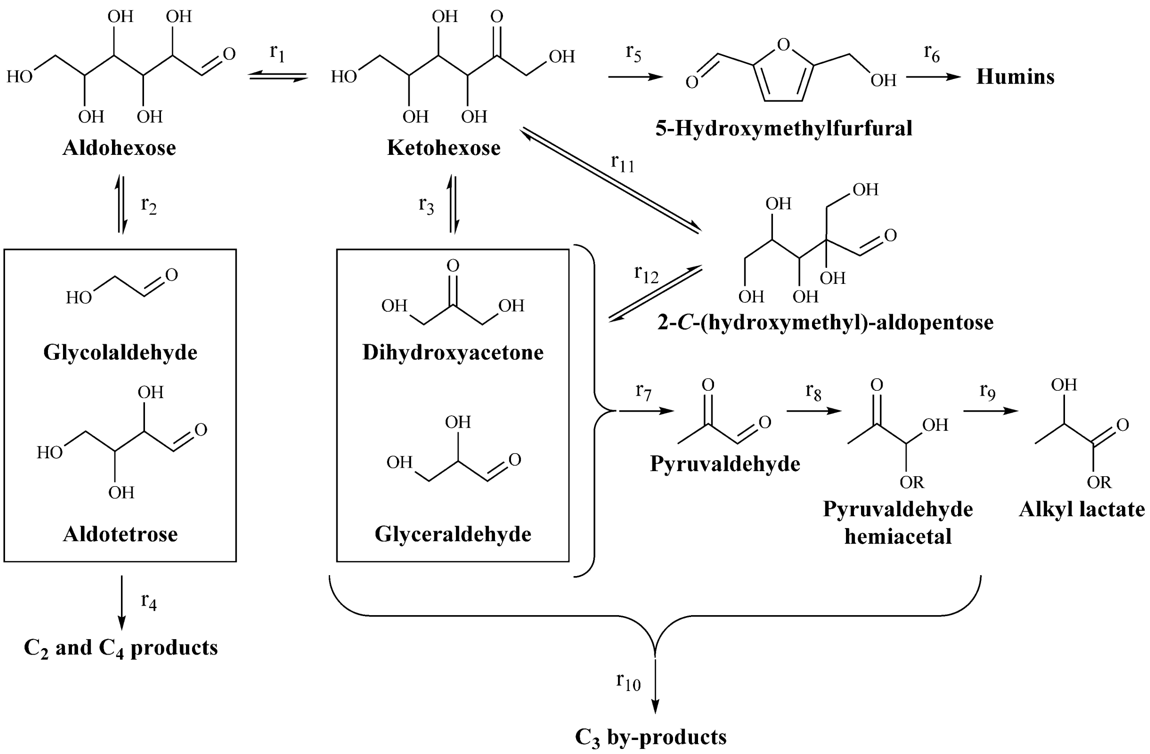

Figure 3.1 Schematic representation of reaction network in which ketohexoses can isomerize to aldohexoses via 1,2-HS (r_1) and to 2-*C*-(hydroxymethyl)-aldopentoses via 1,2-CS (r_{11}) reactions. Retro-aldol reactions of hexose species (r_2, r_3, and r_{12}) lead to the formation of C_2, C_3, and C_4 carbohydrate fragments. Lewis acids can then catalyze the formation of α-hydroxy carboxylic acids from these smaller fragments (e.g. r_7, r_8, and r_9 in the formation of alkyl lactate from trioses). Side reactions, involving dehydration reactions of fructose to 5-HMF (r_5), redox and fragmentation reactions of unstable intermediates, and various humin-forming condensation reactions, lead to loss of yield of desired products.

bond-splitting reactions have large activation energies and unfavorable thermodynamics at low-to-moderate temperatures. As a result, most attempts at the catalytic production of C_2-C_4 α-hydroxy carboxylic acids from hexoses and pentoses have involved high temperature conditions (≥ 160 ^{0}C).[3,10,11] Carbon-basis yields ca. 64-68% of methyl lactate at full conversion were reported for reactions of sucrose catalyzed by Sn-Beta at 160 ^{0}C for 20h.[3] Lower yields ca. 40-44% were reported for monosaccharide substrates in the same study. [3] Recently, methyl lactate yields upwards of 75% from sucrose were achieved with Sn-Beta at 170 ^{0}C, when specific amounts of alkali carbonates were added to the reaction system.[10] Furthermore, the authors suggested that the initial study involving Sn-Beta materials were possibly contaminated by alkali during synthesis, and that alkali-free Sn-Beta recently led to lower yields (30 %).[10]

Low thermal stability of sugars at high temperatures and lack of substrate and reaction specificity of the catalytic sites investigated in the aforementioned systems likely lead to dehydration reactions of ketohexoses to 5-hydroxymethyl furfural (5-HMF) (r_5 in Fig. 3.1). The subsequent fragmentation and coupling reactions of 5-HMF can lead to the formation of insoluble humins that deposit on the catalyst, thereby leading to deactivation and loss of yield of useful products. Large-pore catalysts like Sn-Beta can promote aldose-ketose isomerization reactions (r_1 in Fig. 3.1) of substrates as large as disaccharides[12] because the Lewis acid sites that are active for 1,2-HS reactions are accessible to such species. The same Lewis acid sites have been previously proposed as the active sites in retro-aldol reactions.[9] This inability of Sn-Beta (and other 12-MR materials) to perform size-dependent reaction-discrimination results in aldose-ketose interconversion and parallel retro-aldol reactions of aldo- and keto- hexoses. Therefore, even when ketohexose substrates are used, C_2 and C_4

products derived from aldoses concomitantly form with the more desired C_3 products derived from ketoses (r_4 and r_7-r_{10} in Fig. 3.1, respectively). [3] Thus, catalytic strategies that allow for retro-aldol reactions of hexoses to proceed in the absence of aldose-ketose isomerization are sought for their potential to affect the distribution of C_2, C_3, and C_4 products.

Here, we report the discovery of moderate-temperature (ca. 100 ^{0}C) retro-aldol reactions of various hexoses in aqueous and alcoholic media with catalysts traditionally known for their capacity to catalyze 1,2-CS reactions of aldoses (i.e. various molybdenum oxide and molybdate species, nickel (II) diamine complexes, alkali-exchanged stannosilicate molecular sieves, and amorphous TiO_2-SiO_2 co-precipitates). Because these catalysts do not readily catalyze aldose-ketose interconversion through 1,2-HS, they are candidate co-catalysts for reaction pathways that benefit from aldose- or ketose- specific retro-aldol fragmentation.

3.2 Experimental Methods

3.2.1 Sources of chemicals

MoO_3 (Alfa Aesar, 99.95%), MoO_2 (Sigma-Aldrich, 99%), $H_3PMo_{12}O_{40}\cdot xH_2O$ (Alfa Aesar), MoS_2 (Alfa Aesar, 99%), Na_2MoO_4 (Sigma-Aldrich, 98%), $(NH_4)_6Mo_7O_{24}\cdot 4H_2O$ (Alfa Aesar, 99%), $NiCl_2\cdot 6H_2O$ (Sigma-Aldrich, ≥98%), N,N,N',N'-tetramethylethylenediamine, (Alfa Aesar, 99%), D-fructose (Sigma-Aldrich, ≥99%), L-sorbose (Sigma-Aldrich, ≥98%), D-tagatose (Sigma-Aldrich, ≥98.5%), D-psicose (Sigma-Aldrich, ≥95%), D-hamamelose (Sigma-Aldrich, ≥99.5%), D-Glucose (Sigma-Aldrich, ≥98%), D/L-glyceraldehyde (Sigma-Aldrich, ≥90%), dihydroxyacetone dimer (Alfa Aesar, ≥70%), lactic acid (Sigma-Aldrich, ≥98%), methyl lactate (Sigma-Aldrich, ≥98%), ethyl lactate (Sigma-Aldrich, ≥99%), ethanol (Koptec, anhydrous 200-proof), methanol (Sigma-Aldrich, 99.8%), naphthalene (Sigma-

Aldrich, 99%), tetraethylammonium hydroxide solution (Sigma-Aldrich, 35% in water), tetraethylorthosilicate (Sigma-Aldrich, 98% (w/w)), tin (IV) chloride pentahydrate (Sigma-Aldrich, 98%), hydrofluoric acid (Sigma Aldrich, 54% (w/w) in water), tetraethylammonium fluoride dihydrate (Sigma-Aldrich, 97%), $NaNO_3$ (Sigma Aldrich, ≥99.0%), and NaOH (Alfa Aesar 97%) were purchased and used as received. Chloride form of Amberlite IRA-400 (Sigma-Aldrich) resin was used for immobilization of molybdate salts. TiO_2–SiO_2 co-precipitate (type III, No. 2) was obtained from W. R. Grace (Si/Ti = 56) and was calcined in flowing air (100 mL min^{-1}, Air Liquide, breathing grade) at 580 ^{0}C (ramped up at 1 ^{0}C min^{-1}) for 6 h prior to use.

3.2.2 Synthesis of materials

3.2.2.1 Synthesis of Sn-Beta

Sn-Beta was synthesized according to previously reported procedures (1), as follows: 15.25 g of tetraethylammonium hydroxide solution (35% (w/w) in water) were added to 14.02 g of tetraethylorthosilicate, followed by the addition of 0.172 g of tin (IV) chloride pentahydrate. The mixture was stirred until tetraethylorthosilicate was completely hydrolyzed and then allowed to reach the targeted $H_2O:SiO_2$ ratio by complete evaporation of ethanol and partial evaporation of water. Next, 1.53 g of hydrofluoric acid (54% (w/w) in water) were added, resulting in the formation of a thick gel. The final molar composition of the gel was 1 SiO_2 / 0.0077 $SnCl_4$ / 0.55 TEAOH / 0.54 HF / 7.52 H_2O. As-synthesized Si-Beta (vide infra) was added as seed material (5 wt% of SiO_2 in gel) to this gel and mixed. The final gel was transferred to a Teflon-lined stainless steel autoclave and heated at 140 ^{0}C in a static oven for 25 days. The recovered solids were centrifuged, washed extensively with water, and dried at 100 ^{0}C overnight. The dried solids were calcined in flowing air (100 mL min^{-1}, Air Liquide, breathing grade) at 580 ^{0}C (ramped up at 1 ^{0}C min^{-1}) for 6 h.

3.2.2.2 Synthesis of Si-Beta

Si-Beta was synthesized according to previously reported procedures (1), as follows: 4.95 g of tetraethylammonium fluoride dihydrate was added to 10.00 g of water and 10.001 g of tetraethylorthosilicate. The mixture was stirred until tetraethylorthosilicate was completely hydrolyzed and then allowed to reach the targeted H_2O:SiO_2 ratio by complete evaporation of ethanol and partial evaporation of water. The final molar composition of the gel was 1 SiO_2 / 0.55 TEAF / 7.25 H_2O. The gel was transferred to a Teflon-lined stainless steel autoclave and heated at 140 ^{0}C in a rotation oven (60 rpm) for 7 days. The solids were recovered by filtration, washed extensively with water, and dried at 100 ^{0}C overnight. The dried solids were calcined in flowing air (100 mL min^{-1}, Air Liquide, breathing grade) at 580 ^{0}C (ramped up at 1 ^{0}C min^{-1}) for 6 h.

3.2.2.3 Synthesis of Sn-MFI

Sn-MFI was synthesized with slight modifications to method A reported by Mal et al. (2), as follows: 0.92 g of tin (IV) chloride pentahydrate in 6.08 g of water added to 28.00 g of tetraethylorthosilicate and stirred (uncovered) for 30 min. Next, 48.21 g of tetrapropylammonium hydroxide solution (25% (w/w) in water) was added to the mixture under stirring. After 1 h of additional stirring (uncovered), the remaining water was added, to achieve the final molar composition of the gel of 1 SiO_2 / 0.02 $SnCl_4$ / 0.45 TPAOH / 35 H_2O. The gel was stirred for an additional 30 min (covered), evenly split among three Teflon-lined stainless steel autoclaves, and heated at 160 ^{0}C in a static oven for 48 h. The solids were recovered by filtration, washed extensively with water, and dried at 100 ^{0}C overnight. The dried solids were calcined in flowing air (100 mL min^{-1}, Air Liquide, breathing grade) at 580 ^{0}C (ramped up at 1 ^{0}C min^{-1}) for 6 h.

3.2.2.4 Na-Exchange of Sn-Beta

Three successive sodium ion exchanges were performed according to previously described procedure (3) as follows: calcined Sn-Beta was stirred in a solution of 1 M $NaNO_3$ and 10^{-4} M NaOH in distilled water. Each ion exchange step was carried out for 24 hours at ambient temperature, using 45 mL of exchange or wash solution per 300 mg of starting solids. The material was recovered by centrifugation, and washed three times with 1 M $NaNO_3$ in distilled water. The final material was dried at ambient temperature overnight by an impinging flow of air.

3.2.2.5 $H_3PW_{12}O_{40}$ and $(NH_4)_6Mo_7O_{24}$ exchanged resins

$H_3PW_{12}O_{40}$ and $(NH_4)_6Mo_7O_{24}$ were immobilized by ion exchanging the chloride form of Amberlite IRA-400. In each procedure, *n* meq of ion capacity worth of resin was used per 1 meq of anion to be immobilized, where *n* is the charge of the anion. The resin was suspended in an aqueous solution of anion for 24 h, filtered, washed extensively with water, and dried at ambient temperature overnight by an impinging flow of air.

3.2.3 Reaction analysis

Carbohydrate analysis and fractionation were performed via high performance liquid chromatography on an Agilent 1200 system equipped with refractive index and evaporative light scattering detectors. An Agilent Hi-Plex Ca column held at 80 ^{0}C was used with ultrapure water as the mobile phase (flow rate of 0.6 mL min^{-1}). Quantitative GC/FID analysis of alkyl lactates was performed on an Agilent 7890B GC system equipped with a flame ionization detector and an Agilent HP-5 column. Qualitative GC/MS analysis of side-products was performed on an Agilent 5890 GC system with an Agilent 5970 mass spectrometer and an Agilent DB-5 column. Liquid ^{1}H and ^{13}C NMR spectra were recorded with a Varian INOVA 500 MHz spectrometer equipped with an auto-x pfg broad band probe. All liquid NMR analysis was performed in D_2O solvent, with 4,4-dimethyl-4-silapentane-1-sulfonic acid (DSS) as an internal standard.

Reactions were performed in 10 mL thick-walled crimp-sealed glass reactors (VWR) that were heated in a temperature-controlled oil bath. A typical reaction procedure involved: addition of desired amount of catalysts (i.e. MoO_3, Sn-MFI, etc.), carbohydrate substrate (i.e. D-fructose, DHA, etc.), and solvent (i.e. EtOH, MeOH, etc. with pre-dissolved naphthalene as internal standard) to reactor, sealing of reactor with crimp-top, agitation of reactor at ambient temperature until dissolution of substrate, and placement of reactor in the oil bath at desired temperature. Aliquots (~100 μL) were extracted at indicated times, filtered with a 0.2 μm PTFE syringe filter, and analyzed by GC/FID. For reactions with $[Ni(N,N,N',N'\text{-}Me_4en)_2]Cl_2$, aliquots were agitated with 20 mg of Dowex 50WX2 (hydrogen form) resin to remove nickel (II) species prior to filtration. For product identification by HPLC, liquid

NMR, or GC/MS, internal standard was excluded and the entire reactor content was used. Rotary evaporation was used to remove solvent when needed.

3.3 Results and Discussion

3.3.1 Retro-Aldol Reactions and 1,2-CS Catalysts. During our recent investigation of epimerization reactions of aldohexoses on alkali-exchanged Sn-Beta materials, a change in the reaction pathway from a 1,2-HS to a 1,2-CS upon alkali exchange was observed. [13] This 1,2-CS pathway in aldohexoses is analogous to those previously reported for molybdate and nickel (II) diamine catalyzed reactions of these aldoses (also known as Bilik reaction), in which simultaneous C-C bond breaking and forming steps were proposed to occur (Fig. 3.2). [14,15] Reactions of ketoses catalyzed by molybdates and nickel (II) diamines were found to proceed through analogous pathways, to form branched sugars (2-*C*-(hydroxymethyl)-aldoses (r_{11} in Fig. 3.1). [16–18] In addition to the branched sugars, small amounts of ketose isomers were observed (e.g. when D-fructose was reacted with molybdate, the branched sugar D-hamamelose formed, as well as small quantities of ketose isomers: sorbose, psicose, and tagatose). [16,19,20] The formation of ketose isomers was attributed to competing hydride shift side reactions. [20]

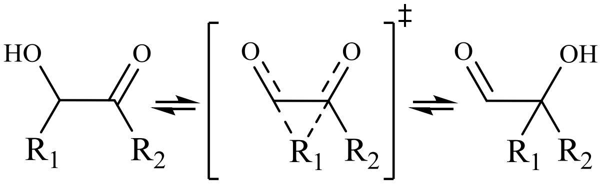

Figure 3.2 Schematic representation of a 1,2-CS reaction (R_2 = H for aldoses or R_2 = CH_2OH for ketoses, and R_1 represents the remainder of the saccharide) that involves simultaneous breaking and forming of C-C bonds.

We observed the formation of the same branched sugar (D-hamamelose) and ketose isomers, when fructose was reacted with alkali-exchanged Sn-Beta at 100 ^{0}C. Interestingly, small quantities of retro-aldol products, DHA and GLA, were also observed in the HPLC chromatograms and NMR spectra of unseparated reaction solutions. The presence of DHA and GLA put the mechanism of ketose isomer formation in question, as it is possible to form all of the ketohexoses through non-stereospecific aldol condensation of DHA and racemic GLA. Water-dissolved MoO_3 (H_2MoO_4) was tested for similar products, when fructose was reacted at 100 ^{0}C. Initial formation of hamamelose, DHA, and GLA was observed. Subsequently, sorbose, tagatose, and psicose began to form, without significant changes in the DHA and GLA concentration. Quantification of products was not performed due to a multitude of partially overlapping peaks in HPLC chromatograms and NMR spectra; however, fructose and sorbose were eventually observed in substantially greater quantities than tagatose, psicose, and hamamelose. Fractionation of product solutions and ^{1}H and ^{13}C NMR were used to confirm the presence of DHA, GLA, fructose, sorbose, tagatose, psicose, and 2-*C*-(hydroxymethyl)-aldopentoses (Figs. B1-B6 in Appendix B). These results suggested that some of the ketose isomers may form as aldol condensation products of DHA and GLA, rather than directly from fructose through hydride shift reactions, as was previously hypothesized. The unfavorable equilibria of retro-aldol reactions at these moderate temperatures may be responsible for the low concentrations of DHA and GLA. The reverse reaction, aldol coupling, is a logical secondary reaction that can form the more stable ketohexose side-products. The possibility of aldol coupling was confirmed by reacting a mixture of DHA and GLA under the same conditions, resulting in complex mixture of products containing ketohexoses and 2-*C*-(hydroxymethyl)-aldopentoses.

While the low production of 2-*C*-(hydroxymethyl)-aldopentoses may be due to thermodynamic limitations (e.g. hamamelose-fructose equilibrium K_{eq} ~14)[16], tagatose and psicose may form in small quantities due to kinetic reasons. The tetradentate open-chain ketohydrol fructose-molybdate complex that was previously hypothesized to be the key species in the fructose-hamamelose rearrangement catalyzed by water-dissolved molybdates is shown in Fig. 3.3 (along with analogues for other ketohexoses).[16] ^1H and ^{13}C NMR studies of the molybdate complexes of ketohexoses suggest that only fructose and sorbose form detectable amounts of tetradentate molybdate complexes, while psicose and tagatose tend to form tridentate complexes.[21] These results suggest that aldol coupling reactions that would result in the formation of tagatose and psicose would proceed through more energetic transition states, resulting in slow formation kinetics. Additionally, the same study provides estimates of the fraction of a given ketohexose that exists in a molybdate complex, and indicates that the psicose and tagatose complexes are more favorable, with 80-95% of the sugars bound to Mo (at stoichiometric Mo/monosaccharide amounts), whereas these values for sorbose and fructose are only 15-20%.[21] If the retro-aldol reactions of ketohexoses proceed through tetradentate molybdate complexes, these results suggest that the formation

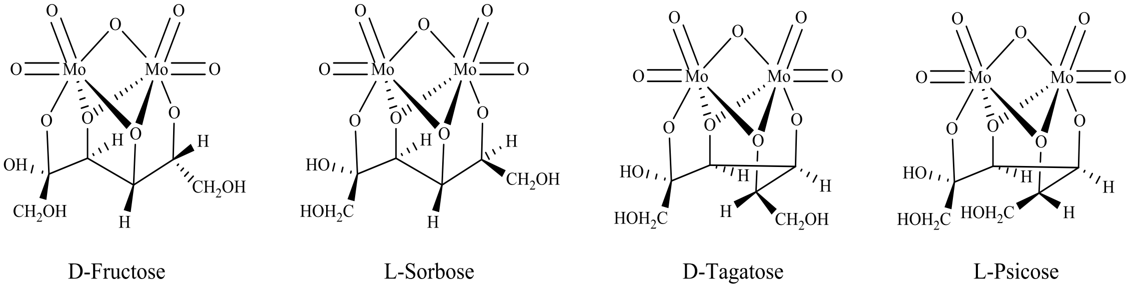

Figure 3.3 Fructose, sorbose, tagatose, and psicose molybdate complexes hypothesized to be involved in 1,2-CS rearrangements to corresponding 2-*C*-(hydroxymethyl)-aldopentoses.

of tagatose and psicose may reduce the fraction of catalytically active molybdate species through competitive binding and formation of tridentate complexes. A similar NMR study of molybdate and tungstate complexes of fructose and sorbose provides conflicting interpretations of the complex structures.[22] The multinuclear NMR data from this study suggests that both sugars form O-1,2,2',4 acyclic complexes, which do not involve O-3 coordination, in high proportions. [22] It is important to note that these results were obtained at pH ca. 7.5, while, at lower pH, additional minor complexes were observed, with proposed O-3,4,5,6 coordination.[22] Molybdate-catalyzed epimerization of aldohexoses was reported to be ~20-fold faster at pH 1.5-3.5 than at pH 5.9, and a lack of reaction was observed at pH higher than 6.0.[20] Furthermore, 3-deoxy-aldohexoses do not undergo epimerization reactions; thus, binding through the hydroxyl group adjacent to the carbonyl may be required for 1,2-CS catalyzed by molybdates.[23] The combination of these results illustrates the complexity of molybdate-sugar equilibria and suggests tetradentate complexes of fructose and sorbose may be crucial to retro-aldol reactions.

While binuclear molybdate species were implicated in epimerization reactions catalyzed by water-dissolved MoO_3 higher structures containing molybdate ions were later shown to catalyze epimerization reactions (e.g. Keggin structure molybdenum-based polyoxometalates,[24] and heptamolybdate species immobilized on anion-exchange supports[25]). Similarly, we observed promotion of retro-aldol reactions of fructose by the $H_3PMo_{12}O_{40}$ Keggin ion, and by $(NH_4)_6Mo_7O_{24}$, both as homogeneous catalysts and when immobilized onto an anion-exchange support (e.g. Amberlite IRA-400, chloride form). Soluble and insoluble molybdate salts (e.g. Na_2Mo_4 and $ZnMoO_4$, respectively), as well as insoluble solids containing Mo (IV) (e.g. MoO_2, and MoS_2) also appear catalytically active in epimerization and retro-aldol reactions of fructose. At this time, it is not clear if the nominal form of each chemical is the catalytically active one, or if unknown catalytic species are generated in situ at reaction conditions. While—due to the aforementioned complications in quantification—we could not directly assess the performance of each catalyst in retro-aldol reactions, we did observe differences in kinetics (*vide infra*) of the lactate-forming reaction cascade when different Mo-containing species were used for the retro-aldol component of the pathway (i.e. r_3 of cascade consisting of r_3, and r_7-r_9 in Fig 3.1).

Tungstate analogues of molybdate-monosaccharide complexes were reported to have formation constants that are 2-3 orders of magnitude higher than molybdates.[22] Such strong binding may be responsible for the apparent lack of catalytic activity of H_2WO_4 and $H_3PW_{12}O_{40}$ in the epimerization of glucose to mannose at mild conditions. [24,26] Similarly, in our experiments, tungstate species performed poorly, but did produce species consistent with retro-aldol reactions of hexoses at long reaction times. Interestingly, at high temperatures ($\geq$ 150 ^{0}C), H_xWO_3 was recently reported to catalyze retro-aldol reactions of glucose and fructose, when coupled with a Ru/C-promoted H_2-reductive step to produce glycols. [27] An apparent activation energy of 141.3 kJ/mol for the retro-aldol reaction of glucose was reported, while the apparent activation energy for further reactions of glycolaldehyde (including aldol condensation) was estimated to be 52.7 kJ/mol.[27] These results illustrate the high barriers of retro-aldol reactions that encouraged high-temperature conditions to be investigated in previous studies, and suggest additional (reductive) catalytic routes not considered here that could benefit from lower temperature retro-aldol catalysis.

Nickel (II) diamine complexes in methanolic solutions were previously shown to catalyze the 1,2-CS in aldoses[15] and 2-*C*-(hydroxymethyl)-aldopentose formation from ketohexoses[18] ca. 60 ^{0}C. We observed that the complex of tetramethylethylenediamine with $NiCl_2$ ($[Ni(N,N,N',N'\text{-}Me_4en)_2]Cl_2$) in methanol also accelerated the retro-aldol part of the methyl lactate-producing reaction cascade ca. 100 ^{0}C. The investigators of 1,2-CS catalysis in aldoses by nickel (II) diamine complexes used stoichiometric amounts of nickel complexes and aldoses, noting that the nickel complexes can also be used in catalytic amounts, but deactivate after a few turnovers.[15] Similarly, deactivation was inferred from our data due to an early decrease in methyl lactate production rate. This deactivation is potentially related to the formation of a white precipitate that was observed when $[Ni(N,N,N',N'\text{-}Me_4en)_2]Cl_2$ dissolved in MeOH was allowed to stand at ambient temperatures for extended times. While nickel (II) diamines do not appear to be stable catalysts at reaction conditions, they are exceptionally active 1,2-CS catalysts (with 1,2-CS reactions of aldoses observed as low as 25 ^{0}C), and may be good model systems for retro-aldol reactions catalyzed by 1,2-CS catalysts, as their sugar complexes are isolable and amenable to characterization through EXAFS and X-ray crystallography.[15]

3.3.2 Coupling Retro-Aldol Reactions with 1,2-HS for Lactate Production. Materials that can catalyze the 1,2-CS in aldoses were reported to be poor 1,2-HS catalysts for the same substrates, as the production of ketoses was not detected.[20] Because the formation of lactate from trioses by Lewis acid catalysts has been shown to involve a 1,2-HS (r_9 in Fig. 3.1),[28] an efficient route to the more thermodynamically stable lactate products is not enabled by the retro-aldol catalysts described above, resulting in triose accumulation and recombination through aldol reactions. Addition of a 1,2-HS co-catalyst (Sn-MFI with Si/Sn = 70 ± 6, fluoride-free synthesis)[29] to an 1 wt% fructose, 0.2 wt% MoO_3 aqueous solution enabled formation of lactic acid at 100 ^{0}C. However, quantitative ^{1}H NMR data suggest that lactate forms strong pH-dependent complexes with molybdate species (see Fig. B7 in Appendix B), and that lactate production stops once the stoichiometric amount of 2 mol lactate per mol molybdate is produced. This inhibition of catalysis by product coordination is consistent with the previously reported pH-dependent molybdate-lactate complex formation, with an estimated pK of formation of -49 at pH = 4.5.[30]

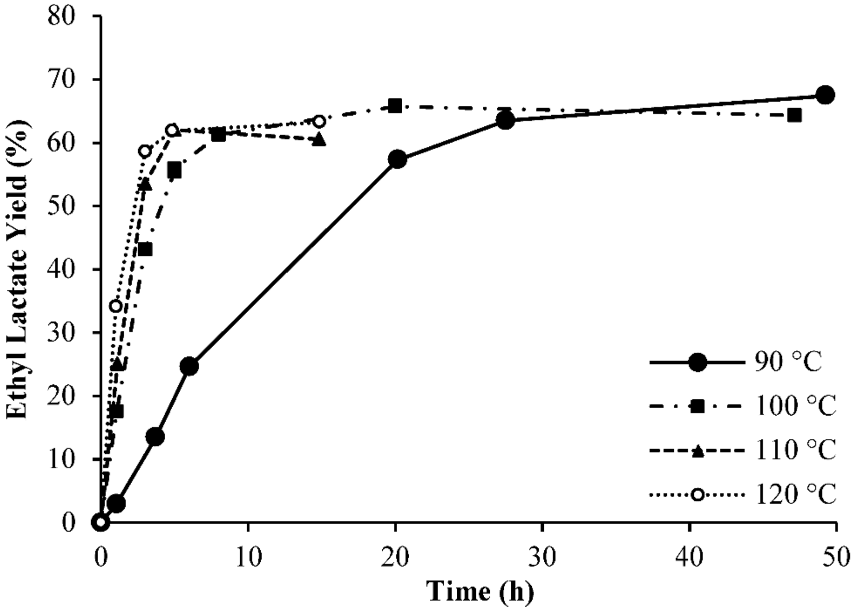

Figure 3.4 Ethyl lactate yield as a function of time at different temperatures (indicated in legend). Reaction conditions: 80 mg MoO_3; 100 mg Sn-MFI; 50 mg D-fructose; 4.9 g EtOH; 50 mg naphthalene as internal standard.

When the reactions of fructose with MoO_3 and Sn-MFI were performed in alcoholic media, corresponding alkyl lactates were produced in good yields (e.g. see Fig. 3.4 for a representative graph of ethyl lactate production from fructose as a function of time at different temperatures, Fig. B8 in Appendix B for ^{1}H NMR of methyl lactate product, and Table 3.1 for the maximum observed yields of lactate products under various reactions).

Turnover numbers (TON) in excess of unity indicate that alkyl lactate production is truly catalytic in such reactions (e.g. for Reaction 6 in Table 1, the TON ≥ 5.5 based on Mo atoms for the retro-aldol reaction of fructose, and TON ≥ 16.1 based on Sn atoms for lactate formation from the resulting trioses). For reactions performed in alcoholic media, MoO_3 particles remained undissolved and progressively turned a dark-blue color, suggesting the possibility of partial reduction of MoO_3 or coverage with alcohol-insoluble molybdate-lactate complex. Both possibilities could contribute to lowering of lactate yield. Rapid, reversible ketalization of ketoses by the solvent was observed, and may influence the reaction kinetics.

A number of parameters were varied in order to maximize the yield of alkyl lactate products and gain further insight into the limiting factors of this reaction network. Plots analogous to Fig. 3.4 for reactions in the following discussion can be found in Figs. B9-B17 in Appendix B. Data in Fig. 3.4 shown that, at otherwise-fixed conditions, increase in temperature resulted in an increased rate of ethyl lactate formation, but ultimate ethyl lactate yield was not significantly impacted, suggesting that side reactions may have comparable activation energies to the limiting steps in lactate production. At 100 ^{0}C, with constant Sn-MFI amount, increasing the amount of MoO_3 catalyst lead to a faster approach to ultimate lactate yield, but the increase in rate was not proportional to the change in MoO_3 amount, and a potential induction time is observed for the reaction with the lowest MoO_3 content. Conversely, fixing the amount of MoO_3, and varying the amount of Sn-MFI suggested that two regimes are possible: one in which ethyl lactate production is limited by retro-aldol

Table 3.1 Maximum observed yields of lactic acid or alkyl lactates obtained under various reaction conditions

R[a]	1,2-CS catalyst	Mass (mg)	1,2-HS catalyst	Mass (mg)	Substrate	wt% of solution	Solvent	Max Yield (%)[b]
1	MoO_3	80	Sn-MFI	100	Fructose	1	EtOH	67.4
2	MoO_3	80	Sn-MFI	100	Fructose	1	EtOH	65.7
3	MoO_3	80	Sn-MFI	100	Fructose	1	EtOH	61.9
4	MoO_3	80	Sn-MFI	100	Fructose	1	EtOH	63.2
5	MoO_3	20	Sn-MFI	100	Fructose	1	EtOH	67.7
6	MoO_3	5	Sn-MFI	100	Fructose	1	EtOH	69.2
7	MoO_3	80	Sn-MFI	200	Fructose	1	EtOH	68.6
8	MoO_3	80	Sn-MFI	50	Fructose	1	EtOH	46.7
9	MoO_3	80	Sn-MFI	100	Fructose	5	EtOH	21.0
10	MoO_3	80	Sn-MFI	100	Fructose	0.2	EtOH	74.6
11	-	0	Sn-MFI	100	Fructose	1	EtOH	3.9
12	-	0	Sn-MFI	100	DHA/GLA	0.5/0.5	EtOH	86.5
13	MoO_3	80	-	0	Fructose	1	EtOH	13.0
14	MoO_3	80	-	0	DHA/GLA	0.5/0.5	EtOH	14.6
15	MoO_2	80	Sn-MFI	100	Fructose	1	EtOH	58.1
16	MoS_2	80	Sn-MFI	100	Fructose	1	EtOH	48.3
17	$H_3PMo_{12}O_{40}$	10	Sn-MFI	100	Fructose	1	EtOH	51.6
18	$Ni(Me_4en)_2Cl_2$	2	Sn-MFI	100	Fructose	1	MeOH	17.6[c]
19	$Ni(Me_4en)_2Cl_2$	20	Sn-MFI	100	Fructose	1	MeOH	45.1[c]
20	TiO_2-SiO_2	200	Sn-MFI	100	Fructose	1	MeOH	7.7
21	MoO_3	80	Sn-Beta	50	Fructose	1	EtOH	51.0
22	MoO_3	80	Sn-Beta	50	Glucose	1	EtOH	40.2
23		0	Sn-Beta	50	DHA	1	EtOH	88.4
24	MoO_3	80	Sn-MFI	100	Hamamelose	1	EtOH	70.2
25	MoO_3	80	Sn-MFI	100	Sorbose	1	EtOH	67.6
26	MoO_3	80	Sn-MFI	100	Psicose	1	EtOH	57.6
27	MoO_3	80	Sn-MFI	100	Tagatose	1	EtOH	46.1
28	MoO_3	80	Sn-MFI	100	Fructose	1	MeOH	68.2
29	MoO_3	80	Sn-MFI	100	Fructose	1	10/90 H_2O/EtOH	22.7
30	MoO_3	10	Sn-MFI	100	Fructose	1	H_2O	26.7[d]

Reaction conditions: for each reaction, the catalyst amounts, substrate concentrations, solvents, and temperature used are indicated in the table. Each reaction involving alcoholic solvents was performed with 4.9 g of solvent and 50 mg naphthalene as internal standard for GC-FID quantification. (cont.)

[a] R = Reaction number

[b] Maximum yield achieved for reaction, on % carbon basis.

[c] For reactions with $[Ni(N,N,N',N'\text{-}Me_4en)_2]Cl_2$, aliquots were agitated with 20 mg of Dowex 50WX2 (hydrogen form) resin to remove nickel (II) species prior to filtration.

[d] For the reaction performed in water, no naphthalene was added, and 4,4-dimethyl-4-silapentane-1-sulfonic acid, sodium salt (DSS) was used as an external standard for quantitative ^{1}H-NMR.

---

reactions (i.e. excess Sn-MFI catalyst can deplete trioses faster than they are generated) and one in which the ethyl lactate production from trioses is kinetically relevant (i.e. insufficient Sn-MFI leads to accumulation of trioses). In the former scenario, the ultimate yield of ethyl lactate was higher than in the latter. Similarly, at fixed amounts of both catalysts, lower initial substrate concentrations resulted in higher ethyl lactate yields. These results suggest that high concentrations of substrate and intermediates are conducive to side-product formation and that rapid conversion to stable alkyl lactate products can reduce the extent of irreversible side reactions.

A set of control experiments that illustrate the importance of the combination of the two catalysts were performed. In the absence of MoO_3 co-catalyst, Sn-MFI was unable to convert fructose to ethyl lactate in significant yields, even though high yields of ethyl lactate were rapidly achieved by Sn-MFI alone when an equimolar mixture of DHA and GLA were used as substrates. Conversely, without Sn-MFI, MoO_3 slowly catalyzed the formation of ethyl lactate from fructose, with an ultimate ethyl lactate yield being considerably lower than in the mixed-catalyst system. Additionally, the use of equimolar DHA and GLA mixture as starting substrate did not result in significantly higher yields of ethyl lactate when MoO_3 was used by itself, further illustrating the rapidity of side reactions of trioses when a catalytic path to the thermodynamically stale lactate products is not present.

As discussed above, other Mo-containing 1,2-CS catalysts (e.g. MoO_2, MoS_2, $H_3PMo_{12}O_{40}$, Na_2MoO_4, $(NH_4)_6Mo_7O_{24}\cdot4H_2O$, $ZnMoO_4$, and $CaMoO_4$) were also able to accelerate alkyl lactate production from fructose when paired with Sn-MFI (e.g. see Fig. B13 in Appendix B for the first three). While the conditions for these catalysts have not been optimized, all alternative Mo-containing catalysts resulted in lower ethyl lactate yields than were achieved with MoO_3. Similarly $[Ni(N,N,N',N'\text{-}Me_4en)_2]Cl_2$ in methanol also accelerated the retro-aldol part of the reaction cascade at 100 ^{0}C, but deactivated after a few turnovers. Amorphous TiO_2-SiO_2 co-precipitates were reported to slowly catalyze the 1,2-CS of glucose in methanol [12]. Here, we saw only a minor increase in lactate production upon addition of TiO_2-SiO_2 co-precipitate to Sn-MFI, and its use was not further investigated.

Sn-Beta (Si/Sn = 95 ± 14, fluoride synthesis)[31] can be used in place of Sn-MFI for the second part of the reaction cascade. Furthermore, when coupled with MoO_3, under conditions where lactate formation from trioses was kinetically relevant, Sn-Beta performed better than Sn-MFI.[9] This result is consistent with the reported faster kinetics of alkyl lactate synthesis from trioses by Sn-Beta than Sn-MFI. Because Sn-Beta can also catalyze glucose-fructose-mannose isomerization reactions through the 1,2-HS and, to some degree, retro-aldol reactions of hexoses, Sn-Beta was not used as the catalyst of choice in the current study, in order to avoid additional complicating factors in the reaction network. To illustrate this point, data in Fig. B15 in Appendix B show ethyl lactate formation from glucose when Sn-Beta is used in combination with MoO_3, indicating that aldose-ketose isomerization reactions occur on kinetically relevant timescales. Another noted benefit of using Sn-MFI as the 1,2-HS catalyst is that it can be easily synthesized in the absence of fluoride[29] (a frequently raised concern for large scale synthesis of catalysts to be used for biomass processing e.g. Sn-Beta). In principle, even more economically accessible materials that can catalyze lactate formation from trioses (e.g. post-synthetically treated Al zeolites[32] or homogeneous Lewis acids[33]) may be paired with the retro-aldol catalysts reported in this study to produce alkyl lactates from hexoses at mild conditions.

Sn-Beta (and other Lewis-acid containing zeotypes, e.g. Ti-Beta) has also been shown to catalyze the 1,2-CS reactions of aldoses in aqueous solutions when either borate[34] or alkali salts[13] are present. The recently reported increase in methyl lactate production by Sn-Beta from fructose in methanol at 170 ^{0}C (from 16% to 57%) upon alkali carbonate addition[10] is consistent with formation of 1,2-CS sites upon alkali exchange of open sites in Sn-Beta. Sn-Beta systems with added borate and alkali salts were reported to be pH sensitive and are not efficient 1,2-CS catalysts in acidic conditions.[13,34] Furthermore, if Sn-MFI is used as a size-dependent 1,2-HS catalyst in conjunction with borate- or alkali- modified Sn-Beta, borate or alkali ions have the capacity to enter the Sn-MFI pores and influence the efficiency of lactate production from trioses. Thus, coupling of lactic acid or alkyl lactate production with retro-aldol reactions in mixed Sn-based zeotype systems was not studied here, but may warrant further investigation for the potential to affect the distribution of C_2, C_3, and C_4 products by limitation of aldose-ketose interconversion.

Formation of other 2-ketohexoses and 2-*C*-(hydroxymethyl)-aldopentoses in MoO_3-catalyzed reactions of fructose was discussed above. The differences in interactions between the various molybdate and hexose species may impact the rate of retro-aldol reactions. To test for this possibility, psicose, sorbose, tagatose, and hamamelose were reacted under the same conditions as fructose. The rate of ethyl lactate formation from hamamelose was nearly identical to that from fructose. The initial rates of ethyl lactate formation from sorbose and psicose were lower than from fructose, but comparable ultimate yields of ethyl lactate were observed. Tagatose appeared to be the slowest to react. While it is clear that formation of ketohexose side-products can impact the ultimate kinetics of ethyl lactate production, it is not certain whether the difference in the rates of retro-aldol reactions among these substrates is due to differences in energy barriers or due to reduction of available catalytic sites through competitive coordination in binding configurations that are not activated for retro-aldol reactions.

At 160 ^{0}C, Sn-Beta was reported to perform much better for lactate production from sucrose in methanol than in ethanol, isopropanol, or water.[3] In the case of MoO_3/Sn-MFI, no significant differences in kinetics or ultimate yields of alkyl lactates were observed between methanol and ethanol solvents, at 100 ^{0}C. However, when 10 wt% water / 90 wt% ethanol was used, the ultimate yield of ethyl lactate was significantly lower than for neat ethanol solvent. This difference may be attributed to increased solubility of molybdate species in the mixed solvent system. Since lactic acid forms strong complexes with molybdate ions, this fraction of lactate species is missing from the reported yield.

In addition to the main alkyl lactate products quantified in this study, species consistent with retro-aldol reactions on aldohexoses and partially oxidized products were identified in the GC-MS chromatograms of reaction solutions (e.g. ethyl acetals and ethyl esters of glycolaldehyde, glycolic acid, pyruvic acid, 2-hydroxy-3-butenoic acid, and 2,4-dihydroxybutanoic acid). Additionally, catalyst combinations that did not rapidly convert ketoses into lactates and generated Brønsted acidity also resulted in minor formation of 5-

HMF and its partially oxidized variants. The aldohexoses that are required for C_2 and C_4 products are possibly formed in small amounts from ketohexoses by Sn sites on the external surface of Sn-MFI crystallites. The partially oxidized products may be formed by the reduction of Mo(VI) to Mo(V) and/or Mo(IV), since particles of MoO_3 appear to progressively turn dark blue over the course of the reaction. In this regard, 1,2-CS catalysts that do not readily reduce in the presence of carbohydrates have the potential to result in higher ultimate lactate yields. Elimination of aldo-ketohexose interconversion and limitation of oxidation and hexose dehydration reactions, as well as quantification of reaction intermediates and byproducts under these relatively mild retro-aldol conditions and their dependence on 1,2-CS and 1,2-HS site distribution are the focus of further studies within our group.

3.4 Acknowledgments

We thank Dr. Mona Shahgholi (Caltech) for use of GC-MS. This work was financially supported as part of the Catalysis Center for Energy Innovation, an Energy Frontier Research Center funded by the US Department of Energy, Office of Science, Office of Basic Energy Sciences under Award DE-SC0001004. M.O. acknowledges funding from the National Science Foundation Graduate Research Fellowship Program under Grant DGE-1144469.

3.5 References

(1) Werpy, T.; Petersen, G. *Top Value Added Chemicals from Biomass: Volume I -- Results of Screening for Potential Candidates from Sugars and Synthesis Gas*; Pacific Northwest National Laboratory, 2004; Vol. 1.

(2) Dusselier, M.; Van Wouwe, P.; Dewaele, A.; Makshina, E.; Sels, B. F. *Energy Environ. Sci.* **2013**, *6* (5), 1415.

(3) Holm, M. S.; Saravanamurugan, S.; Taarning, E. *Science* **2010**, *328* (5978), 602–605.

(4) Dusselier, M.; Van Wouwe, P.; de Clippel, F.; Dijkmans, J.; Gammon, D. W.; Sels, B. F. *ChemCatChem* **2013**, *5* (2), 569–575.

(5) Huber, G. W.; Iborra, S.; Corma, A. *Chem. Rev.* **2006**, *106* (9), 4044–4098.

(6) Dapsens, P. Y.; Mondelli, C.; Kusema, B. T.; Verel, R.; Pérez-Ramírez, J. *Green Chem.* **2014**, *16* (3), 1176.

(7) Dusselier, M.; Van Wouwe, P.; Dewaele, A.; Jacobs, P. A.; Sels, B. F. *Science* **2015**, *349* (6243), 78–80.

(8) Taarning, E.; Saravanamurugan, S.; Spangsberg Holm, M.; Xiong, J.; West, R. M.; Christensen, C. H. *ChemSusChem* **2009**, *2* (7), 625–627.

(9) Osmundsen, C. M.; Holm, M. S.; Dahl, S.; Taarning, E. *Proc. R. Soc. A* **2012**, *468* (2143), 2000–2016.

(10) Tolborg, S.; Sádaba, I.; Osmundsen, C. M.; Fristrup, P.; Holm, M. S.; Taarning, E. *ChemSusChem* **2015**, *8* (4), 613–617.

(11) Wang, Y.; Deng, W.; Wang, B.; Zhang, Q.; Wan, X.; Tang, Z.; Wang, Y.; Zhu, C.; Cao, Z.; Wang, G.; Wan, H. *Nat. Commun.* **2013**, *4* (Ii), 2141.

(12) Gounder, R.; Davis, M. E. *J. Catal.* **2013**, *308*, 176–188.

(13) Bermejo-Deval, R.; Orazov, M.; Gounder, R.; Hwang, S.-J.; Davis, M. E. *ACS Catal.* **2014**, *4* (7), 2288–2297.

(14) Bilik, V. .; Petruš, L.; Farkas, V. *Chem. Zvesti* **1975**, *29* (5), 690–693.

(15) Tanase, T.; Shimizu, F.; Kuse, M.; Yano, S.; Hidai, M.; Yoshikawa, S. *Inorg. Chem.* **1988**, *27* (23), 4085–4094.

(16) Hricovíniová, Z.; Hricovíni, M.; Petruš, L. *Chem. Pap.* **1998**, *52* (5), 692–698.

(17) Hricovíniová, Z.; Lamba, D.; Hricovíni, M. *Carbohydr. Res.* **2005**, *340* (3), 455–458.

(18) Yanagihara, R.; Osanai, S.; Yoshikawa, S. *Chem. Lett.* **1992**, No. 1, 89–90.

(19) Stanković, E.; Bilik, V.; Fedoroňko, M.; Königstein, J. *Chem. Zvesti* **1975**, *29* (5), 685–689.

(20) Petruš, L.; Petrušová, M.; Hricovíniová, Z. In *Glycoscience: Epimerisation, Isomerisation and Rearrangement Reactions of Carbohydrates*; Stütz, A. E., Ed.; 2001.

(21) Matulova, M.; Bilik, V. . **1990**, *44* (1), 97–103.

(22) Sauvage, J.-P.; Verchère, J.-F.; Chapelle, S. *Carbohydr. Res.* **1996**, *286* (6), 67–76.

(23) Hayes, M. L.; Pennings, N. J.; Serianni, A. S.; Barker, R. *J. Am. Chem. Soc.* **1982**, *104* (24), 6764–6769.

(24) Ju, F.; VanderVelde, D. G.; Nikolla, E. *ACS Catal.* **2014**, *4* (5), 1358–1364.

(25) Stockman, R.; Dekoninck, J.; Sels, B. F.; Jacobs, P. A. In *Current Opinion in Solid State and Materials Science*; Jaroniec, M., Sayari, A., Eds.; Elsevier, 2005; Vol. Volume 156, pp 843–850.

(26) Bílik, V. *Chem. Zvesti* **1972**, *26*, 183–186.

(27) Zhang, J.; Hou, B.; Wang, A.; Li, Z.; Wang, H.; Zhang, T. *AIChE J.* **2014**, *60* (11), 3804–3813.

(28) Pescarmona, P. P.; Janssen, K. P. F.; Delaet, C.; Stroobants, C.; Houthoofd, K.; Philippaerts, A.; De Jonghe, C.; Paul, J. S.; Jacobs, P. A.; Sels, B. F. *Green Chem.* **2010**, *12* (6), 1083.

(29) Mal, N. K.; Ramaswamy, V.; Rajamohanan, P. R.; Ramaswamy, A. V. *Microporous Mater.* **1997**, *12* (4-6), 331–340.

(30) Caldeira, M. M.; Gil, V. M. S. *Polyhedron* **1986**, *5* (1-2), 381–385.

(31) Moliner, M.; Román-Leshkov, Y.; Davis, M. E. *Proc. Natl. Acad. Sci. USA* **2010**, *107* (14), 6164–6168.

(32) Dapsens, P. Y.; Mondelli, C.; Pérez-Ramírez, J. *ChemSusChem* **2013**, *6* (5), 831–839.

(33) Hayashi, Y.; Sasaki, Y. *Chem. Commun. (Camb).* **2005**, No. 21, 2716–2718.

(34) Gunther, W. R.; Wang, Y.; Ji, Y.; Michaelis, V. K.; Hunt, S. T.; Griffin, R. G.; Román-Leshkov, Y. *Nat. Commun.* **2012**, *3*, 1109.

Chapter 4

Catalysis by Framework Zinc in Silica-Based Molecular Sieves

Information contained in Chapter 4 was originally published in: (**Orazov, M.**; Davis, M. E. *Chem. Sci.* **2016**, *7*, 2264–2274. DOI: 10.1039/C5SC03889H)

4.1 Introduction

Heterogeneous catalysts consisting of isolated Lewis acid centers on silica-based supports have been investigated for a wide range of reactions for the conversion of biomass into valorized chemicals. Generation of framework, Lewis acid sites in crystalline, pure-silica molecular sieves by the isomorphic substitution of Si by Sn, Ti, Zr, or Hf is particularly interesting because such sites are located in pores that have diameters comparable to those of substrates, thus giving rise to the possibility of shape-selective catalysis and support-induced stabilization of transition states or intermediates.[1–5] These materials can also exhibit higher acid site stability, with lower tendency for thermal ion migration and sintering into bulk oxides, than analogous sites on amorphous supports. The crystalline materials have been shown to be catalytically active in alkane oxidation, alkene epoxidation, aromatics hydroxylation, Baeyer-Villiger (BV) oxidation, Meerwein-Ponndorf-Verley-Oppenauer (MPVO), sugar isomerization, retro-aldol, and Diels-Alder cycloaddition-dehydration reactions and can, in some instances, be coupled with other catalytic chemistries in “one-pot” strategies.[1,6–15] The catalytic performance of these materials appears to depend strongly on the heteroatom type, the framework in which they are located, and the particular reaction conditions utilized. No single heterogeneous Lewis acid catalyst has been shown to offer optimal performance for the broad range of reactions that are believed to involve Lewis acid activation. Thus, discovery and characterization of catalytically active sites for given reactions are necessary to guide process optimization, and must be performed on an individual basis. Expanding the number of members in this library of zeotypic catalysts is an ongoing effort in the field, with attempts being made to both increase the number of usable zeolitic frameworks, and enable the incorporation of catalytically pertinent metal centers in a controlled manner.

Zinc is a common metal center in a number of homogeneous, Lewis acid catalysts (both in synthetic complexes and naturally occurring enzymes).[16–18] While Zn^{2+} ions exchanged onto aluminosilicate zeolites have been considered for a number of catalytic applications, to the best of our knowledge, evidence of heterogeneous catalysis performed by framework Zn sites in otherwise pure-silica molecular sieves is sparse.[19,20] For instance, Zn^{2+} exchanged onto Al-Beta preferentially titrates paired Al sites, and the resulting material can be used as a catalyst for hydroamination reactions.[19] Such Zn^{2+} sites have been extensively characterized and were demonstrated to have very strong interactions with Lewis basic probe molecules such as acetonitrile and pyridine, with characteristic desorption temperatures considerably higher than those observed in our previous studies of Lewis acidic zeotypes containing Ti, Zr, or Sn.[19,21] However, in all such samples, residual Brønsted acidity, originating from isolated Al sites that are not readily exchanged by Zn^{2+}, is observed.[19] These results, as well as literature on amorphous silica materials bearing isolated Zn sites,[22–24] have prompted us to investigate the properties of CIT-6, an easily-synthesized zincosilicate analog of zeolite beta, whose Lewis and Brønsted acidity have not been sufficiently characterized, despite its first reported synthesis dating back to 1999.[25,26] Instead of direct catalysis by Zn sites, to date, CIT-6 has been mainly used as a support for other metal centers, e.g., Ni^{2+} or Pt^{2+} ions exchanged onto the zincosilicate, or aluminum inserted into the silanol nests of its de-zincated form.[25,27,28] Here, we report our characterization of CIT-6 and other similar zincosilicates by probe-molecule FTIR spectroscopy and evaluate their catalytic properties in the context of Lewis acid mediated reactions, namely: isomerization of glucose to fructose, MPVO reactions of cyclohexanone and 2-butanol, and Diels-Alder cycloaddition-dehydration reactions of partially oxidized variants of 5-hydroxymethylfurfural (5-HMF). We show that such Zn zeotypes have exceedingly strong interactions with Lewis basic substrates. While such high interaction strengths can limit the conditions where catalysis is feasible, under appropriate conditions, these materials may enable chemistries that previously were effectively inaccessible, e.g., Diels-Alder cycloaddition-dehydration reactions of the dimethyl ester of furan-2,5-dicarboxylic acid.

4.2 Experimental

4.2.1 Microporous materials synthesis

The syntheses of microporous and mesoporous materials used in this study are standard and are reported elsewhere, but are briefly outlined below. In each case, as-synthesized solids were recovered by centrifugation, washed thoroughly with distilled water and acetone (Fisher Scientific), dried at 100 °C, and calcined in 100 mL min^{-1} flowing air (Air Liquide, breathing grade) at 580 °C (ramped up at 1 °C min^{-1}) for 6 h.

4.2.1.1 CIT-6 synthesis. CIT-6 was synthesized according to the method reported by Takewaki et al.[25] Colloidal silica (Ludox AS-40), zinc acetate dihydrate (Aldrich), tetraethylammonium hydroxide (Aldrich), and lithium hydroxide monohydrate (Aldrich) were mixed to form a clear synthesis gel of composition 1 SiO_2/0.03 $Zn(OAc)_2$/ 0.65 TEAOH/0.05 LiOH/30 H_2O. The gel was charged into a Teflon-lined, stainless steel autoclave and heated statically at 140 °C for 7.5 days under autogenous pressure. A single large batch (8 g SiO_2 in gel) of the material was synthesized and used throughout the study.

4.2.1.2 VPI-8 synthesis. VPI-8 was synthesized from the same gel as CIT-6, above, but at a higher temperature (150 °C) and longer crystallization times (14 days).

4.2.1.3 Zn-MFI synthesis. Zn-MFI was synthesized according to the method reported by BP.[29] Zinc sulfate heptahydrate (Aldrich) was dissolved in distilled water and the pH was increased to 6 by addition of ammonia solution (Mallinckrodt). The white precipitate that formed (presumably $Zn(OH)_2$) was filtered, washed thoroughly with distilled water, and dried. Sodium hydroxide (Mallinckrodt) and TPAOH (Acros Organics) dissolved in distilled water were added to the precipitate and stirred until the precipitate dissolved. Ludox AS- 40 was added to the solution with stirring. The resulting homogeneous gel of composition 1 SiO_2/ 0.067 ZnO/ 0.105 TPAOH/0.107 Na_2O/14.6 H_2O was charged into a Teflon-lined, stainless steel autoclave and heated in a rotating oven at 175 °C for 4 days under autogenous pressure.

4.2.1.4 Zn-MCM-41 synthesis. Zn-MCM-41 was synthesized according to the method reported by Takewaki et al.[30] Tetraethylorthosilicate (Aldrich), zinc acetate dihydrate, cetyltrimethylammonium bromide (Aldrich), and sodium hydroxide were mixed at ambient temperature for 2h to form a gel of composition 1 SiO_2/0.02 $Zn(OAc)_2$/ 0.61 C_{16}TMABr/0.5 NaOH/4 EtOH/ 30 H2O. The gel was charged into a Teflon-lined, stainless steel autoclave and heated statically at 105 °C for 3 days under autogenous pressure.

4.2.1.5 SSZ-33 synthesis. The borosilicate SSZ-33 was synthesized according to the method reported by Dartt and Davis.[9] Fumed silica (Cab-O-Sil), boric acid (J. T. Baker), N,N,N-trimethyltricyclo[5.2.1.$0^{2,6}$]decaneammoniumhydroxide (R-OH) (provided by Dr. Stacey I. Zones of Chevron Energy Technology Company), and sodium hydroxide were mixed for 1h to form a synthesis gel of composition 1 SiO_2/0.0125 B_2O_3/ 0.2 ROH/0.1 NaOH/40 H_2O. The gel was charged into a Teflon-lined, stainless steel autoclave and heated in a rotating oven at 160 °C for 10 days under autogenous pressure.

4.2.1.6 Zr-Beta synthesis. Zr-Beta were synthesized in fluoride media according to the methods adopted by Pacheco and Davis.[13] Tetraethylorthosilicate was partially hydrolysed in a solution of tetraethylammonium hydroxide for 30 min, followed by the addition of zirconium (IV) propoxide (Aldrich) in ethanol. The alkoxides were allowed to hydrolyse overnight and excess water and alcohols were evaporated. Finally hydrofluoric acid (HF) (Aldrich) was added to form a synthesis gel of composition 1 SiO_2/0.1 ZrO_2/0.54 TEAOH /0.54 HF/6.75 H_2O. Dealuminateed Al-Beta seeds (prepared according to the method reported by Chang et al.)[31] in water were dispersed in the Zr-Beta gel prior to crystallization (at 4 wt% loading of SiO_2). The gels was charged into a Teflon-lined, stainless steel autoclave and heated in a rotating oven at 140 °C for 7 days under autogenous pressure.

4.2.1.7 Generation of silanol nests by heteroatom removal. Zn was inserted into some materials that contained silanol nests generated by removal of Zn or B by treatment of calcined zeolite powders with 1M aqueous H_2SO_4 (Macron) (at 0.1 g solid / 10 mL solution) at ambient temperatures for 12h. The final solids were recovered by centrifugation, thoroughly washed and calcined prior to further use.

4.2.1.8 Post-synthetic Zn insertion. The zinc insertion procedure was adapted from Kozawa.[24] Materials possessing silanols were contacted with an aqueous solution of 0.1 M $ZnCl_2$ (EM Science), and 2.0 M NH_4Cl (Mallinckrodt) (adjusted to desired pH by NH_4OH or HCl), using 1 g solid / 25mL solution. The dispersed solids were stirred in such solutions for 12h at ambient temperature.

Na/Zn/Al-Beta and Zn/Al-Beta were generated by adapting the Zn-exchange procedure of Penzien et al.[19] 0.06 M $Zn(OAc)_2$ aqueous solution was contacted with calcined Na-Al-Beta or H-Al-Beta (Tosoh), at 80 °C, for 24h, using 1g solid/ 25 mL solution.

After the exchange procedures, the solids were recovered by centrifugation, washed twice with distilled water (1 g solid / 25mL water), dried, and calcined, as previously described.

4.2.2. Characterization of solids

Scanning electron microscopy (SEM) with Energy Dispersive X-ray Spectroscopy (EDS) measurements were recorded on a LEO 1550 VP FE SEM at an electron high tension (EHT) of 15 kV. The crystalline structures of zeolite samples were determined from powder X-ray diffraction (XRD) patterns collected using a Rigaku Miniflex II diffractometer and Cu Kα radiation. Thermogravimetric analysis (TGA) under an air atmosphere was performed on a PerkinElmer STA 6000 with a ramp of 10 °C min^{-1} up to 900 °C. Probe molecule IR spectroscopy experiments were performed on a Nicolet Nexus 470 Fourier transform infrared (FTIR) spectrometer with a liquid N_2 cooled Hg−Cd−Te (MCT) detector. Spectra in 4000−650 cm^{-1} range were acquired with 2 cm^{-1} resolution.

Self-supporting wafers (10−20 mg cm^{-2}) were pressed and sealed in a heatable quartz vacuum cell with removable KBr windows. The cell was purged with air (60 mL min^{-1}, Air Liquide, breathing grade) while heating to 500 °C (1 °C min^{-1}), where it was held for 1 h, followed by evacuation at 500 °C for >2 h (<0.01 Pa dynamic vacuum; oil diffusion pump), and cooling to 35 °C under a dynamic vacuum. CD_3CN (Sigma-Aldrich, 99.8% D atoms) or pyridine (EMD Millipore) was degassed by three freeze (liquid N_2), pump, thaw cycles, then dosed to the sample at 35 °C until the Lewis acid sites were saturated, at which point physisorbed and gas-phase species were observed. The cell was evacuated down to 13.3 Pa, and the first spectrum was recorded. Then, the cell was evacuated under a dynamic vacuum at 35 °C for 24h, after which the second spectrum was acquired. Subsequent heating to temperatures specified in plots of spectra was performed at 5 °C min^{-1}, with a subsequent hold time of 0.5 h or greater (as specified in figure legends) prior to acquisition of the next spectrum. The resulting spectra were baseline-corrected by subtracting the spectrum of the pellet at same temperature prior to adsorption of the probe molecule. The spectra are not normalized by the number of Lewis acid sites or framework vibrations. Spectral artifacts known as “interference fringes” were apparent in some spectra and were removed using a computational method based on digital filtering techniques and Fourier analysis.[32]

4.2.3. Catalytic testing

Liquid ^1H and ^{13}C NMR spectra were acquired on a Varian 500 MHz spectrometer equipped with an auto-x pfg broadband probe and a Bruker 400 MHz with Prodigy broadband cryoprobe. Carbohydrate analysis was performed via high performance liquid chromatography on an Agilent 1200 system equipped with refractive index and evaporative light scattering detectors. An Agilent Hi-Plex Ca column at 80 °C was used with ultrapure water as the mobile phase (flow rate of 0.6 mL min^{-1}). Quantitative GC-FID analysis of MPVO and DA cycloaddition dehydration reactions was performed on an Agilent 7890B GC system equipped with a flame ionization detector and an Agilent HP-5 column. Qualitative GC-MS analysis of products was performed on an Agilent 5890 GC system with an Agilent 5970 mass spectrometer and an Agilent DB-5 column.

4.2.3.1. Glucose isomerization reactions. Reactions of glucose (Aldrich) (1 wt% in water or methanol (EMD Millipore) solvent) catalysed by CIT-6 were performed in 10 mL thick-walled crimp-sealed glass reactors (VWR) that were heated in a temperature-controlled oil bath. Reactions were performed at 100 °C, with a 1:50 Zn:glucose initial molar ratio. Aliquots (~100 μL) were extracted at indicated times, mixed with a mannitol solution (external standard), filtered with a 0.2 μm PTFE syringe filter, and analysed by HPLC. To determine the mechanism of fructose formation, glucose ^{13}C-enriched at the C1 position (^{13}C-C1-glucose) (Cambridge Isotope) was reacted with CIT-6 in D_2O at 100 °C for 1h. The product solution was filtered and analysed by liquid NMR directly.

4.2.3.2. MPVO reactions. Reactions of cyclohexanone (Aldrich) and 2-butanol (Fisher Scientific) catalysed by CIT-6 were performed in 10 mL thick-walled crimp-sealed glass reactors (VWR) that were heated in a temperature-controlled oil bath. Reactions were performed at 100 °C, in cyclohexane solvent. The cyclohexanone concentration was fixed at 0.1 M for all reactions, and the initial ratio of Zn:cyclohexanone was 1:100. Naphthalene was used as an internal standard, and reactions were analysed by GC-FID. The turnover frequency at a given 2-butanol concentration was calculated from the initial rate of formation of cyclohexanol.

4.2.3.3. Diels-Alder reactions. The procedure for Diels-Alder reactions was adapted from Pacheco and Davis,[13] but was modified for quantification by GC-FID. Reactions of methyl 5-(methoxymethyl)furan-2-carboxylate (MMFC) (Enamine) or dimethyl 2,5-furandicarboxylate (DMFDC) (Matrix Scientific) with ethylene (Matheson) were carried out in a 50 mL high-pressure stainless steel batch reactor (Parr Series 4590) equipped with a magnetic stirrer (operated at 200 rpm) and heater. For MMFC reactions, 10 mL of a 0.1 M diene solution in heptane (Aldrich) and 100 mg catalyst were loaded into the reactor. DMFDC is poorly soluble in heptane at low temperatures, so this diene, along with 100 mg of catalyst, was loaded directly into the reactor, and 10 mL of heptane was added to give a nominal concentration of 0.33 M of diene. Decane was also added as an internal standard for GC-FID quantification. At the start of a reaction, the head space of the reactor was purged with helium gas with a fill/vent cycle (10 times). Next, the reactor was pressurized to 35 bar with ethylene gas at ambient temperature. The reactor was heated to reaction temperature while the pressure increased autogenously (~60−80 bar). Reaction time was started when the contents of the vessel reached desired temperature, and after a specified time, the reactor was quenched with water and allowed to cool to ambient temperature. At this point, the reactor gases were carefully vented. Solution aliquots that were collected for GC analysis were filtered with a 0.2 μm PTFE syringe filter. The MMFC reaction solutions were analysed directly, while for the DMFDC system, 20 mL of acetone were added to solubilize components not readily soluble in heptane. In both cases, aliquots taken for NMR studies were filtered, rotavaped, and redissolved in acetone-d_6 (Cambridge Isotope). Samples of post-reaction catalysts intended for TGA were isolated from reaction solution by centrifugation, washed twice with either heptane (for MMFC reactions) or acetone (for

DMFDC reactions), and dried at 100 °C overnight. TGA of corresponding washed, unreacted catalysts was used to account for any strongly-retained solvent.

Catalyst recycle experiments were performed for the Diels-Alder cycloaddition-dehydration reaction of DMFDC and ethylene at 210 °C**,** with CIT-6-reZn-pH=6.9. First two reruns were performed with samples that were triply washed with acetone and dried at 100 °C overnight. The third rerun was performed on recalcined catalyst recovered after the second rerun. In all instances reagent and solvent ratios were adjusted to keep constant ratio to inorganic content, as determined by TGA. SEM-EDS analysis of recovered and acetone-washed catalysts was performed. The catalyst used in the third rerun was also analysed by XRD and CD_3CN adsorption tracked by IR.

4.3 Results and discussion

4.3.1 Probe molecule FTIR spectroscopy

The presence and character of Lewis and Brønsted acid sites in solid catalysts may be probed by following the adsorption and desorption behavior of Lewis basic molecules through FTIR spectroscopy. Pyridine and deuterated acetonitrile (CD_3CN) have been routinely used as Lewis bases for this purpose.[33,34] While the significantly different vibrational modes of pyridine coordinated to a Lewis acid center and pyridinium ion generated from protonation of pyridine by a Brønsted acid allow for easy determination of the presence of the two kinds of sites, more subtle differences that differentiate one kind of Lewis acid center from another are harder to discern. Thus, CD_3CN, whose CN stretching frequency tends to increase with the strength of the interaction with a Lewis acid center, can be used as a complimentary probe molecule to qualitatively compare the site of interest with other previously studied sites.[33] Additionally, desorption temperatures of such molecules reflect the strength of interactions a given functional group may be expected to have with the site of interest.

Pyridine adsorption onto CIT-6 (Fig. 4.1) results in IR bands characteristic of pyridine interacting with Lewis acid sites (1451, 1491, and 1610 cm^{-1}) and hydrogen bonded pyridine (ca. 1575 and 1446 cm^{-1}).[23] No band characteristic of Brønsted acid sites (ca. 1550 cm^{-1}) is observed. Pyridine remains adsorbed on the Lewis acid sites up to 300-350 °C. In contrast, pyridine dosed onto bulk ZnO results in bands characteristic of Lewis acid sites (1451 and 1610 cm^{-1}), hydrogen-bonded pyridine (1574 cm^{-1}), and a broad band in the range previously assigned to both dissociatively-adsorbed pyridine on base sites ($C_5H_4N^-$ species) and to protonated pyridine on strong Brønsted acid sites ($C_5H_5NH^+$ species) (Fig. 4.2). Furthermore, all such adsorbed pyridine desorbs upon evacuation at 300 °C (Fig. 4.2).

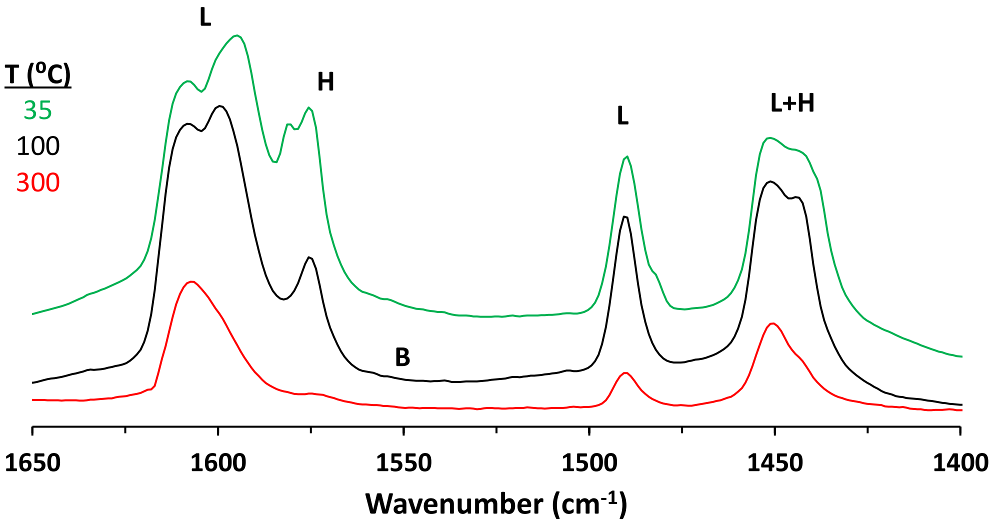

Figure 4.1 Baseline corrected IR spectra of pyridine adsorbed on CIT-6 at 35 °C. Different colors (indicated in legend) correspond to different subsequent desorption temperatures carried out for 1h. Peaks corresponding to pyridine coordinated to Lewis acid (L), Brønsted acid (B), and hydrogen-bonding (H) sites are marked.

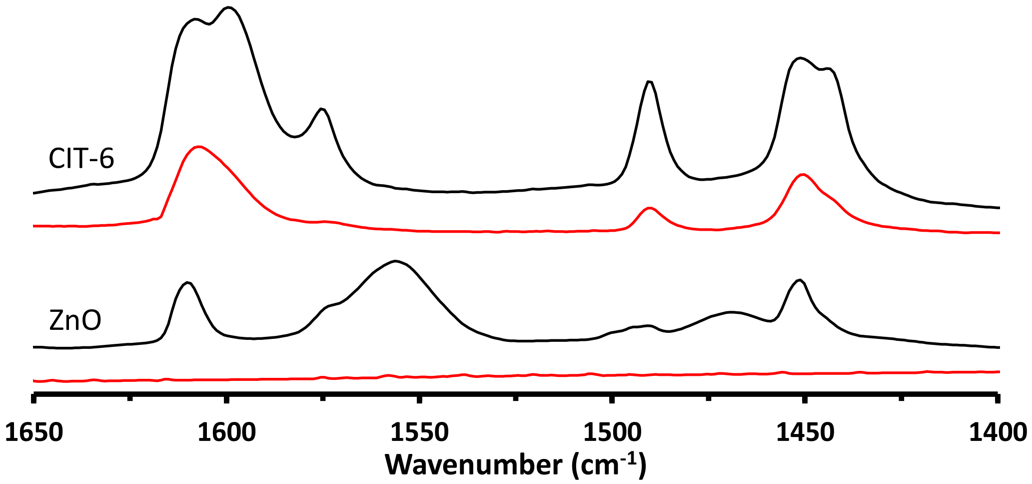

Figure 4.2 Baseline-corrected IR spectra of pyridine adsorbed on CIT-6 (top) and ZnO (bottom) at 35 °C. Black and red spectra correspond to subsequent desorption under dynamic vacuum for 1h at 100 °C and 300 °C, respectively.

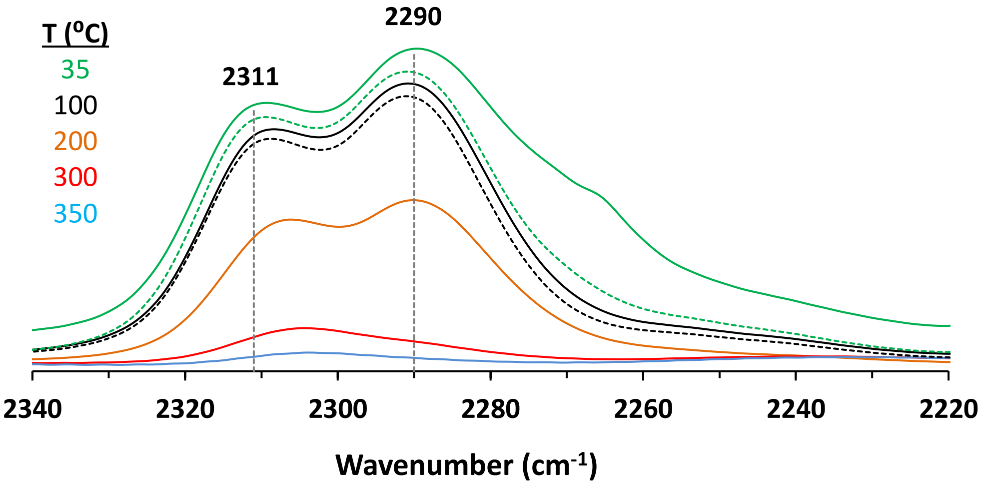

Figure 4.3 Baseline corrected IR spectra of CD_3CN adsorbed on CIT-6 at 35 °C (green solid) and desorbed at different times and temperatures: 24h at 35 °C (green, dashed), 0.5h at 100 °C (black, solid), 1.5h at 100 °C (black, dashed), 0.5h at 200 °C (orange, solid), 0.5h at 300 °C (red, solid), and 0.5h at 350 °C (blue, solid).

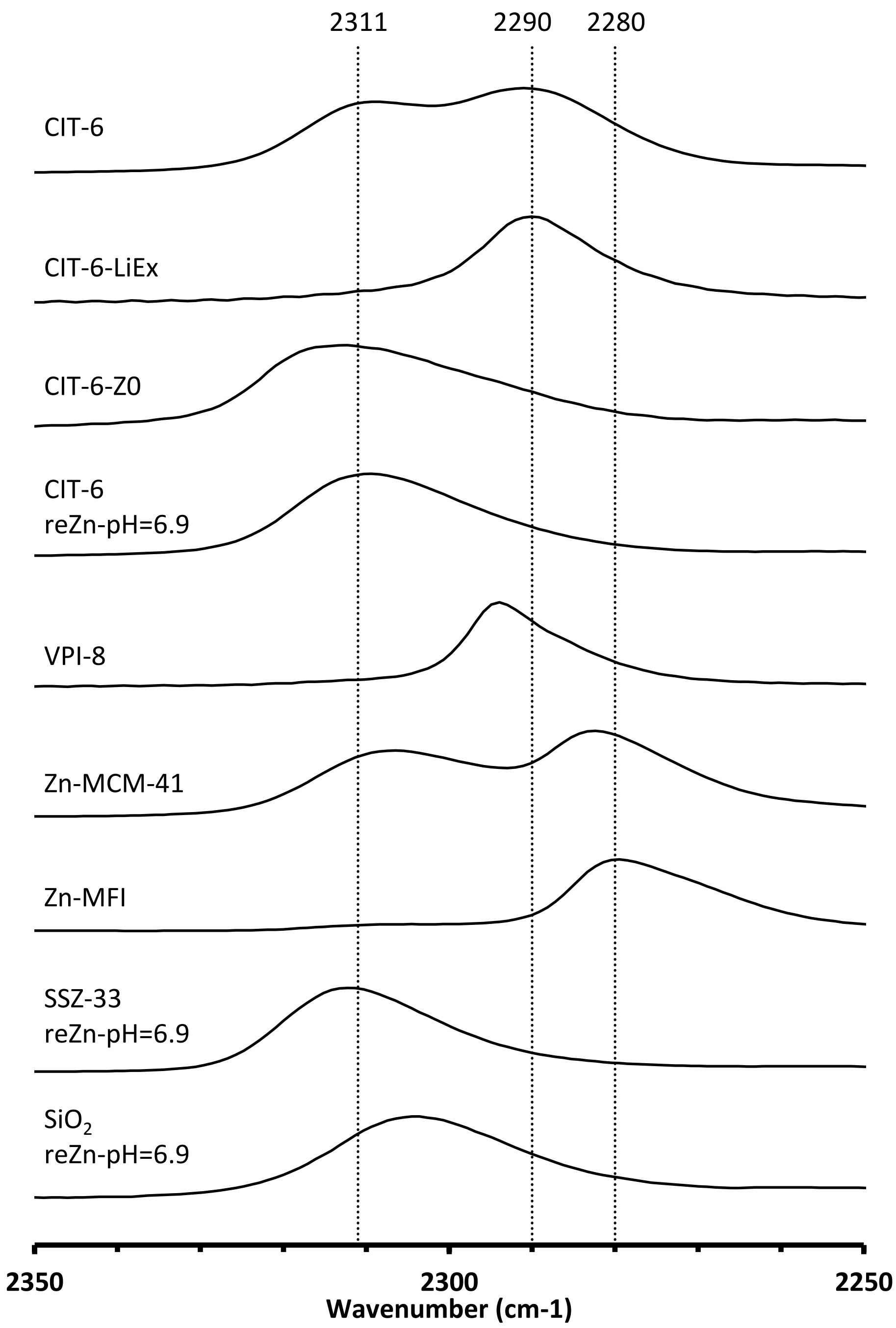

Figure 4.4 Baseline-corrected, normalized IR spectra of CD_3CN adsorbed at 35 °C on (from top to bottom): CIT-6, CIT-6-LiEx, CIT6-Z0, CIT-6-reZn-pH=6.9, VPI-8, Zn-MCM-41, Zn-MFI, SSZ-33-reZn-pH=6.9, and SiO_2-reZn-pH=6.9. Spectra were collected after desorption at 100 °C for 1h.

Adsorption of CD_3CN reveals the presence of at least two Lewis acid sites in CIT-6 (Fig. 4.3), with deconvoluted bands appearing at 2311 cm^{-1} and 2290 cm^{-1}. The frequency of the 2311 cm^{-1} band of CIT-6 suggests an extent of polarization comparable to that generated by Sn-MCM-41, Sn-MFI, and Zr-Beta (ca. 2309-2312 cm^{-1}), but lower than that generated by the "open" Sn site of Sn-Beta (2315 cm^{-1}) or Al Lewis acid sites in various zeolites ($\geq$ 2320 cm^{-1}).[33,35,36] This band is intermediate between the 2314 cm^{-1} band reported for the Zn-exchanged Al-Beta[19] and the 2305 cm^{-1} band measured for Zn sites dispersed on amorphous silica (Fig. 4.4). The lower frequency of the band measured for the amorphous-supported Zn sites is consistent with the trend observed for Sn in Sn-Beta and Sn-MCM-41.[36,37] Silica-supported Zn sites have been previously characterized in the context of alkane dehydrogenation. EXAFS data suggest that the dehydrated Zn sites in this type of material datively coordinate an oxygen of a neighboring silanol (as shown in structure Z_0 in Figure 4.5),[22] but this polarization appears insufficient to generate a strong Brønsted acid site that is capable of protonating pyridine.

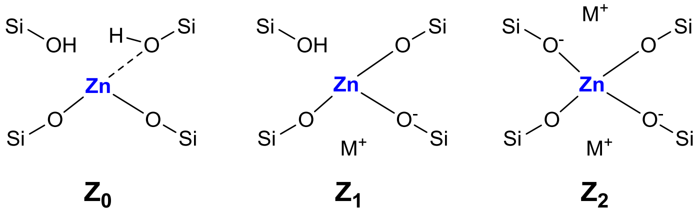

Figure 4.5 Proposed framework Zn site structures in microporous zincosilicates. M^+ is a monovalent cation, such as alkali or alkyl ammonium.

The 2290 cm^{-1} band of CD_3CN adsorbed on CIT-6 is likely associated with Li-bearing Zn sites. We previously observed a CD_3CN band ca. 2292 cm^{-1} in a Sn-Beta material that was exchanged with Li^+ under basic conditions in order to cationate the neighboring silanol of the "open" Sn site.[21] Similarly, Na^+ and K^+ exchanges generate sites with characteristic CD_3CN bands ca. 2280 and 2273 cm^{-1}, respectively. VPI-8 (VET framework) is a zincosilicate with a higher framework density than CIT-6 that can be found as a minor phase impurity in CIT-6 powders and is difficult to detect at low concentrations (as demonstrated by the data shown in Fig. 4.6). VPI-8 crystallizes if the CIT-6 gel (which contains Li^+ ions) is aged beyond complete CIT-6 crystallization[38] and exhibits a CD_3CN band primarily ca. 2294 cm^{-1}. On the other hand, Zn-MCM-41 and Zn-MFI are synthesized from gels containing Na^+ ions and CD_3CN bands ca. 2280 cm^{-1} are observed for these materials. These data are consistent with the presence of Zn sites possessing structures Z_1 and/or Z_2 in Fig. 4.5. Further support for this tentative assignment comes from ion exchange experiments that shift the site distribution in CIT-6. A moderately basic Li^+ exchange (1M $LiNO_3$, and initial pH = 10, set by LiOH) generates a material (CIT-6-LiEx) possessing primarily a 2290 cm^{-1} CD_3CN band. On the other hand, exchanging CIT-6 with a nearly-neutral 1M solution of $N(CH_3)_4Cl$, followed by calcination, produces a material (CIT-6-Z0) possessing primarily a 2312 cm^{-1} CD_3CN band, with a broad red-shifted shoulder. It is important to note that, within the measurement error of energy dispersive spectroscopy (EDS), CIT-6-LiEx (Si/Zn = 10.9 ± 2.1) has the same Zn content as the parent material (Si/Zn = 12.2 ± 0.9), but CIT-6-Z0 loses nearly half of its Zn (Si/Zn = 21.3 ± 4.2).

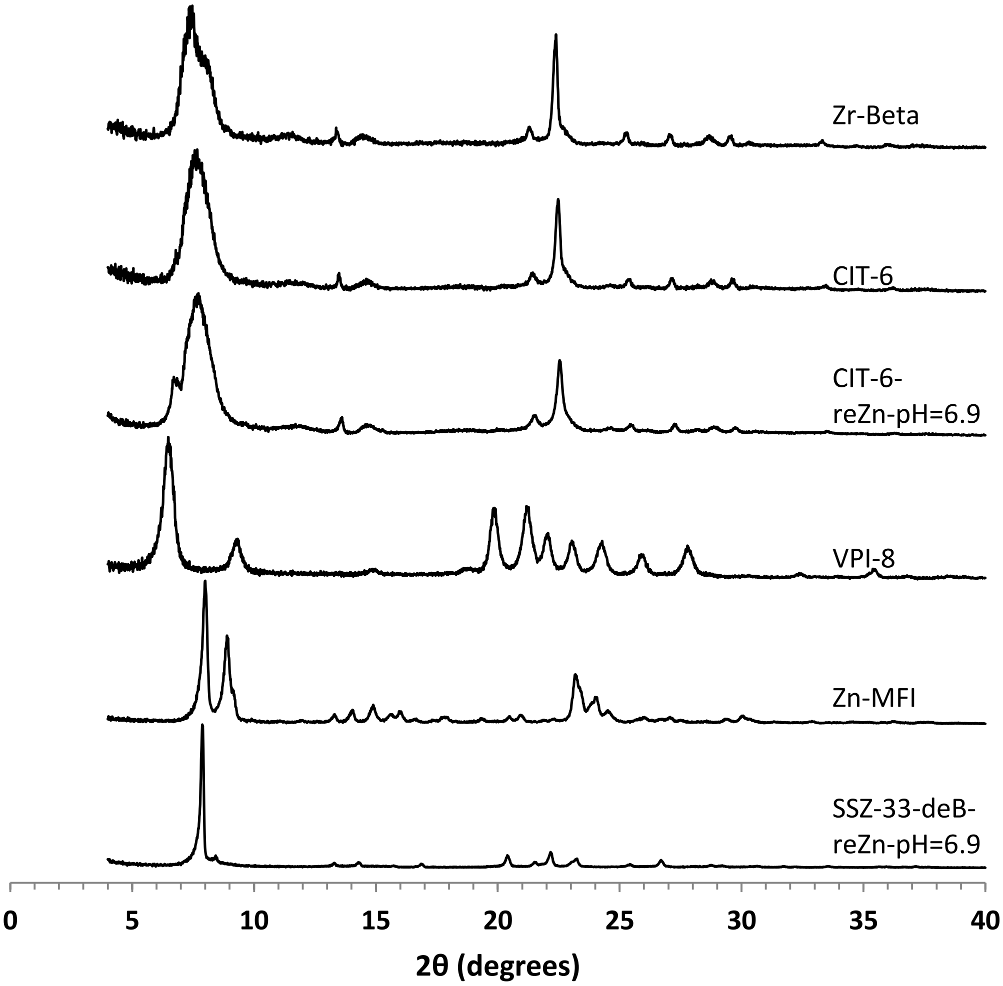

Figure 4.6 Normalized powder XRD data for selected microporous materials (from top to bottom): Zr-Beta, CIT-6, CIT-6-reZn-pH=6.9, VPI-8, Zn-MFI, and SSZ-33-reZn-pH=6.9. All materials have been calcined. XRD pattern of the parent CIT-6 sample does not have noticeable VPI-8 peaks, but, upon 1M H_2SO_4 treatment, Zn-reinsertion, and calcination, a shoulder in the low angle peak of *BEA becomes apparent, indicating the presence of VPI-8 (VET framework) as a minor phase impurity. Crystal aggregates of VPI-8 morphology are also observed among *BEA crystals. The increase in the prominence of the VET peak in the powder pattern may be associated with selective partial degradation of the *BEA framework in the treatment of the sample, as it is a less dense structure.

Materials with higher total Zn contents, with CD_3CN bands ca. 2312-2310 cm^{-1}, can be generated by an alternative post-synthetic strategy (*vide infra*). IR spectra of CD_3CN adsorbed on VPI-8, Zn-MCM-41, Zn-MFI, and a number of post-synthetically Zn-modified materials are shown in Fig. 4.4. (powder XRD data of these microporous materials are included in Fig. 4.6).

In our hands, CD_3CN appears to interact much stronger with the two discernable Lewis acid sites in calcined CIT-6, than with any of the sites in Sn-, Ti-, or Zr-Beta, or their alkali-exchanged counterparts. In fact, the persistence of coordinated CD_3CN on the CIT-6 sites to temperatures beyond 200 °C under vacuum (Fig. 4.3) is consistent with the high temperatures of TPD desorption peaks for Zn-exchanged Al-Beta.[19] The high interaction strength of CD_3CN with such sites (as inferred from high desorption temperatures) appears to conflict with the relatively low induced blue shifts of the CN vibration. This disparity may stem from the difference in the energies of structural rearrangements for Zn sites vs Sn, Ti, or Zr sites upon desorption of probe molecules.

CD_3CN adsorbed on bulk ZnO generates spectroscopic signatures distinct from CIT-6 (Fig. 4.7), with a broad band ca. 2300 cm^{-1} that can be attributed to Lewis or Brønsted acid sites, as well as a multitude of bands below 2200 cm^{-1}, characteristic of CD_2CN^- and polyanions formed by deprotonation of CD_3CN by strongly basic surface oxygen species.[34] While the 2300 cm^{-1} band is not spectroscopically resolved from the bands observed in CIT-6, the lack of CD_2CN^- signatures in the CIT-6 spectra suggests an absence of detectable amounts of extra-framework ZnO in CIT-6 after calcination.

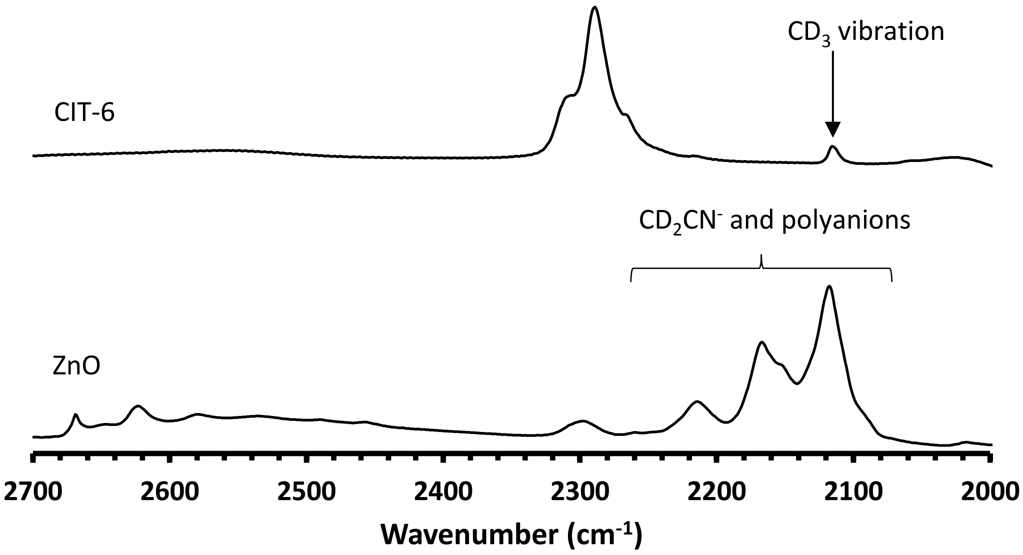

Figure 4.7 Baseline-corrected, normalized IR spectra of CD_3CN adsorbed at 35 °C on CIT-6 (top) and ZnO (bottom). A CD_3 vibration band ca. 2115 cm^{-1} is found in all spectra of CD_3CN adsorbed on SiO_2 materials, and is not a shifted

---

4.3.2 Catalysis with microporous zincosilicates

We have previously explored reactions of sugars catalyzed by isolated Sn sites in SiO_2-based materials and by SnO_x particles located in the pores of Si-Beta.[39] The isolated "open" Sn sites that have an adjacent protonated silanol were found to promote glucose-fructose isomerization through a 1,2-intramolecular hydride shift mechanism, while SnO_x particles behaved as base catalysts by promoting the same isomerization through an enolate mechanism that involves deprotonation of α-carbonyl carbon (Fig. 4.8).[21,39] Data provided in Fig. 4.9 show that under the same reaction conditions as we used previously, CIT-6 isomerizes glucose to fructose in both water and methanol solvents, but does so with proton abstraction from the α-carbonyl carbon (as evidenced by ^{13}C NMR of isotopically labeled glucose; Fig. 4.10). While the reaction appears to proceed catalytically (TOF > 1 in water and methanol), the reaction slows prior to reaching an equilibrium distribution of sugars, suggesting that catalyst deactivation occurs (Fig. 4.11).

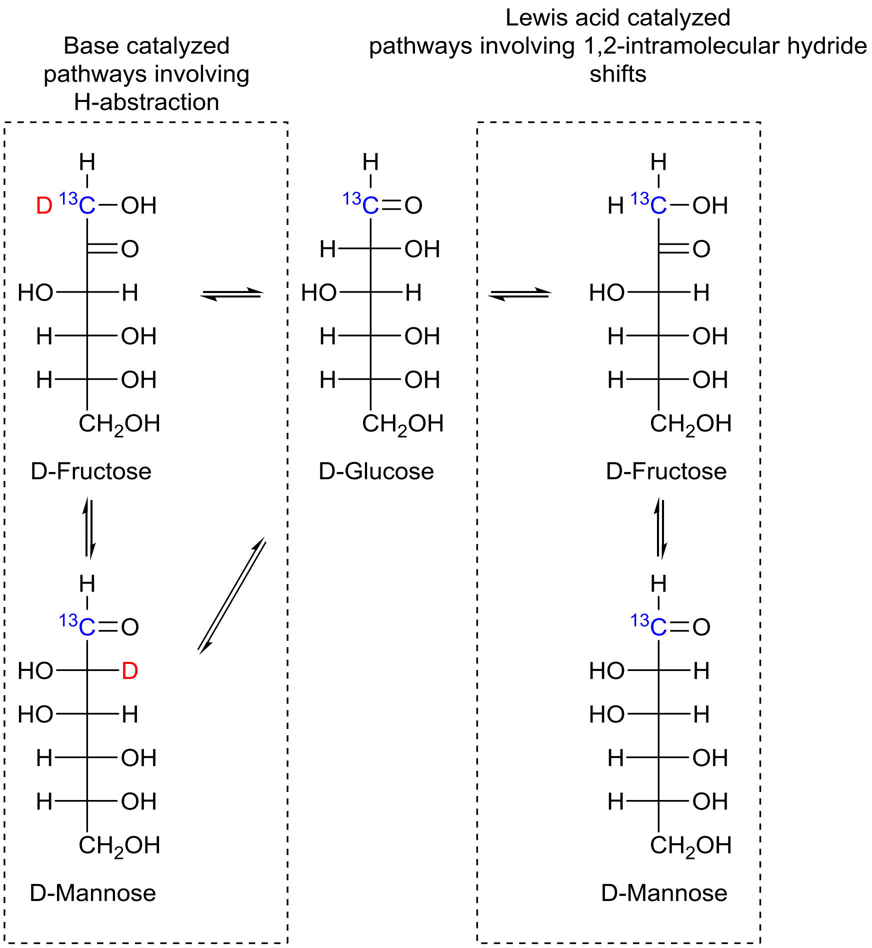

Figure 4.8 Illustration of glucose isomerization mechanisms promoted by bases and Lewis acids. For reactions performed in deuterated solvents (D_2O or MeOD), deuterium incorporation is expected for products formed through enolate intermediates, but not through intramolecular hydride shifts. The use of ^{13}C-C1-glucose enables product analysis without the need for fractionation.

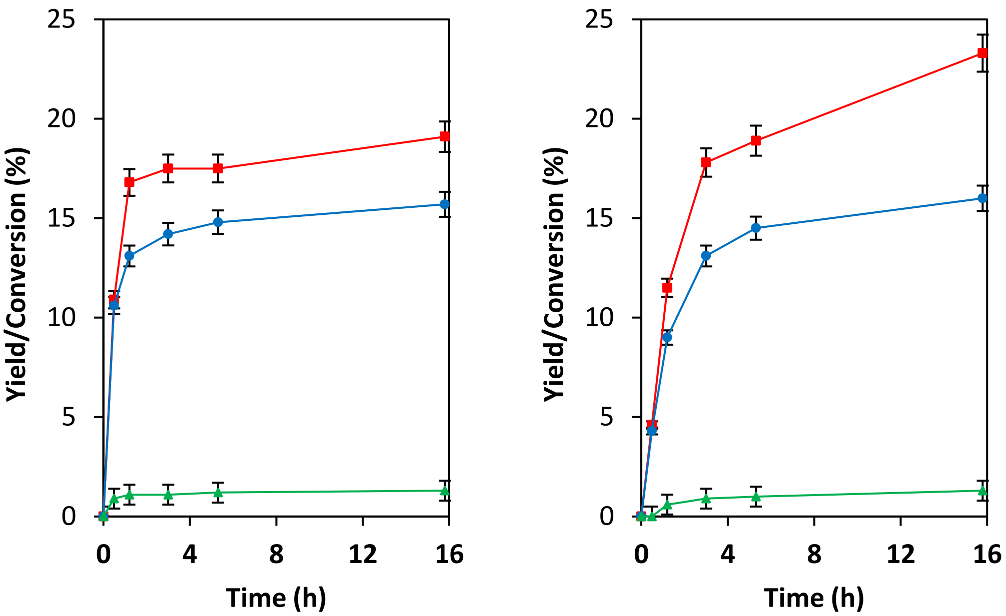

Figure 4.9 Glucose isomerization reactions are catalyzed by CIT-6 in aqueous (left) and methanolic (right) solvents. Glucose conversion (red squares), fructose yields (blue circles), and mannose yields (green triangles) are plotted as a function of reaction time. Reaction conditions: 100 °C, 1% (wt/wt) glucose, 1:50 Zn:glucose initial molar ratio.

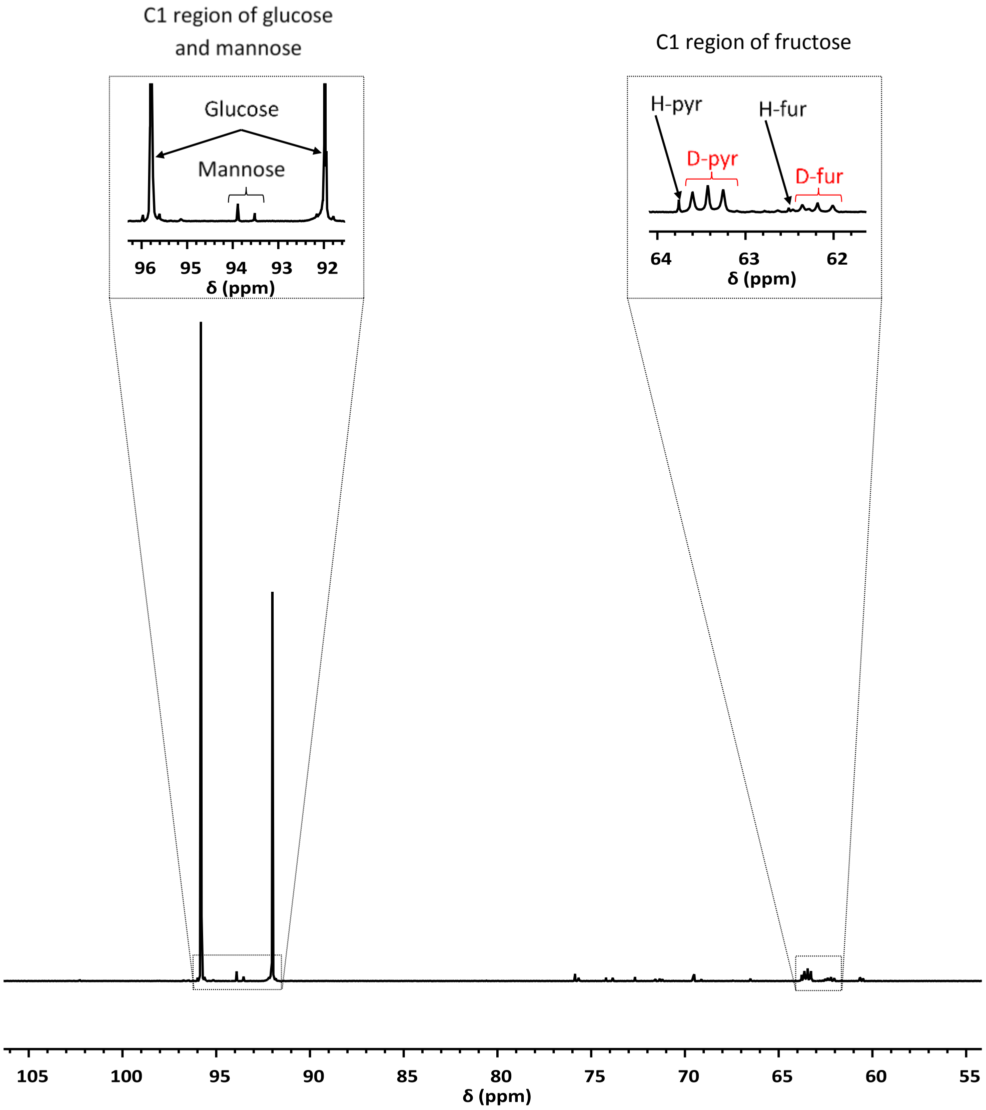

Figure 4.10 ^{13}C NMR spectrum of unseparated reactant (^{13}C-C1-glucose) and the products generated by CIT-6 at 100 °C after a 1h reaction in D_2O. The abbreviations “pyr” and “fur” stand for pyranose and furanose, respectively. Incorporation of deuterium at C1 position of fructose, as evidence by appearance of low-intensity triplets, indicates a base-catalyzed mechanism. The presence of ^{1}H-form of fructose likely originates from the small fraction of ^{1}H impurity in D_2O solvent, but could also arise from a small contribution from a hydride shift mechanism. Unlabeled peaks correspond to natural abundance ^{13}C (~1%) occurring in glucose C2-C6 positions.

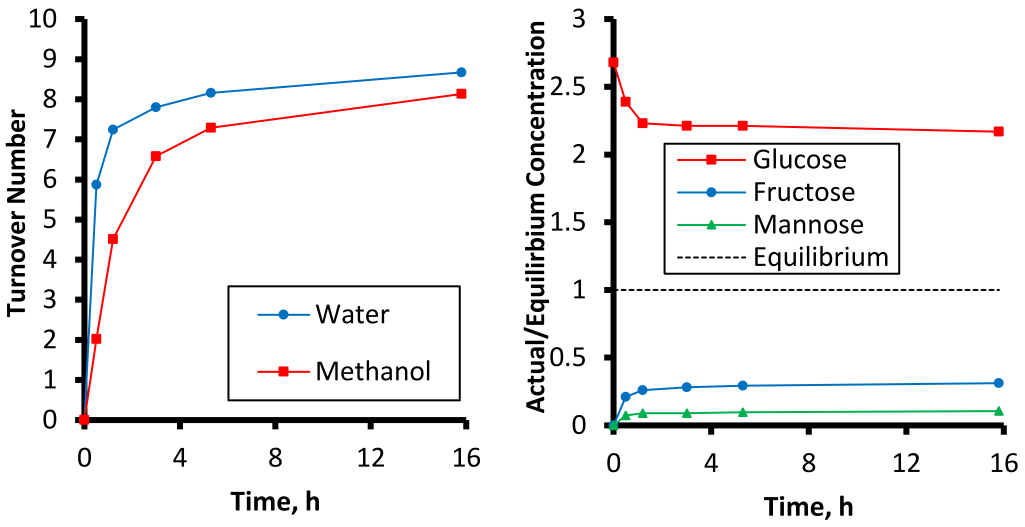

Figure 4.11 Left: Stagnation of TON for glucose reactions catalyzed by CIT-6 in water and methanol solvents, based on total Zn content. Right: Approach to equilibrium distribution of sugars in water. Reaction conditions: 100 °C, 1% (wt/wt) glucose, 1:50 Zn:glucose initial molar ratio.

EDS analysis indicates a 35% decrease in Zn content of the CIT-6 sample after reaction in water. Recalcination of the catalyst recovered and washed after such a reaction does not result in the recovery of isomerization activity. Additionally, CD_3CN adsorption on this material reveals a loss of the 2290 cm^{-1} band that is present in the original CIT-6 sample, but retention of the 2311 cm^{-1} band (Fig. 4.12). Though ZnO and $Zn(OH)_2$ can catalyze the isomerization glucose through the enolate pathway, it is unlikely that the isomerization activity observed in the original CIT-6 is attributable to such species, as their presence is not observed in spectroscopic characterization, and the permanent catalyst deactivation is inconsistent with their presence. The catalytic data obtained from CIT-6 are more consistent with involvement of Z_1 or Z_2 sites that we hypothesize are correlated to the 2290 cm^{-1} CD_3CN band. The enhanced basicity of framework oxygens whose charge is balanced by alkali cations may allow for participation of Z_1 or Z_2 sites in this base-promoted reaction.

The generation of small quantities of α-hydroxycarboxylic acid species (e.g., lactic acid), as ascertained by ^{1}H and ^{13}C NMR, suggests acid-catalyzed hydrolysis of Z_1 and Z_2 sites as the possible mode of deactivation.

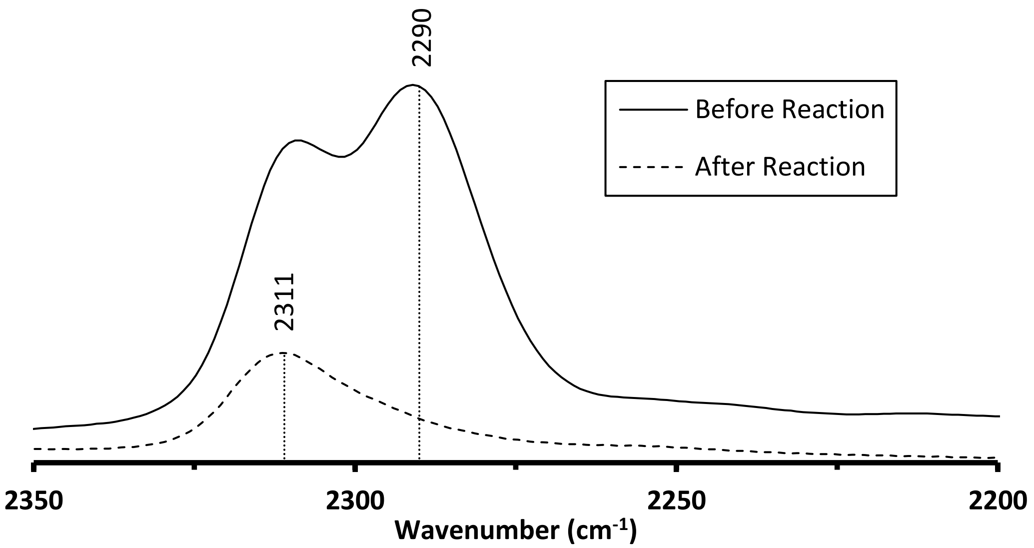

Figure 4.12 Baseline-corrected IR spectra of CD_3CN adsorbed at 35 °C on CIT-6 before and after glucose reaction in water. Spectra were collected after desorption at 100 °C for 1h. Spectra are not quantitative and total Zn content (based on EDS measurements) falls by 35% after reaction.

While CIT-6 is an active catalyst for glucose-fructose isomerization, this reaction is not proceeding via catalysis by the Lewis acid sites (as would be suggested by Lewis base adsorption in FTIR experiments). The pK_a values of the conjugate acids of nitriles are higher than those of the conjugate acids of aldehydes, ketones, alcohols, and water. Outside of solvation effects, this relative ranking implies that nitriles should have weaker interactions with Lewis acid sites than the other Lewis basic species listed above. Data provide in Fig. 4.3 show that vacuum desorption of CD_3CN from CIT-6 Lewis acid sites at 100 °C is slow, with minimal desorption occurring over the course of an hour. Desorption of water, methanol, and cyclohexanone were also observed to be slow at 100 °C, and appreciable desorption rates only occurred at temperatures higher than 200 °C. These low rates of desorption of probe molecules are expected to translate to slow desorption of these types of compounds present in solutions at reaction conditions. Thus, the Lewis acid-mediated catalytic properties of Zn sites in CIT-6 at low temperatures are mitigated in solvents possessing strongly Lewis basic functional groups. This interpretation is supported by the observed rate behavior of Lewis-acid mediated MPVO reactions of cyclohexanone and 2-butanol catalyzed by CIT-6. Data in Fig. 4.13 show the measured initial rates for this reaction as a function of 2-butanol concentration, for a fixed concentration of cyclohexanone (0.2 M). The initial rate of the reaction increases with increasing 2-butanol concentration, but peaks at a concentration where the ratio of the two reactants is stoichiometric (0.2 M), and decreases with further increase in 2-butanol concentration. This reaction behavior is consistent with kinetically limiting desorption rates. The nominal TOF of CIT-6 for this reaction (based on total Zn) is 3-4 orders of magnitude lower than that of Sn-Beta (based on total Sn) under similar reaction conditions.[3] At this point, it is not clear if the low TOF reflects the intrinsic catalytic activity of the Zn sites and their hindered desorption rates, or if severe diffusion limitations induced by high concentrations of strongly bound species also contribute to the slow measured kinetics.

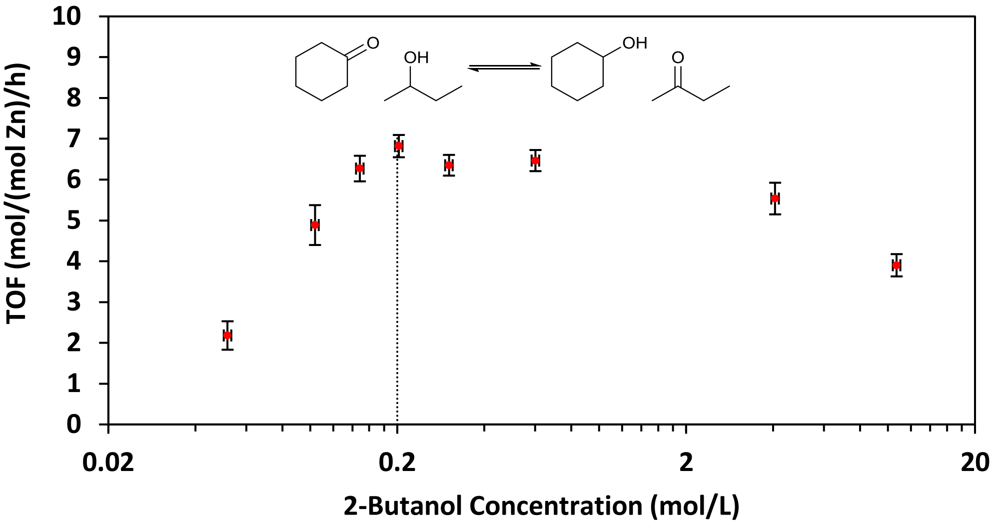

Figure 4.13 Initial TOF of MPVO reactions of cyclohexanone and 2-butanol catalyzed by CIT-6 as a function of 2-butanol concentration. Reaction conditions: 100 °C, 0.2 M cyclohexanone, indicated concentration of 2-Butanol in cyclohexane, and 1:100 Zn:cyclohexanone initial molar ratio.

Sabatier's principle can be used to qualitatively rationalize the poor catalytic performance observed for MPVO reactions promoted by CIT-6 relative to the performance of other Lewis acidic beta zeotypes known to catalyze such reactions,[2,40] and to infer reaction conditions where CIT-6 may behave as a catalytically interesting material. The principle states that for a reaction with a given activation energy, an optimal enthalpy of desorption of the substrate from the heterogeneous catalyst exists. For MPVO reactions, Ti-Beta appears to interact too weakly and CIT-6 too strongly with the carbonyl bearing substrates (as inferred from desorption of cyclohexanone), with both cases resulting in low reaction rates. Sn-Beta and Zr-Beta have desorption rates intermediate to the two extremes and result in significantly higher reaction rates at a given temperature. Because these materials usually possess more than one kind of coordination environment for the heteroatoms, quantitative statements of these results is presently not possible due to a lack of measurements of site-specific reaction rates and adsorption enthalpies. Another outcome of Sabatier's principle suggests that reactions with higher intrinsic activation barriers will generally correspond to higher optimal adsorption enthalpies. Thus, the Lewis acid sites of CIT-6 have the potential to catalyze high-temperature reactions more optimally than the Lewis acid sites in weaker binding materials such as in Ti-, Zr-, and Sn-Beta.

The Diels-Alder (DA) cycloaddition-dehydration reactions of substituted furans with ethylene are a promising route to terephthalic acid made from renewable sources (Fig. 4.14). Such reactions of dimethylfuran ($R_1 = R_2 = CH_3$ in Fig. 4.14) can be catalyzed more efficiently by Brønsted acids than Lewis acids,[41,42] but furans with oxygenated side-groups that can be derived from 5-hydroxymethylfurfural without costly reduction steps react on Brønsted acidic zeolites with negligible selectivities towards desired DA products under similar or milder conditions.[13] Only the Lewis-acidic Sn- and Zr-Beta were previously observed to catalyze the DA reactions of such substrates with appreciable selectivity, with Zr-Beta resulting in considerably higher selectivities, for reasons currently not understood.[13] The apparent absence of strong Brønsted acid sites in CIT-6 makes it a candidate catalyst for these kinds of DA reactions.

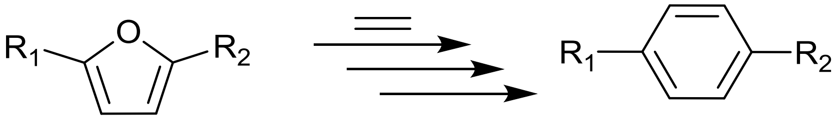

Figure 4.14 Generalized description of Diels-Alder cycloaddition-dehydration reactions of substituted furans (R_1, R_2 = CH_3, CH_2OR, CHO, or CHOOR, where R = H or alkyl group). This is a multistep process, whose rate limiting steps are greatly influenced by the identity of the R_1 and R_2 groups.

In heptane solvent, CIT-6 catalyzes the formation of methyl 4-(methoxymethyl) benzenecarboxylate (MMBC) in the reaction of methyl 5-(methoxymethyl)furan-2-carboxylate (MMFC) with ethylene at 190 °C, with a yield of 16% at 51% selectivity (Fig. 4.15). No significant quantities of soluble byproducts were detected by ^{1}H NMR (Fig. 4.16) or observed in the GC chromatograms. Interestingly, no conversion is observed in dioxane, the solvent found to give the best selectivity for this reaction when Zr-Beta or Sn-Beta catalysts are used.[13] This result is consistent with the hypothesis that, in CIT-6, there is Lewis acid site passivation through competitive binding of oxygenated species, even at these relatively high temperatures. Furthermore, Brønsted acid sites are expected to not be passivated in dioxane, and the lack of MMFC conversion in this solvent suggests that no catalytically relevant Brønsted acid sites are accessible at the reaction temperatures. Additionally, bulk ZnO produces no detectable conversion of MMFC in heptane, demonstrating that it is the framework Zn in CIT-6 that is catalytically active in this reaction. CIT-6-LiEx is significantly less active than the parent CIT-6, suggesting that the CIT-6 sites associated with 2290 cm^{-1} CD_3CN IR band are unable to effectively catalyze these reactions. CIT-6-Z0 primarily has sites associated with the 2311 cm^{-1} CD_3CN IR band and, despite its lower Zn content, results in higher MMBC yields than the parent CIT-6 material. These data implicate the Z_0 sites as the catalytically active species in such DA cycloaddition-dehydration reactions. However, site cooperativity in mixed-site samples of CIT-6 is another possibility that warrants consideration in future studies. Because determination of cooperativity would require quantitation of each type of site, determination of their proximity, and measurement of intrinsic site kinetics, such efforts are outside of the scope of this work.

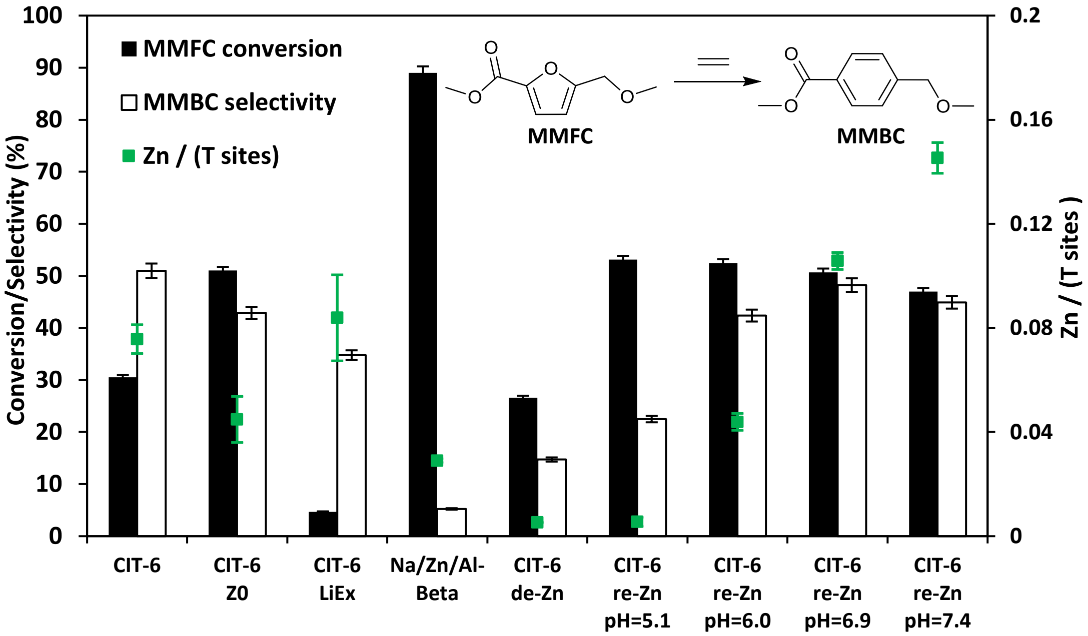

Figure 4.15 Diels-Alder cycloaddition-dehydration reactions of MMFC with ethylene catalyzed by CIT-6 and its various modified forms with different Zn contents and site distributions.

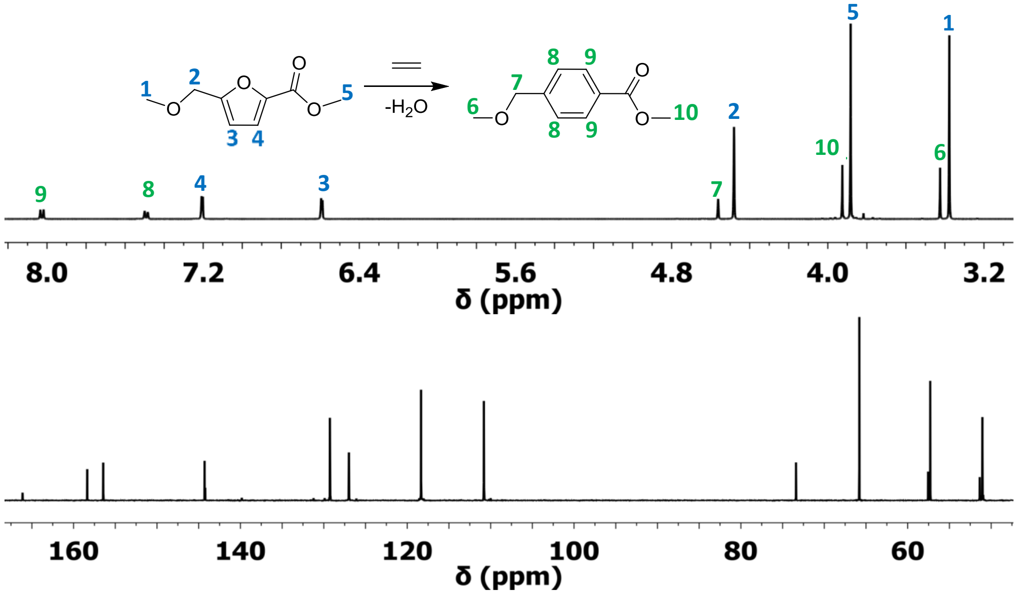

Figure 4.16 ^{1}H (top) and ^{13}C (bottom) NMR spectra of unseparated reactant (MMFC) and the products generated by CIT-6 at 190 °C after a 6h DA cycloaddition-dehydration reaction in heptane.

While other porous zincosilicate materials (Zn-MCM-41, Zn-MFI, VPI-8, and deboronated SSZ-33 that has been post-synthetically zincated) have varying distributions of Zn Lewis acid sites (i.e., different proportions of Z_0, Z_1, and Z_2 type of sites as characterized by CD_3CN IR experiments (Fig. 4.4)), all of these materials produce negligible levels of MMBC and result in minor conversion of MMFC and appear brown in color after reaction (Table 4.1). The reason for the lack of activity of Zn sites in these materials remains unknown. However, the 10MR pores in Zn-MFI may be too small. VPI-8 (VET structure) has a 1-D linear 12MR pore system and SSZ-33 (CON structure) has 12MR pores intersected by 10MR pores, so both materials should be able to accommodate molecules that can enter the *BEA framework, but the additional limitation of 1-D diffusion may render these materials effectively inactive. The lack of activity of the un-constrained sites in Zn-MCM-41 or Zn on amorphous silica are hard to reconcile, but these results are consistent with the reported lack of activity of Sn- and Zr-MCM-41,[13] and suggest that the *BEA framework may play a role in the stabilization of intermediates or transition states for such DA reactions. We also note that Na-Al-Beta that has been ion exchanged with Zn^{2+} leads to negligible selectivity towards MMBC, and apparent coking of catalyst.

Assuming homogeneous dispersion of Zn in CIT-6, the relatively low Si/Zn ratio of the material (12.2 ± 0.9) implies that 4.8 Zn sites are found per unit cell. Considering that each MMFC molecule possesses 4 oxygen atoms, and spans a large fraction of the void space of a *BEA unit cell, coordination to multiple Zn sites is possible at high Zn loadings. Multiple coordination points with the framework are expected to further increase the molar

Table 4.1 Summary of results for DA cycloaddition-dehydration reaction of MMFC and ethylene.

Run	Catalyst	Si/M ratio	T (°C)	Time (h)	X_{MMFC} (%)	Y_{MMBC} (%)	S_{MMBC} (%)
1	CIT-6	12.2 ± 0.9	150	12	18.1	10.1	55.7
2	CIT-6	12.2 ± 0.9	170	12	34.5	21.5	62.3
3	CIT-6	12.2 ± 0.9	170	18	45.8	28.4	62.0
4	CIT-6	12.2 ± 0.9	190	6	30.5	15.6	51.0
5	Catalyst recovered after **run 4** [1]	n.d.	190	6	18.8	10.2	54.4
6	CIT-6	12.2 ± 0.9	190	12	43.6	25.7	58.8
7	CIT-6	12.2 ± 0.9	230	6	41.6	9.9	23.8
8	CIT-6 [2]	12.2 ± 0.9	190	6	*	*	*
9	Bulk ZnO	-	190	6	*	*	*
10	CIT-6-LiEx	10.9 ± 2.5	190	6	4.7	1.6	34.8
11	CIT-6-Z0	21.3 ± 4.2	190	6	51.0	21.9	42.9
12	Zn MCM-41	21.6 ± 8.0	190	6	4.3	*	*
13	Zn MFI	38.8 ± 3.2	190	12	6.8	*	*
14	VPI-8	18.3 ± 1.8	190	6	5.1	*	*
15	SSZ-33-deB-re-Zn-pH=6.9	12.6 ± 0.9	190	12	10.6	0.4	4.1
16	Zn-Na-Al-Beta	31.0 ± 0.7 Si/Zn 12.6 ± 0.1 Si/Al	190	6	89	4.7	5.2
17	CIT-6-de-Zn	188 ± 17	190	6	26.6	3.9	14.7
18	CIT-6-re-Zn-pH=5.1	180 ± 57	190	6	53.1	11.9	22.5
19	CIT-6-re-Zn-pH=6.0	21.8 ± 1.6	190	6	52.5	22.2	42.4
20	CIT-6-re-Zn-pH=6.9	8.5 ± 0.3	190	6	50.7	24.5	48.2
21	CIT-6-re-Zn-pH=7.4	5.9 ± 0.2	190	6	47.0	21.2	44.9
22	Zr-Beta	79 ± 9	190	6	44.7	18.9	42.3

Reaction conditions: catalyst, temperature, and duration as indicated; 0.1 M MMFC in 10 mL heptane; 100 mg of catalyst; and 35 bar C_2H_4 at 25 °C.

[1] Catalyst washed with heptane, and reused without recalcination

[2] Dioxane solvent (0.1 M MMFC in 10 mL)

* Below detection limit for conversion or yield (0.4%)

n.d. not determined

enthalpy of desorption for reactants, intermediates, and products. The close spacing of Zn sites also increases the likelihood of coupling reactions, as adsorbates may be positioned in intimate contact for extended periods of time. We investigated the possibility of increasing catalyst selectivity by adapting a procedure used to ion-exchange Zn amines onto amorphous silica supports in order to generate dispersed Zn sites primarily in Z_0 configuration, as characterized by CD_3CN IR experiments (Fig. 4.4).[24] Briefly, this procedure involves contacting a material possessing silanol nests with an aqueous solution containing 0.1 M $ZnCl_2$, and 2.0 M NH_4Cl, adjusted to desired pH by NH_4OH or HCl, followed by recovery and washing of solids, drying, and calcination. For amorphous silica, this procedure is reported to generate materials with Si/Zn ratios as low as 9 when the pH of the starting solution is 7.4, while decreasing pH of the starting solution leads to lower Zn contents.[24] CIT-6 exposed to 1.0 M H_2SO_4 for 12h, at ambient temperatures, (denoted CIT-6-de-Zn) loses most of its Zn (Si/Zn = 188 ± 17 is near the detection limit of EDS), leaving behind silanol nests that can host re-introduced Zn. Indeed, the application of the Zn-amine-based procedure leads to incorporation of Zn in CIT-6-de-Zn, with higher pH corresponding to higher Zn incorporation and higher MMBC yields (up to pH =6.9), at nearly identical conversions (see entries in Fig. 4.15 denoted as CIT-6-re-Zn-pH=X, where X corresponds to the initial pH in the re-zincation solution). At Si/Zn = 5.8 ± 0.2, CIT-6-re-Zn-pH=7.4 has a nominal Zn loading that exceeds that of the original material by a factor of 2. Such high Zn loading either suggests that the original CIT-6 material, prior to de-zincation, already possesses a number of unoccupied silanol nests, or that immobilization of extra-framework Zn species may also occur at higher pH.

Interestingly, CIT-6-de-Zn converts a significant amount of MMFC (27%), with low selectivity towards MMBC (15%). These data suggest that the side reactions do not correlate with decreased Zn spacing, but reveal that underlying non-selective sites may exist in CIT-6. Standard CIT-6 is synthesized in hydroxide media with Ludox AS-40 as the silica source. Thus, the byproduct-forming sites may be either highly active impurities from Ludox (Al or Fe) that are not removed by the acid treatment, or the numerous silanol defects that are generated upon de-zincation.

While the MMBC selectivity of CIT-6, or the various post-synthetically generated Zn-containing Beta zeotypes presented here, is still lower in heptane than that reported for Zr-Beta in dioxane (~70-80%), it is higher than that of Sn-Beta in dioxane (~50%).[13,43] Furthermore, a number of reactions reported here exceed the selectivity of Zr-Beta in heptane under identical reaction conditions (measured to be 42% here), and result in comparable net yields of MMBC. The MMBC selectivity of CIT-6 can be further increased to 62% by lowering the reaction temperature to 170 °C (Table 4.1).

Another interesting and more stable furan, 2,5-furandicarboxylic acid (FDCA), is formed upon oxidation of both side-groups of 5-HMF to carboxylic acid groups, and can be obtained in high yield and selectivity from 5-HMF, or can be made from fructose, with 5-HMF as an intermediate in a "one-pot" scheme.[44,45] The dimethyl ester of FDCA, dimethyl 2,5-furandicarboxylate (DMFDC), is used in its purification by vacuum distillation, and can be formed either through a separate esterification of FDCA, or directly and quantitatively during the oxidation of 5-HMF.[46] DA cycloaddition-dehydration reactions of ethylene with FDCA and DMFDC ($R_1 = R_2$ = COOH or COOMe in Fig. 4.14, respectively), are attractive direct routes to terephthalic acid (TPA) and dimethyl terephthalate (DMT), respectively, that do not require subsequent oxidation steps. Prior investigations of such reactions catalyzed by Sn-Beta showed that both of these substrates were highly resistant to DA reactions. Only under forcing conditions (300 °C) did DMT form from DMFDC in dioxane solvent, with a molar yield of 0.4% and >1% selectivity.[13,47] A BP patent reports no formation of DMT, but a molar yield of 0.023% of TPA, at 0.038% selectivity, when DMFDC is reacted with ethylene without a catalyst in toluene solvent at 190-195 °C.[48] Similarly a Furanix – Coca-Cola patent application reports a 7.2-11.6% yield of TPA, at an undisclosed conversion or selectivity, without any DMT observed, when DMFDC is reacted with ethylene in homogeneous acid/acetic anhydride mixtures at 240 °C.[49]

CIT-6 is able to catalyze the formation of DMT from DMFDC at 190 °C, with a yield of 3.4% and 5.1% selectivity (Fig. 4.17). GC-MS and ^{1}H NMR spectra (Figs. 4.18 and 4.19) of the reaction solutions indicate significant quantities of three byproducts: methyl 2-furoate (MF), methyl benzoate (MB), and 2-cyclohexenone (CHO), at 50.5%, 5.3%, and 2.8% yield (measured by GC-FID), respectively. MF is hypothesized to form through decarboxylation reactions of DMFDC, while MB may form either through a DA step with ethylene from MF, or as a decarboxylation product from DMT. No significant formation of MB was observed when DMT was used as a reactant, suggesting that the latter scenario is not likely. CHO is potentially formed from the DA product of ethylene and furan, as shown in Fig. 4.20. After the DA cycloaddition, the resulting 7-oxabicyclo[2.2.1]hept-2-ene adduct can rearrange to an epoxide, as is proposed to occur in the Lewis acid catalyzed dehydration of the DA adduct of dimethyl furan.[42] Subsequently, the epoxide can be isomerized into the enone by a Lewis-acid-promoted hydride shift.[50] The presence of this product suggests that furan and benzene should also form, but these species are only observed in GC-MS at very small relative amounts, and are poorly resolved from solvent peaks. Furthermore, because these species are significantly more volatile than any other component of the reaction solution they may be removed in part during vessel depressurization. For these reasons, we did not attempt to quantify the yields of furan and benzene in this work. Fig. 4.21 summarizes the hypothesized reaction network.

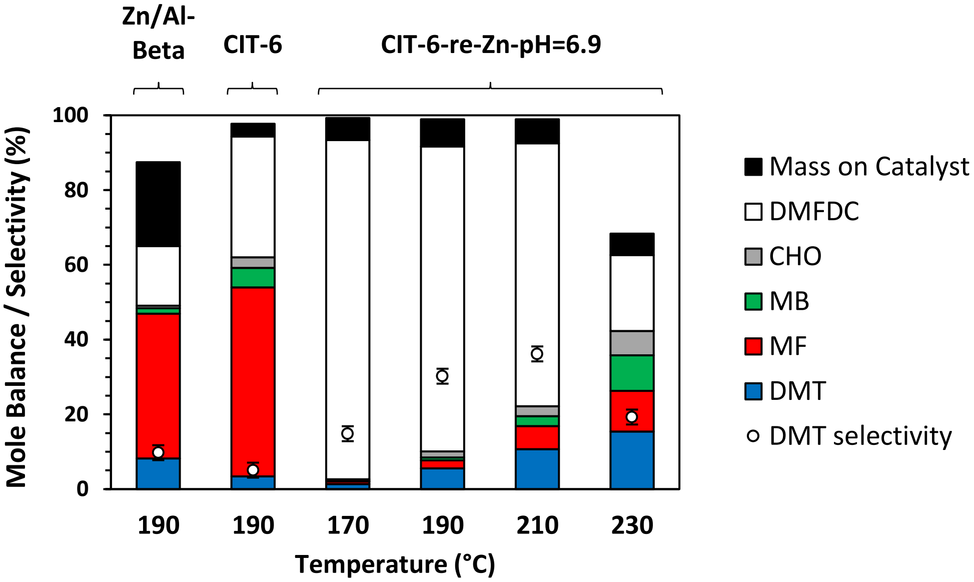

Figure 4.17 Diels-Alder cycloaddition-dehydration reactions of DMFDC catalyzed by CIT-6 and CIT-6-re-Zn-pH=6.9 at various temperatures. Resulting yields (%) of DMT, MF, MB, CHO, and DMFDC are calculated as ratio of moles formed to initial moles of DMFDC. Mass on catalyst (%) is expressed as ratio of combustible mass on catalyst (measured by TGA) to initial mass of DMFDC. Reaction conditions: 12h, effective concentration of 0.033M DMFDC in 10 mL heptane, 100 mg of catalyst, and 35 bar C_2H_2 at 25 °C.

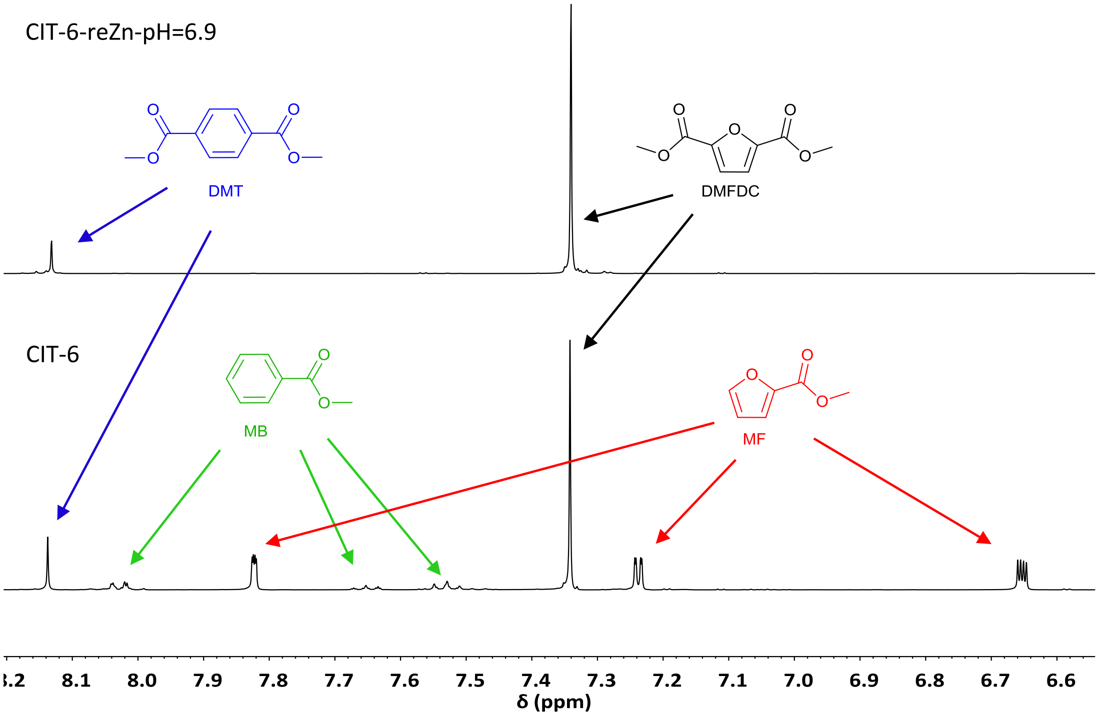

Figure 4.18 ^{1}H NMR spectrum of unseparated reactant (DMFDC) and the products (DMT, MB, and MF) generated by CIT-6 (bottom) and CIT-6-reZn-pH=6.9 (top) at 190 °C after a 12h DA cycloaddition-dehydration reaction in heptane.

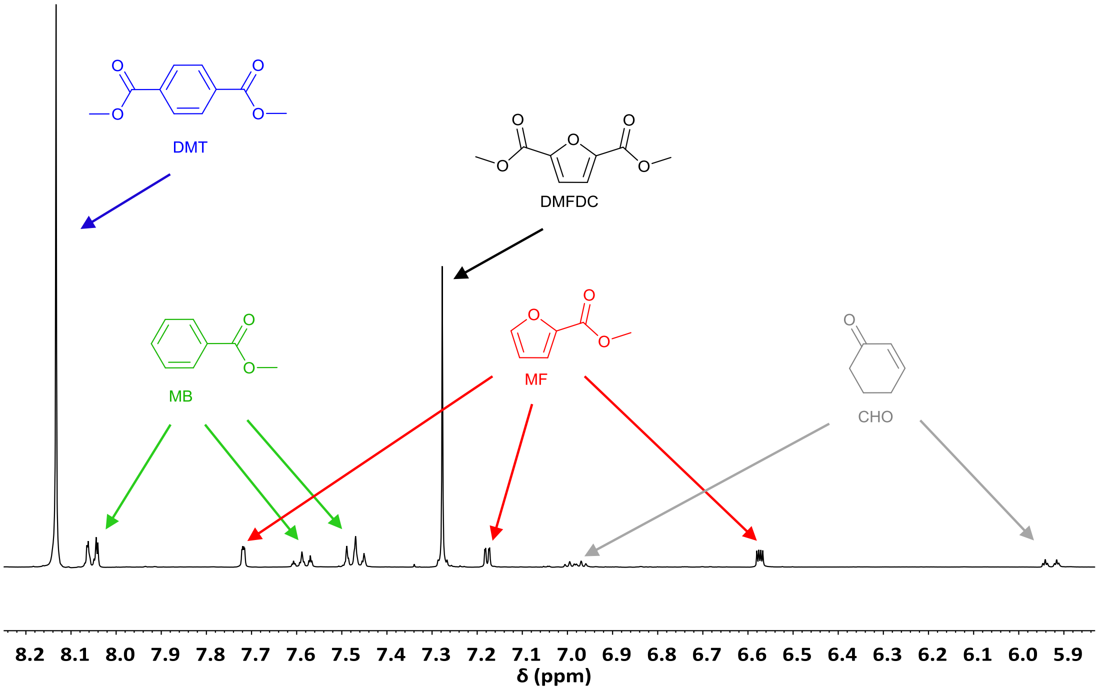

Figure 4.19 ^{1}H NMR spectrum of unseparated reactant (DMFDC) and the products (DMT, MB, MF, and CHO) generated by CIT-6-reZn-pH=6.9 at 230 °C after a 12h DA cycloaddition-dehydration reaction in heptane.

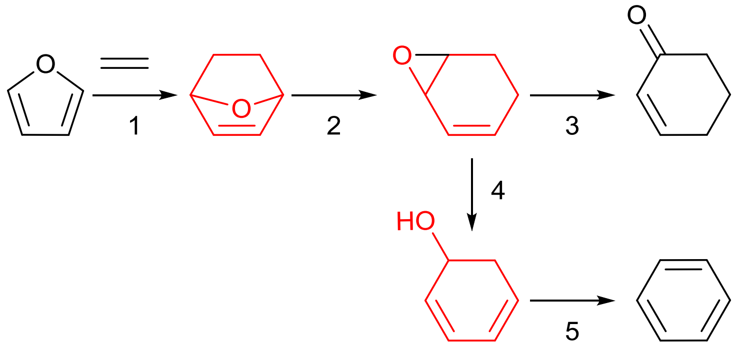

Figure 4.20 Proposed mechanism of formation of 2-cyclohexenone and benzene from furan. Step 1 is a Diels-Alder cycloaddition step. Step 2 is a Lewis acid promoted rearrangement to an epoxide proposed for the dimethyl furan analog of the oxa-norbornene cycloadduct. Step 3 is a Lewis acid promoted hydride shift that isomerizes the epoxide to the enone. Benzene is hypothesized to form through steps 4 and 5 that are also proposed for the analogous dehydrative-aromatization of dimethyl furan to p-xylene. Intermediates highlighted in red were not detected in this study.

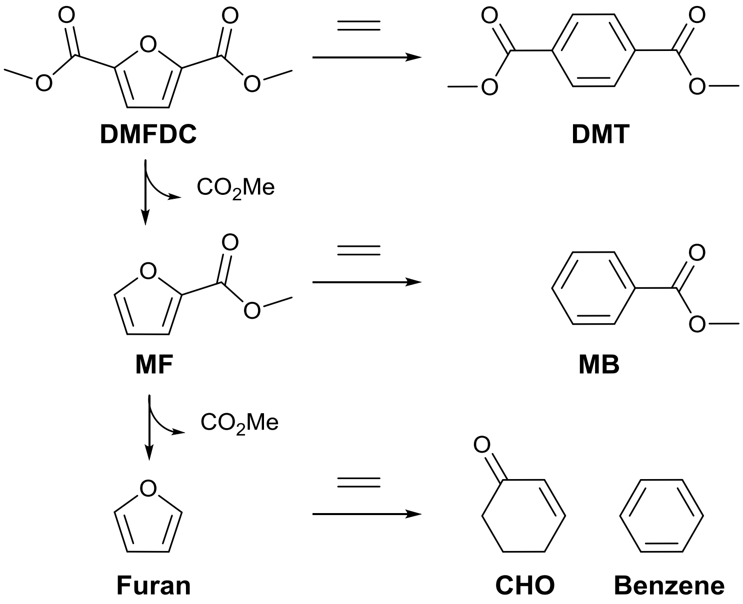

Figure 4.21 Full Diels-Alder cycloaddition-dehydration reaction diagram for DMFDC as a substrate. In the case of CIT-6, decarboxylation reactions are primarily catalyzed by Li-bearing sites.

With Sn-Beta catalysts, the disodium salt of FDCA was reported to primarily decarboxylate rather than produce DA products.[47] Furthermore, decarboxylation reactions of esters are generally hypothesized to proceed through free acid or carboxylate intermediates, which may be stabilized by alkali ions.[51] Thus, the Li-bearing sites of CIT-6 were suspected as a potential source for such decarboxylation reactions. CIT-6-re-Zn-pH=6.9 does not possess Li-bearing sites, and results in nearly double DMT yield (5.6%) and significantly higher selectivity (30.2%) than the parent CIT-6 material. Furthermore, elimination of the Li-bearing sites significantly reduces the production of MF, MB, and CHO to 2.1%, 0.8%, 1.7%. Analogous decarboxylation products, 2-(methoxymethyl)furan and (methoxymethyl)benzene, were not observed in product solutions of MMFC reactions with Li-containing catalysts (Fig. 4.12), but such species may be intermediates in coking that is observed for the MMFC reactions on CIT-6. While undesirable here, sites responsible for decarboxylation reactions of FDCA may be of interest in the context of Henkel reactions that have been shown to be catalyzed by $ZnCl_2$.[52] We note that at 190 °C, Zn/Al-Beta also catalyzes the formation of DMT, with a 9.0% DMT yield and 10.8% selectivity. Significant amounts of decarboxylation products are observed with this material, with 36.4%, 1.4%, and 0.7% yields of MF, MB, and CHO, respectively.

TGA mass losses above 250 °C for the acetone-washed catalyst from DMFDC reactions catalyzed by CIT-6 and CIT-6-re-Zn-pH=6.9 correspond to 3.4% and 7.4% of the initial DMFDC mass, respectively (after adjusting for any solvent retention, determined by TGA of acetone-washed, unreacted catalyst). Thus, despite the large difference in conversion and side-product formation, the difference in substrate adsorption or coking is minor. Additionally, unlike the yellow-brown color of catalysts after reactions of MMFC, both catalysts appear white after DMFDC reactions. In contrast, the Zn/Al-Beta catalyst turned red-brown after DMFDC reactions, suggesting a greater extent of coking occurred on this catalysts, as corroborated by the increase in TGA mass loss to 22.5% of initial DMFDC mass. Mole balance data (based on moles DMFDC) for CIT-6 and CIT-6-re-Zn-pH=6.9, for temperatures ranging from 170 °C to 230 °C, are shown in Fig. 4.17. The yield of DMT progressively increases with temperature, and despite the accompanying growth of MF, MB, and CHO, the apparent selectivity for DMT also increases up to 36.2%, at 210 °C, as the combustible mass deposited onto the catalyst does not appear to change significantly, and constitutes a progressively smaller fraction of the conversion. The large decrease in mole balance closure at 230 °C is not accompanied by increase in coking or detectable formation of new product species (as characterized by GC and NMR); however, volatile species like benzene and furan escape quantification under the current experimental protocols, and may constitute a larger fraction of the conversion.

Preliminary investigation of catalyst stability and recyclability were performed with CIT-6-reZn-pH=6.9 for the DA reaction of DMFDC and ethylene at 210 °C. These experiments suggest that, while the catalyst retains activity without intermediate calcination, the product distribution after each run changes, with decarboxylation reactions becoming more prominent, and contributing to decreased DMT selectivity (Fig. 4.22). Furthermore, calcination of the catalyst after the second reuse does not restore the initial selectivity. Neither the XRD pattern of (Fig. 4.23) nor the qualitative IR spectrum of CD_3CN adsorbed on (Fig. 4.24) the catalyst recovered after the third run are appreciably changed. Within certainty of EDS measurements, the Si/Zn ratio of the catalyst also remained constant throughout these experiments (Fig. 4.25). Thus, more extensive recyclability tests and new probes for the changes to active site structure are needed to understand the evolution of the catalyst activity and selectivity.

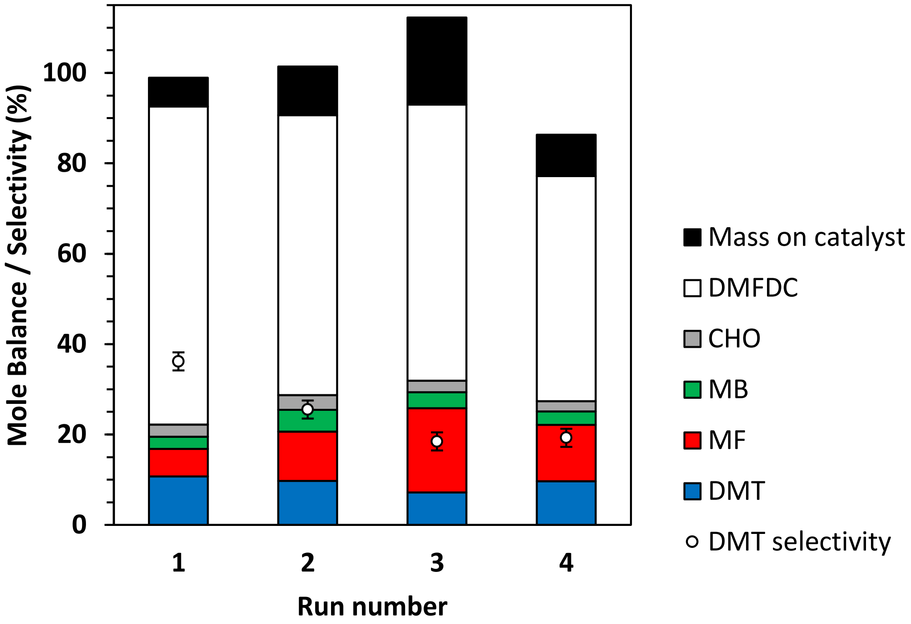

Figure 4.22 Catalyst recycle experiments for Diels-Alder cycloaddition-dehydration reactions of DMFDC catalyzed by CIT-6-re-Zn-pH=6.9 at 210 °C. Run 1 uses as-made CIT-6-re-Zn-pH=6.9; Run 2 uses catalyst recovered after Run 1, triply washed by acetone, and dried; Run 3 uses catalyst recovered after Run 2, triply washed by acetone, and dried; Run 4 uses catalyst recovered after Run 3, triply washed by acetone, dried, and calcined. Resulting yields (%) of DMT, MF, MB, CHO, and DMFDC are calculated as ratio of moles formed to initial moles of DMFDC. Mass on catalyst (%) is expressed as ratio of combustible mass on catalyst (measured by TGA) to initial mass of DMFDC. Reaction conditions: reagent and solvent ratios were adjusted to keep constant ratio to inorganic catalyst content between runs; 35 bar C_2H_2 at 25 °C, 12h reaction time.

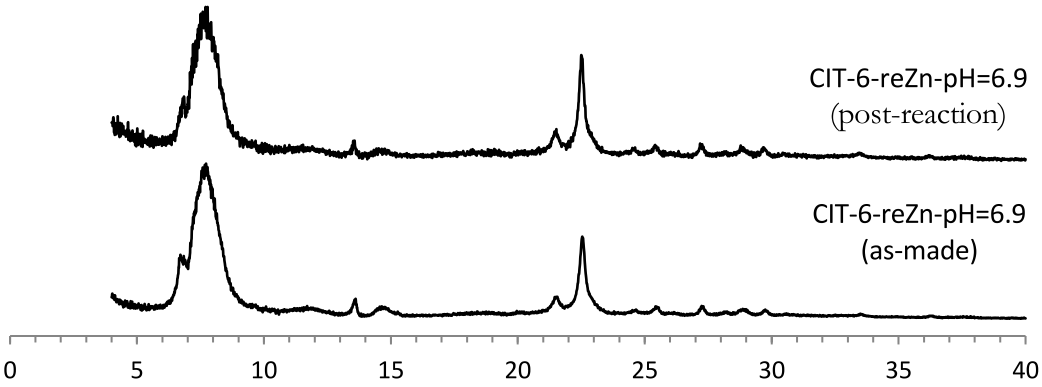

Figure 4.23 Normalized powder XRD data for as-made CIT-6-reZn-pH=6.9 (bottom), and CIT-6-reZn-pH=6.9 recovered after Run 3 in Fig. 4.22 (top).

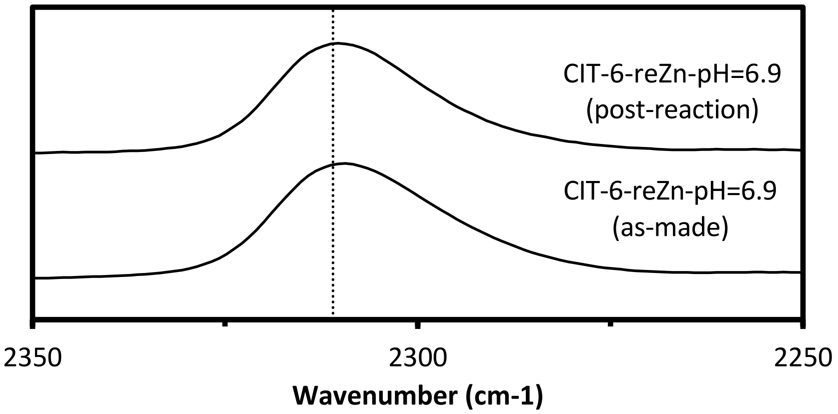

Figure 4.24 Baseline-corrected, normalized IR spectra of CD_3CN adsorbed at 35 °C on as-made CIT-6-reZn-pH=6.9 (bottom), and CIT-6-reZn-pH=6.9 recovered after Run 3 in Fig. 4.22 (top). Spectra were collected after desorption at 100 °C for 1h.

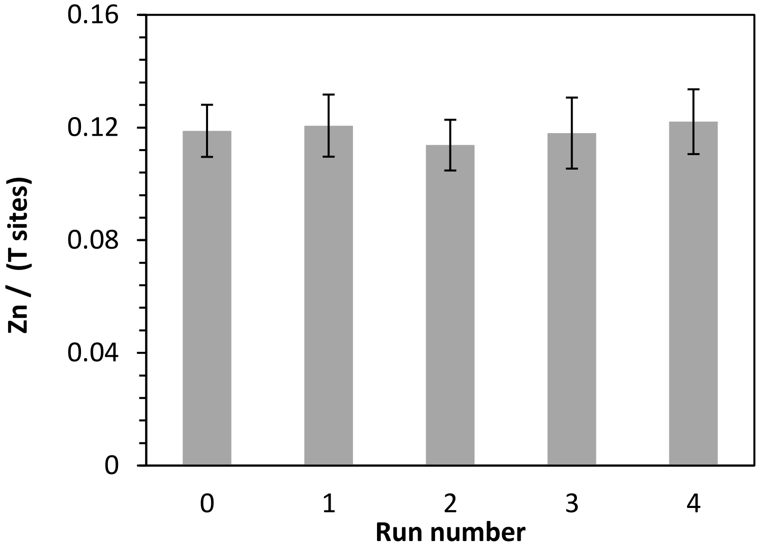

Figure 4.25 Zn content (as measured by EDS) of catalysts recovered after each run shown in Fig. 4.22. Run 0 corresponds to as-made CIT-6-re-Zn-pH=6.9 before Run 1; Run 1 uses as-made CIT-6-re-Zn-pH=6.9; Run 2 uses catalyst recovered after Run 1, triply washed by acetone, and dried; Run 3 uses catalyst recovered after Run 2, triply washed by acetone, and dried; Run 4 uses catalyst recovered after Run 3, triply washed by acetone, dried, and calcined.

The net processes for biomass-based production of DMT involve the synthesis and purification steps of the furan reactants, as well as any subsequent product processing. DMFDC is a more attractive substrate from the standpoint of its stability and the elimination of oxidation steps after the DA reactions. The data presented here show that isolated Zn sites in the *BEA framework offer significant improvement in both yield and selectivity of DA cycloaddition-dehydration reactions of ethylene and DMFDC over previously investigated heterogeneous catalysts. While both metrics remain lower for the DA reactions of DMFDC than for MMFC, these results indicate that such reactions are feasible, and warrant further consideration. Additionally, the identified side products of

DMFDC reactions, MF, MB, CHO, furan, and benzene, have industrial applications, and do not correspond to complete loss of carbon.[53,54]

4.4 Conclusions

Framework Zn sites in microporous zincosilicates behave as Lewis acid centers in probe-molecule IR spectroscopy, with unusually high adsorption energies of Lewis bases on such materials. The strong interactions with adsorbates severely limit the activity of zincosilicates at low temperatures and in solvents bearing Lewis basic groups for reactions catalyzed by Lewis acids (e.g. inter- and intra-molecular MVPO reactions). However, at higher temperatures, in heptane solvent, CIT-6 (Zn-Beta) is able to catalyze Diels-Alder cycloaddition-dehydration reactions of ethylene with methyl 5-(methoxymethyl)furan-2-carboxylate, a promising route to biomass-based terephthalic acid. Furthermore, a CIT-6-based catalyst enables the use of the dimethyl ester of furan-2,5-dicarboxylic acid, a furan resistant to Diels-Alder cycloaddition-dehydration reactions catalyzed by known Lewis acid zeotypes (e.g., Sn-Beta), resulting in direct formation of dimethyl terephthalate without the need for further oxidation reactions. Elimination of alkali-bearing sites is shown to significantly improve the selectivity of such reactions towards dimethyl terephthalate by lowering the extent of decarboxylation side-reactions that result in the formation of the notable byproducts: methyl 2-furoate, methyl benzoate, and 2-cyclohexenone. Here, only zincosilicates with *BEA topology have been demonstrated to be of catalytic interest, but probe-molecule IR characterization suggests that the Lewis-acidic character of isolated Zn sites in pure-silica frameworks is general, and that such materials warrant broader consideration for high temperature catalytic applications, especially those sensitive to the presence of strong Brønsted acid sites.

4.5 Acknowledgements

This work was financially supported as part of the Catalysis Center for Energy Innovation, an Energy Frontier Research Center funded by the US Department of Energy, Office of Science, Office of Basic Energy Sciences under Award DE-SC0001004. M.O. acknowledges funding from the National Science Foundation Graduate Research Fellowship Program under Grant DGE-1144469. Any opinions, findings, and conclusions or recommendations expressed in this material are those of the author(s) and do not necessarily reflect the views of the National Science Foundation. We thank Dr. Stacey I. Zones (Chevron Energy Technology Company) for supplying the structure directing agent used in the synthesis of SSZ-33 and for helpful discussions, Dr. Mona Shahgholi (Caltech) for the use of GC-MS, and Dr. Joshua Pacheco and Dr. Mark Deimund for helpful discussions regarding the technical aspects of Diels-Alder reactions and CIT-6 synthesis, respectively.

4.6 References

(1) Corma, A.; Nemeth, L. T.; Renz, M.; Valencia, S. *Nature* **2001**, *412* (6845), 423–425.

(2) Corma, A.; Domine, M. E.; Valencia, S. *J. Catal.* **2003**, *215* (2), 294–304.

(3) Boronat, M.; Corma, A.; Renz, M. *J. Phys. Chem. B* **2006**, *110* (42), 21168–21174.

(4) Blasco, T.; Camblor, M. A.; Corma, A.; Esteve, P.; Guil, J. M.; Martínez, A.; Perdigón-Melón, J. A.; Valencia, S. *J. Phys. Chem. B* **1998**, *102* (1), 75–88.

(5) Lewis, J. D.; Van De Vyver, S.; Crisci, A. J.; Gunther, W. R.; Michaelis, V. K.;

Griffin, R. G.; Román-Leshkov, Y. *ChemSusChem* **2014**, *7* (8), 2255–2265.

(6) Notari, B. In *Chemistry of Microporous CrystalsProceedings of the International Symposium on Chemistry of Microporous Crystals*; Tomoyuki lnui, S. N., Tatsumi, T., Eds.; Studies in Surface Science and Catalysis; Elsevier, 1991; Vol. 60, pp 343–352.

(7) Khouw, C. B.; Dartt, C. B.; Labinger, J. A.; Davis, M. E. *J. Catal.* **1994**, *149* (1), 195–205.

(8) Khouw, C. B.; Davis, M. E. *J. Catal.* **1995**, *151* (1), 77–86.

(9) Dartt, C. B.; Davis, M. E. *Appl. Catal. A Gen.* **1996**, *143* (1), 53–73.

(10) Corma, A.; Domine, M. E.; Nemeth, L.; Valencia, S. *J. Am. Chem. Soc.* **2002**, *124* (13), 3194–3195.

(11) Moliner, M.; Román-Leshkov, Y.; Davis, M. E. *Proc. Natl. Acad. Sci. USA* **2010**, *107* (14), 6164–6168.

(12) Holm, M. S.; Saravanamurugan, S.; Taarning, E. *Science* **2010**, *328* (5978), 602–605.

(13) Pacheco, J. J.; Davis, M. E. *Proc. Natl. Acad. Sci. USA* **2014**, *111* (23), 8363–8367.

(14) Orazov, M.; Davis, M. E. *Proc. Natl. Acad. Sci. USA* **2015**, *112* (38), 11777–11782.

(15) Cho, H. J.; Chang, C.-C.; Fan, W. *Green Chem.* **2014**, *16* (7), 3428–3433.

(16) Fernandez-Lopez, R.; Kofoed, J.; Machuqueiro, M.; Darbre, T. *European J. Org. Chem.* **2005**, No. 24, 5268–5276.

(17) Palomo, C.; Oiarbide, M.; Laso, A. *Angew. Chemie Int. Ed.* **2005**, *44* (25), 3881–3884.

(18) McCall, K. A; Huang, C.; Fierke, C. A. *J. Nutr.* **2000**, *130* (5), 1437S – 1446S.

(19) Penzien, J.; Abraham, A.; van Bokhoven, J. A.; Jentys, A.; Müller, T. E.; Sievers, C.; Lercher, J. A. *J. Phys. Chem. B* **2004**, *108* (13), 4116–4126.

(20) Kolyagin, Y. G.; Ivanova, I. I.; Ordomsky, V. V.; Gedeon, A.; Pirogov, Y. A. *J. Phys. Chem. C* **2008**, *112* (50), 20065–20069.

(21) Bermejo-Deval, R.; Orazov, M.; Gounder, R.; Hwang, S.-J.; Davis, M. E. *ACS Catal.* **2014**, *4* (7), 2288–2297.

(22) Schweitzer, N. M.; Hu, B.; Das, U.; Kim, H.; Curtiss, L. A.; Stair, P. C.; Miller, T.; Hock, A. S.; Greeley, J.; Curtiss, L. A.; Stair, P. C.; Miller, J. T.; Hock, A. S. *Acs Catal.* **2014**, *4* (4), 1091–1098.

(23) Connell, G.; Dumesic, J. A. *J. Catal.* **1987**, *298*, 285–298.

(24) Kozawa, A. *J. Inorg. Nucl. Chem.* **1961**, *21* (3-4), 315–324.

(25) Takewaki, T.; Beck, L. W.; Davis, M. E. *J. Phys. Chem. B* **1999**, *103* (14), 2674–2679.

(26) Takewaki, T.; Beck, L. W.; Davis, M. E. *Top. Catal.* **1999**, *9* (3), 35–42.

(27) Deimund, M. A.; Labinger, J. A.; Davis, M. E. *ACS Catal.* **2014**, *4* (11), 4189–4195.

(28) Andy, P.; Davis, M. E. *Ind. Eng. Chem. Res.* **2004**, *43* (12), 2922–2928.

(29) Barri, S. A. I.; Tahir, R. Chemical process and catalyst. US5208201 A, 1993.

(30) Takewaki, T.; Hwang, S.-J.; Yamashita, H.; Davis, M. E. *Microporous Mesoporous Mater.* **1999**, *32* (3), 265–278.

(31) Chang, C.-C.; Wang, Z.; Dornath, P.; Je Cho, H.; Fan, W. *RSC Adv.* **2012**, *2* (28), 10475.

(32) Faggin, M. F.; Hines, M. A. *Rev. Sci. Instrum.* **2004**, *75* (11), 4547.

(33) Pelmenschikov, A. G.; van Santen, R. A.; Janchen, J.; Meijer, E. *J. Phys. Chem.* **1993**, *97* (42), 11071–11074.

(34) Lavalley, J. C. *Catal. Today* **1996**, *27* (3-4), 377–401.

(35) Ren, L.; Guo, Q.; Kumar, P.; Orazov, M.; Xu, D.; Alhassan, S. M.; Mkhoyan, K. A.; Davis, M. E.; Tsapatsis, M. *Angew. Chemie Int. Ed.* **2015**, *54* (37), 10848–10851.

(36) Osmundsen, C. M.; Holm, M. S.; Dahl, S.; Taarning, E. *Proc. R. Soc. A* **2012**, *468* (2143), 2000–2016.

(37) Boronat, M.; Concepcion, P.; Corma, A.; Navarro, M. T.; Renz, M.; Valencia, S. *Phys. Chem. Chem. Phys.* **2009**, *11*, 2876–2884.

(38) Serrano, D. P.; Van Grieken, R.; Davis, M. E.; Melero, J. A.; Garcia, A.; Morales, G. *Chem. - A Eur. J.* **2002**, *8* (22), 5153–5160.

(39) Bermejo-Deval, R.; Gounder, R.; Davis, M. E. *ACS Catal.* **2012**, *2* (12), 2705–2713.

(40) Luo, H. Y.; Consoli, D. F.; Gunther, W. R.; Román-Leshkov, Y. *J. Catal.* **2014**, *320*, 198–207.

(41) Chang, C.-C.; Green, S. K.; Williams, C. L.; Dauenhauer, P. J.; Fan, W. *Green Chem.* **2014**, *16* (2), 585.

(42) Nikbin, N.; Do, P. T.; Caratzoulas, S.; Lobo, R. F.; Dauenhauer, P. J.; Vlachos, D. G. *J. Catal.* **2013**, *297*, 35–43.

(43) Pacheco, J. J.; Labinger, J. A.; Sessions, A. L.; Davis, M. E. *ACS Catal.* **2015**, 5904–5913.

(44) Casanova, O.; Iborra, S.; Corma, A. *ChemSusChem* **2009**, *2* (12), 1138–1144.

(45) Ribeiro, M. L.; Schuchardt, U. *Catal. Commun.* **2003**, *4* (2), 83–86.

(46) Casanova, O.; Iborra, S.; Corma, A. *J. Catal.* **2009**, *265* (1), 109–116.

(47) Pacheco, J. J. New Catalysts for the Renewable Production of Monomers for Bioplastics, California Institute of Technology, 2015.

(48) Gong, W. H. Terephthalic acid composition and process for the production thereof.

US 7,385,081 B1, 2008.

(49) Wang, B.; Gruter, G. J. M.; Dam, M. A.; Kriegel, R. M. Process for the preparation of benzene derivatives from furan derivatives. WO Patent Appl. PCT/NL2013/050740, 2013.

(50) Ranu, B. C.; Jana, U. *J. Org. Chem.* **1998**, *63* (23), 8212–8216.

(51) Tunge, J. a.; Burger, E. C. *European J. Org. Chem.* **2005**, *2005* (9), 1715–1726.

(52) Dawes, G. J. S.; Scott, E. L.; Le Nôtre, J.; Sanders, J. P. M.; Bitter, J. H. *Green Chem.* **2015**.

(53) Kesavan, L.; Tiruvalam, R.; Ab Rahim, M. H.; bin Saiman, M. I.; Enache, D. I.; Jenkins, R. L.; Dimitratos, N.; Lopez-Sanchez, J. A; Taylor, S. H.; Knight, D. W.; Kiely, C. J.; Hutchings, G. J. *Science* **2011**, *331* (6014), 195–199.

(54) Holladay, J. E.; White, J. F.; Bozell, J. J.; Johnson, D. *Top Value-Added Chemicals from Biomass - Volume II-Results of Screening for Potential Candidates from Biorefinery Lignin*; Richland, WA, 2007; Vol. II.

Chapter 5

Conclusions and Future Directions

5.1 On the utility of active site characterization

Chapters 2 and 4 have discussed various aspects of characterization of poorly-understood molecular sieve catalysts with framework Sn or Zn Lewis acid centers. Chapters 3 and 4 demonstrate that information gained regarding site structures and properties, as well as reaction mechanisms, can aid in the development of novel catalytic systems that open new possibilities for biomass-derived chemicals.

As the work in Chapter 2 was published in 2014, sufficient time has passed for follow up work from the Davis group[1] and other laboratories[2] to further explore the claims in our original report. To this effect, experimental and computational studies on molecular model systems consisting of various tin silsesquioxanes structures that approximate the local environment of framework tin in Sn-Beta qualitatively agree with our claims of 1,2-intramolecular hydride shift (1,2-HS) reactions correlating to open Sn sites with proximal protonated silanols, and of 1,2-intramolecular carbon shift (1,2-CS) reactions correlating to open Sn sites lacking proximal protonated silanols.[1] Furthermore, recent results from the Gounder group confirm that, in Sn-Beta, the turnover frequency for the 1,2-HS reaction quantitatively (within experimental error) scales with number of open Sn sites, rather than the number of total Sn atoms.[2] These results are also consistent with the notion that, in Sn-Beta that is synthesized in fluoride media, closed Sn sites do not open on reaction time scales.

Our demonstration of the participation of the open Sn site's proximal silanol group in 1,2-HS reactions motivates further investigation of its role in other reactions proposed to be catalyzed by open Sn sites, e.g., Bayer-Villiger oxidation, and potentially aldol/retro-aldol reactions. Previous computational work suggests that the role of the proximal silanol in the 1,2-HS pathway may be to shuttle protons.[3] The general hypothesized mechanisms for Bayer-Villiger oxidation of ketones and retro-aldol reactions of sugars both involve proton abstraction and reallocation steps.[4,5] Furthermore, our probe-molecule FTIR data collected on the series of alkali-exchanged Sn-Beta materials (Li^+, Na^+, K^+) show that the identity of the alkali ion influences the frequency of the characteristic band of CD_3CN adsorbed on such exchanged sites, suggesting that the alkali ions may have direct or indirect influence on the modes of site-substrate interactions that go beyond the removal of the participation of the silanol in proton shuttling.

Data in Chapter 3 demonstrate that virtually all reported 1,2-CS catalysts also appear to promote retro-aldol reactions. Furthermore, after the publication[6] of our discovery of the effect of alkali contamination on the reactivity of Sn-Beta in moderate-temperature glucose isomerization reactions, the authors of the first study[7] of high-temperature retro-aldol reactions of sugars catalyzed by Sn-Beta, have re-evaluated[8] their Sn-Beta synthesis protocols and discovered that Sn-Beta samples synthesized in strictly alkali-free conditions are much less selective than samples made with low amounts of alkali cations present in the gel. This follow-up study[8] identifies a significant variability of Na^+ and K^+ contamination in the commonly-used commercial sources (Sigma-Aldrich) of the structure-directing reagent that is used in Sn-Beta synthesis (tetraethylammonium hydroxide). Thus, the authors could not rule out the possibility of alkali contamination in Sn-Beta samples used in their original study, and that the majority of retro-aldol activity in high-temperature retro-aldol reactions catalyzed by Sn-Beta stems from alkali-bearing Sn-sites.[8]

The perturbation generated by alkali exchange of Lewis acid sites does not appear to be unique to Sn. In our hands, Ti-Beta subjected to the same alkali exchange treatments, as used in Chapter 2 for Sn-Beta, also exhibits a different glucose isomerization activity from the parent material. In addition to the 1,2-HS reaction that forms D-fructose from D-glucose, Ti-Beta appears to promote a 1,5-HS that forms L-sorbose from D-glucose.[9] On the other hand, alkali-exchanged Ti-Beta promotes the 1,2-CS to D-mannose, at the expense of L-sorbose and D-fructose production via the 1,5-HS and 1,2-HS routes, respectively. Though data in Chapter 4 demonstrate that Zn Lewis acid sites appear to interact too strongly with Lewis bases to promote reactions at low-to-moderate temperatures, FTIR data and high-temperature Diels Alder reactions again demonstrate that the presence of alkali ions near a Lewis acid site leads to different (or additional) site-substrate interactions, which in turn may promote different reactions (such as decarboxylation of furans).

Further spectroscopic work, e.g., SS-NMR studies of adsorbed substrate conformations and polarization, as well as computational insights regarding these phenomena, may help with rational catalyst design and discovery of new reactions and applications for such Lewis-acid-bearing materials, especially in cases of complex substrates, such as those derived from biomass. Arguably, such studies also need to consider the potential effects that may arise from Lewis acid sites being located in the micropores of zeotypes. These effects may include hydrophobization of the active site surrounding environment, transition state confinement, and electronic effects due to lattice-induced strained geometry.

Finally, while probe-molecule spectroscopic studies may be instructive, all significant effects must be considered in the interpretation of the data. For instance, both the alkali-exchanged Sn-Beta samples and various zincosilicates reported in Chapters 2 and 4 have an apparent inconsistency between the high desorption temperature and the lower magnitude of the shift in the frequency of the characteristic band of CD_3CN in the IR. These observations may be rationalized by at least two scenarios. In the first, multiple interactions of the active site with the probe may contribute to an increase in the net magnitude of interaction energy, but may have conflicting effects on the frequency of the characteristic band. In the second scenario, some factors that contribute to the net adsorption energy may not necessarily increase the polarization of the probe molecule (e.g., energetic effects associated with geometric rearrangements of the Lewis acid center). Understanding if either of these scenarios are at play in the aforementioned materials would also be conducive to the understanding of their catalytic properties.

5.2 Further possibilities of Diels-Alder reactions of oxygenated substrates

In Chapter 4, the Diels-Alder reactions of two kinds of oxygenated furans were used to illustrate the catalytic potential of zincosilicate molecular sieves. The CIT-6 reaction results demonstrate that microporous zincosilicates can act catalytically under appropriately chosen conditions, and warrant further consideration in a broader set of high-temperature catalytic and separation processes, as their uniquely high adsorption energy may be advantageous in certain scenarios. For instance, to the best of our knowledge, CIT-6 is the first heterogeneous catalyst that has been reported to catalyze the Diels-Alder reaction of dimethyl 2,5-furandicarboxylate and ethylene in excess of 1% selectivity.[10]

While the best result (36 % selectivity towards dimethyl terephthalate with Li-free CIT-6) obtained in the study reported in Chapter 4 is certainly a large improvement over past literature,[10] significant room for further improvements remains. Prior literature for this reaction with dimethyl 2,5-furandicarboxylate on zeolite catalysts, and our initial assessment of Zn-exchanged aluminosilicate zeolites resulted in underwhelming results regarding dimethyl terephthalate selectivity.[10,11] In the case of Zn-exchanged Al-Beta, analysis of byproducts indicated that significant decarboxylation of the furan and coking of catalyst surface occurred. However, analyses of byproducts of purely aluminosilicate zeolites (e.g., Al-Beta and Al-USY) have subsequently revealed that on such materials, the decarboxylation of furans occurs to a much lesser extent. Instead, at temperatures that are considered relatively low for such DA reactions (ca. 170 °C), the main side-reactions appear to be the hydration of ethylene and subsequent transesterification of furans and terephthalates to the respective ethyl esters. Furthermore, if we define a selectivity based on the total conversion of furan diesters and the total yield of terephthalates, surprisingly high selectivities (upwards of 88 %) can be obtained with commercially-available aluminosilicate zeolites.

Thus, while prior studies suggested that the strong Brønsted acidity of aluminosilicate zeolites makes them incompatible with oxygenated furans at typical Diels-Alder reaction conditions,[11,12] our recent results suggest that this assessment may need further evaluation. Furthermore, these results elucidate an important point that, from our perspective, has been underreported in the community: Brønsted acid sites in aluminosilicates can hydrate ethylene at DA reaction conditions. Unless careful measures are taken, the hydrophilic aluminosilicate catalysts used in these reactions will adsorb water. Furthermore, water is produced in the dehydrative-aromatization of the DA reaction. Thus, the potential for ethylene hydration is difficult to exclude. To date, most catalytic DA studies report only the conversions of furans, and not of ethylene. While the latter conversion is difficult to measure (not possible with our current experimental setup), it may be important in the economic assessment of industrial processes based on this technology, and in evaluation of site-specific catalytic performance. The apparent lack of ethyl ester or ether byproducts in the DA reactions of various oxygenated furans and ethylene catalysed by Lewis acid molecular sieves (e.g., Zr-Beta) suggest that such materials may not appreciably catalyze ethylene hydration. However, in the case of the commonly studied dimethyl furan, transesterification is precluded by sidegroup functionality, and the occurrence of ethylene hydration cannot be ruled out without further study.

5.3 References

(1) Brand, S. K.; Labinger, J. A.; Davis, M. E. *ChemCatChem* **2016**, *8* (1), 121–124.

(2) Harris, J. W.; Cordon, M. J.; Di Iorio, J. R.; Vega-Vila, J. C.; Ribeiro, F. H.; Gounder, R. *J. Catal.* **2016**, *335*, 141–154.

(3) Rai, N.; Caratzoulas, S.; Vlachos, D. G. *ACS Catal.* **2013**, *3* (10), 2294–2298.

(4) Corma, A.; Nemeth, L. T.; Renz, M.; Valencia, S. *Nature* **2001**, *412* (6845), 423–425.

(5) Fessner, W.; Schneider, A.; Held, H.; Sinerius, G.; Walter, C.; Hixon, M.; Schloss, J. V. *Angew. Chemie Int. Ed. English* **1996**, *35* (19), 2219–2221.

(6) Bermejo-Deval, R.; Orazov, M.; Gounder, R.; Hwang, S.-J.; Davis, M. E. *ACS Catal.* **2014**, *4* (7), 2288–2297.

(7) Holm, M. S.; Saravanamurugan, S.; Taarning, E. *Science* **2010**, *328* (5978), 602–605.

(8) Tolborg, S.; Sádaba, I.; Osmundsen, C. M.; Fristrup, P.; Holm, M. S.; Taarning, E. *ChemSusChem* **2015**, *8* (4), 613–617.

(9) Gounder, R.; Davis, M. E. *ACS Catal.* **2013**, *3* (7), 1469–1476.

(10) Orazov, M.; Davis, M. E. *Chem. Sci.* **2016**, *7* (3), 2264–2274.

(11) Pacheco, J. J. New Catalysts for the Renewable Production of Monomers for Bioplastics, California Institute of Technology, 2015.

(12) Pacheco, J. J.; Davis, M. E. *Proc. Natl. Acad. Sci. USA* **2014**, *111* (23), 8363–8367.

Appendix A: Supplementary Information for Chapter 2

A1. X-ray diffractograms of zeolite samples

Powder X-ray diffraction patterns of the samples used in Chapter 2 are shown in Figs. A1 and A2.

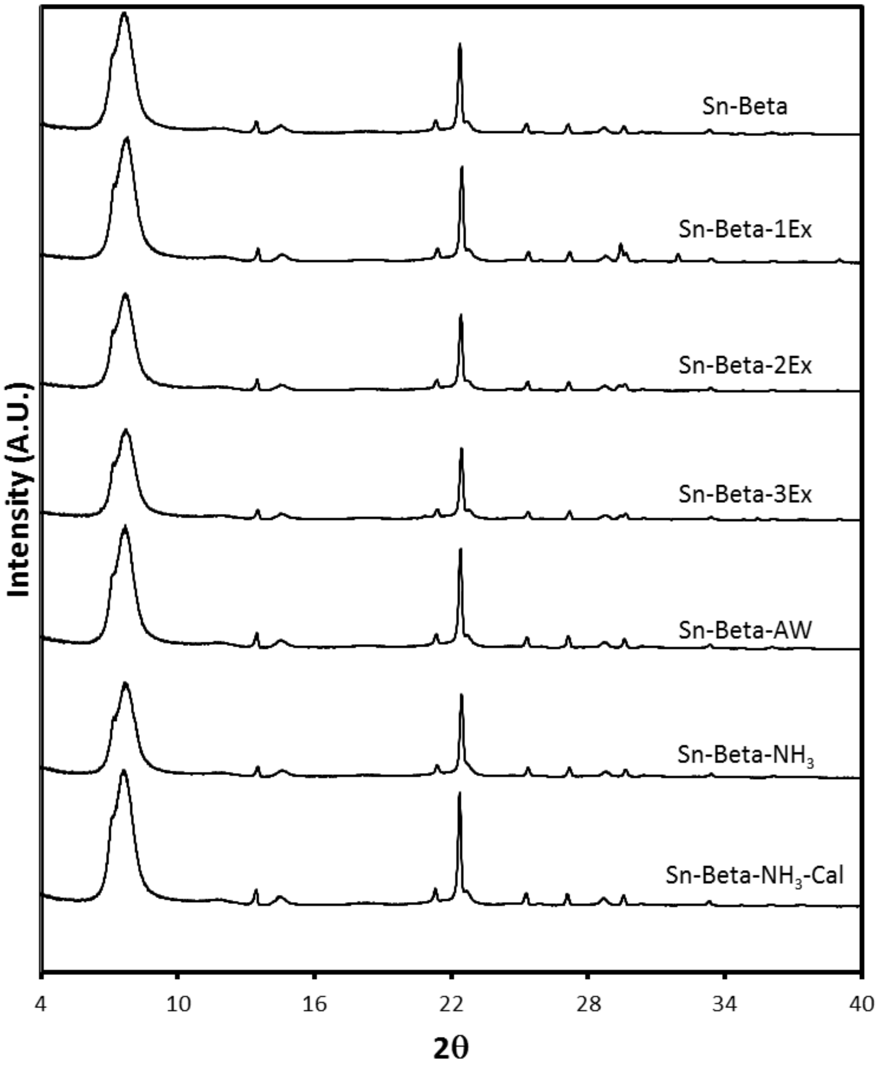

Figure A1 Powder X-ray powder diffraction patterns of Sn-Beta, Sn-Beta-1Ex, Sn-Beta-2Ex, Sn-Beta-3Ex, Sn-Beta-AW, Sn-Beta-NH$_3$, and Sn-Beta-NH$_3$-Cal (top to bottom).

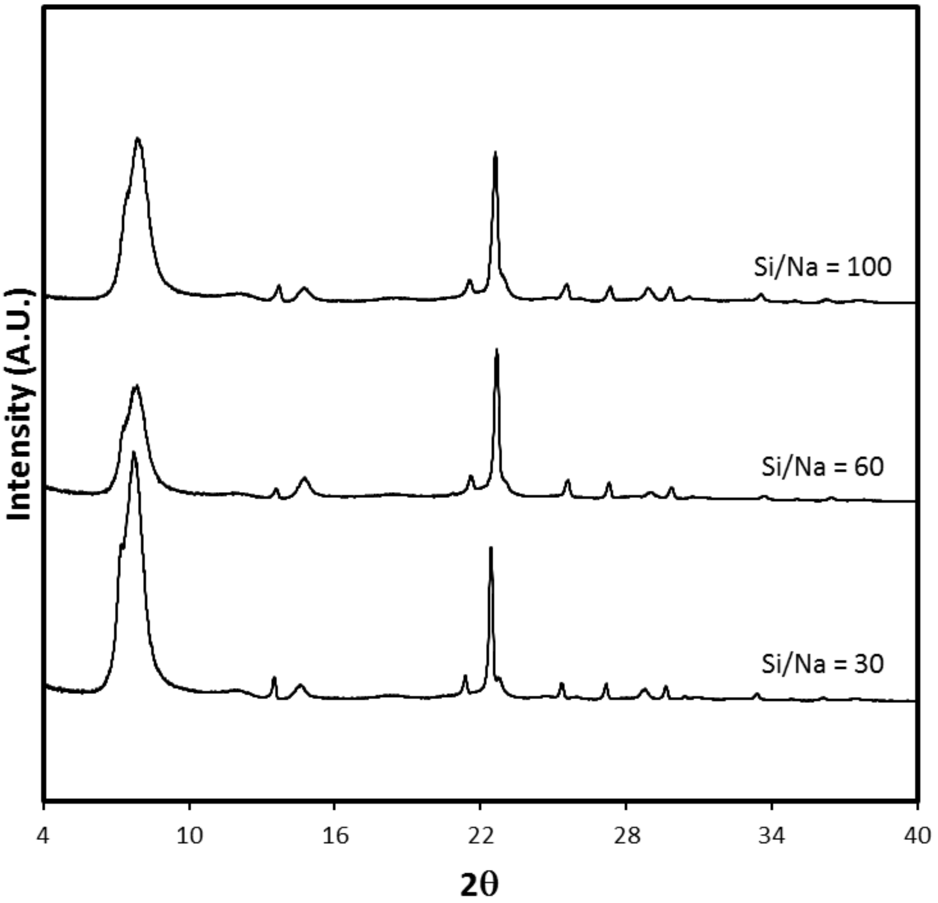

Figure A2 Powder X-ray powder diffraction patterns of Sn-Beta with Si/Na synthesis gel composition of 100, 60, and 30.

A2. SEM images of zeolite samples

SEM images of Sn-Beta, Sn-Beta-1Ex, Sn-Beta-3Ex, Sn-Beta-NH_3, and Na-Sn-Beta used in Chapter 2 are shown at different magnifications in Figures A3 and A4.

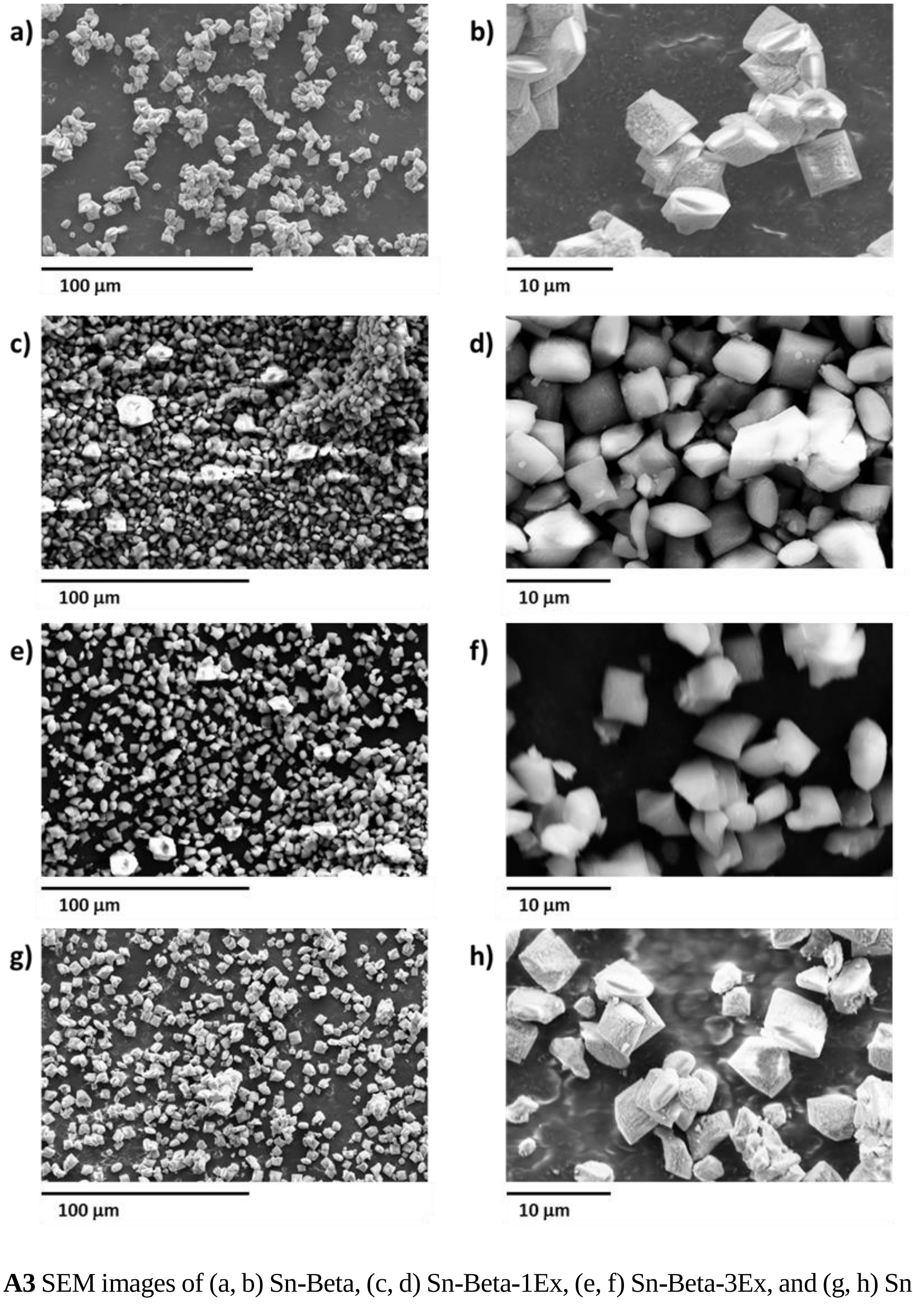

Figure A3 SEM images of (a, b) Sn-Beta, (c, d) Sn-Beta-1Ex, (e, f) Sn-Beta-3Ex, and (g, h) Sn-Beta-NH_3.

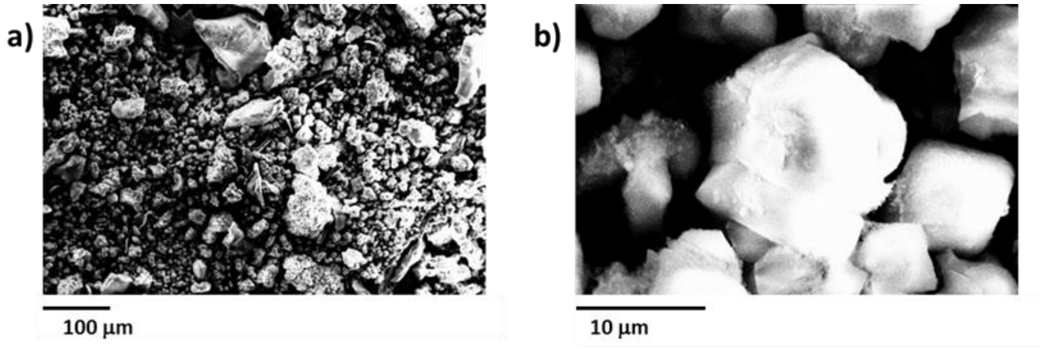

Figure A4 SEM images of Na-Sn-Beta-30.

A3. Ar adsorption isotherms of zeolite samples

Total micropore volume of each sample in Chapter 2 was determined from linear extrapolation of its Ar uptake in the mesopore regions (P/P_0 ~ 0.1-0.4) to zero relative pressure and from the liquid Ar molar density (0.035 mol cm^{-3}).

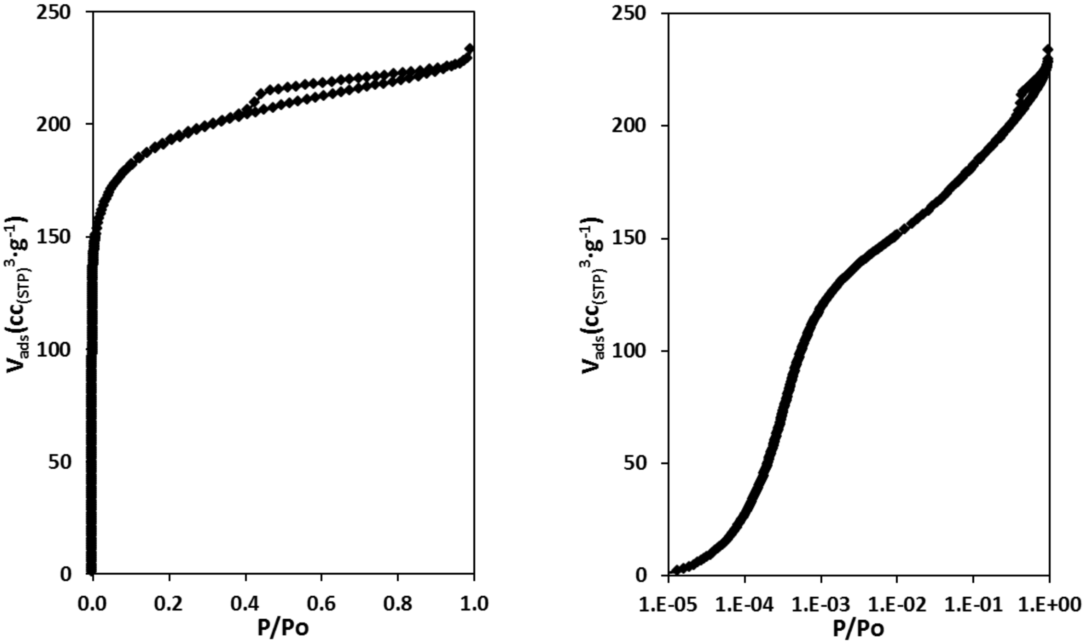

Figure A5 Ar adsorption isotherm (87 K) for Sn-Beta.

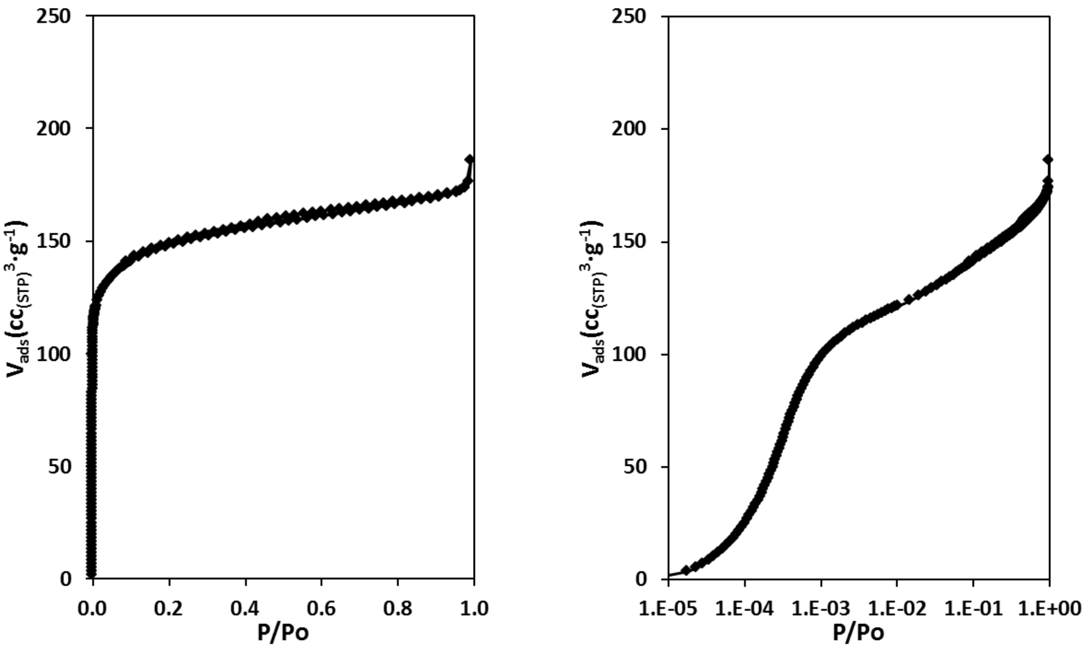

Figure A6 Ar adsorption isotherm (87 K) for Sn-Beta-1Ex.

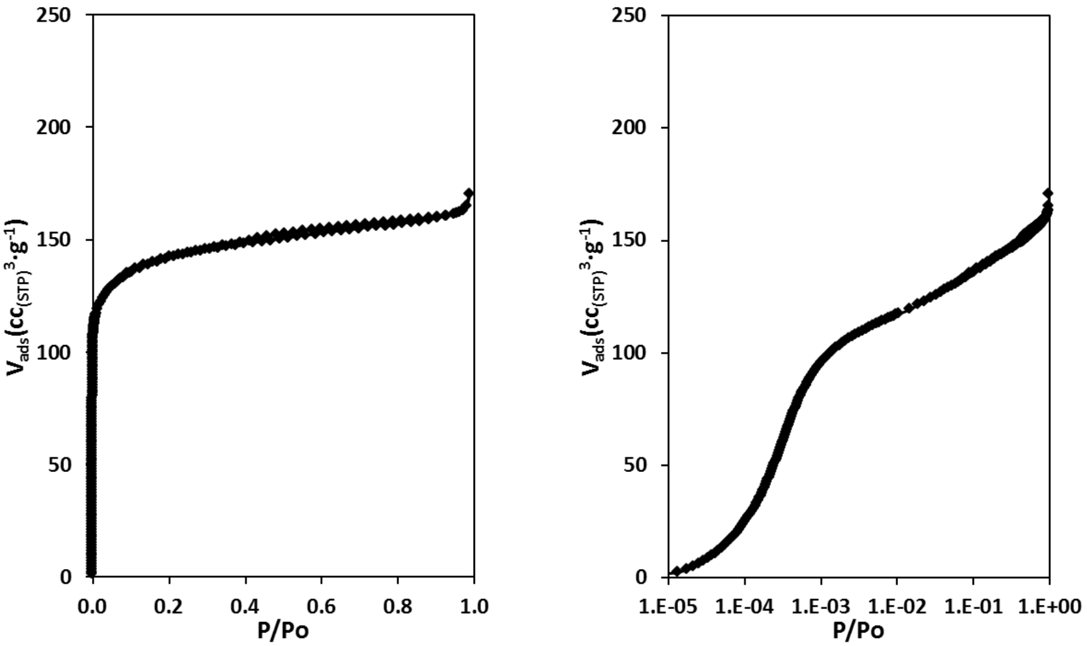

Figure A7 Ar adsorption isotherm (87 K) for Sn-Beta-2Ex.

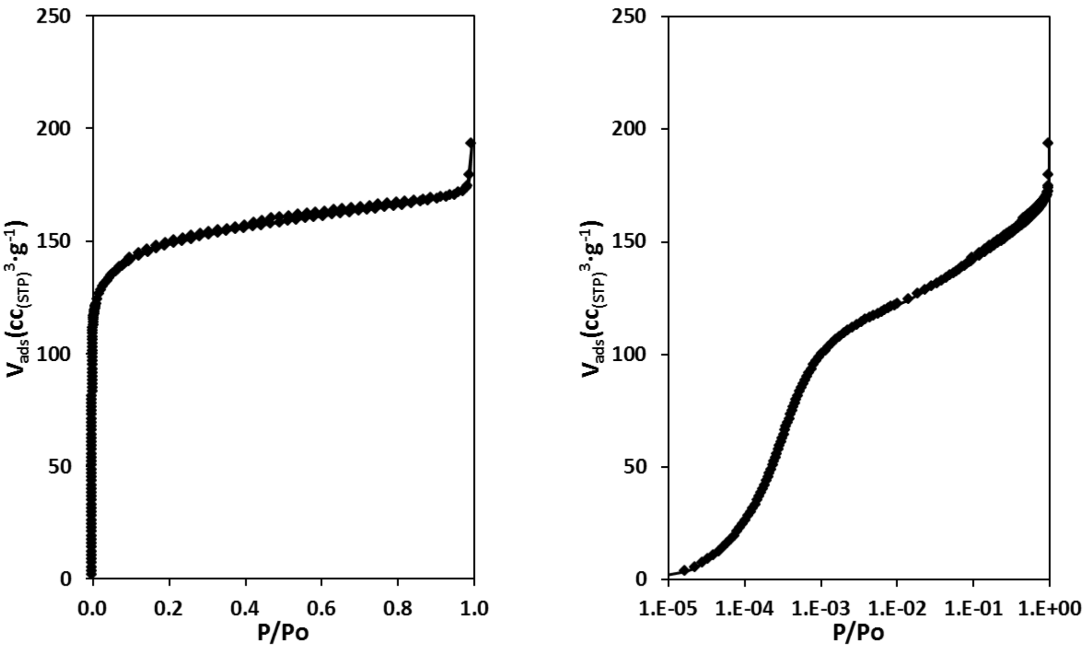

Figure A8 Ar adsorption isotherm (87 K) for Sn-Beta-3Ex.

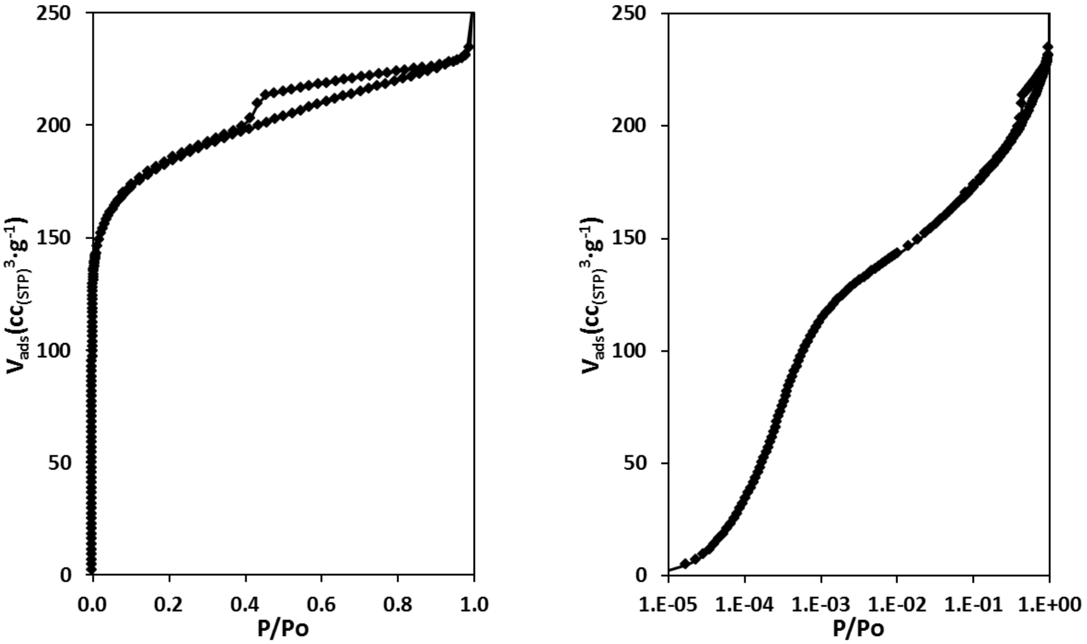

Figure A9 Ar adsorption isotherm (87 K) for Sn-Beta-AW.

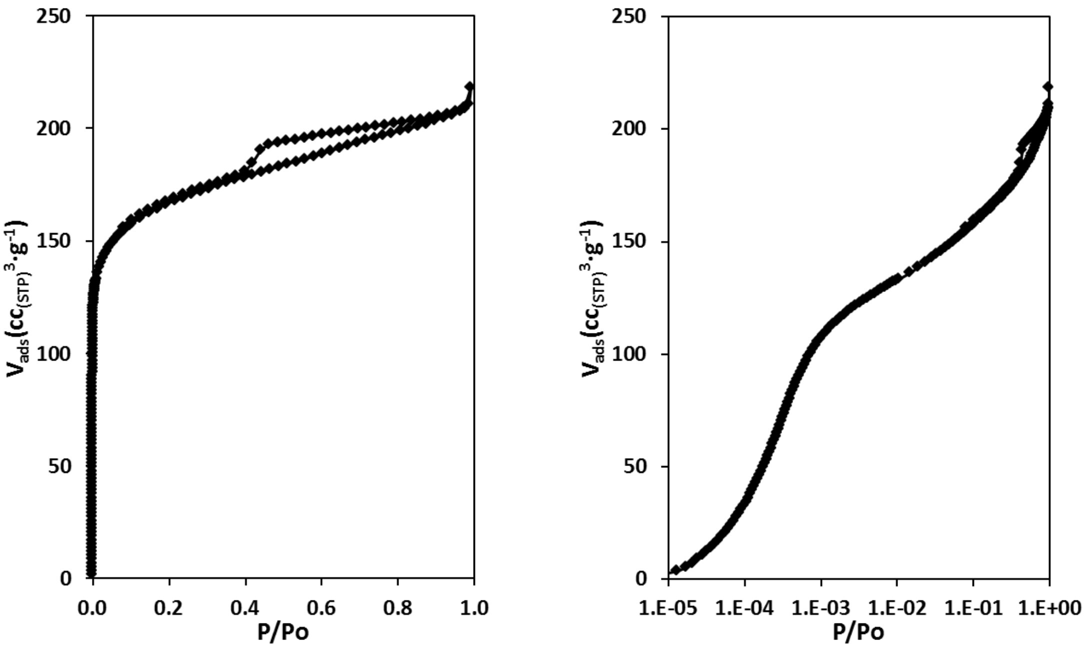

Figure A10 Ar adsorption isotherm (87 K) for Sn-Beta-NH_3.

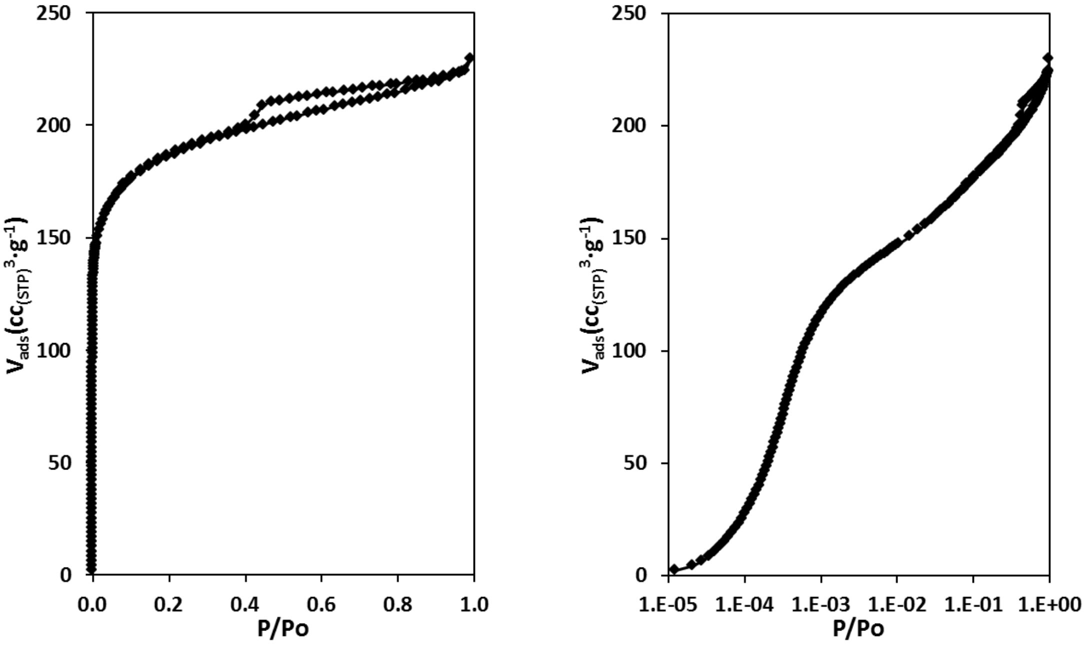

Figure A11 Ar adsorption isotherm (87 K) for Sn-Beta-NH_3-Cal.

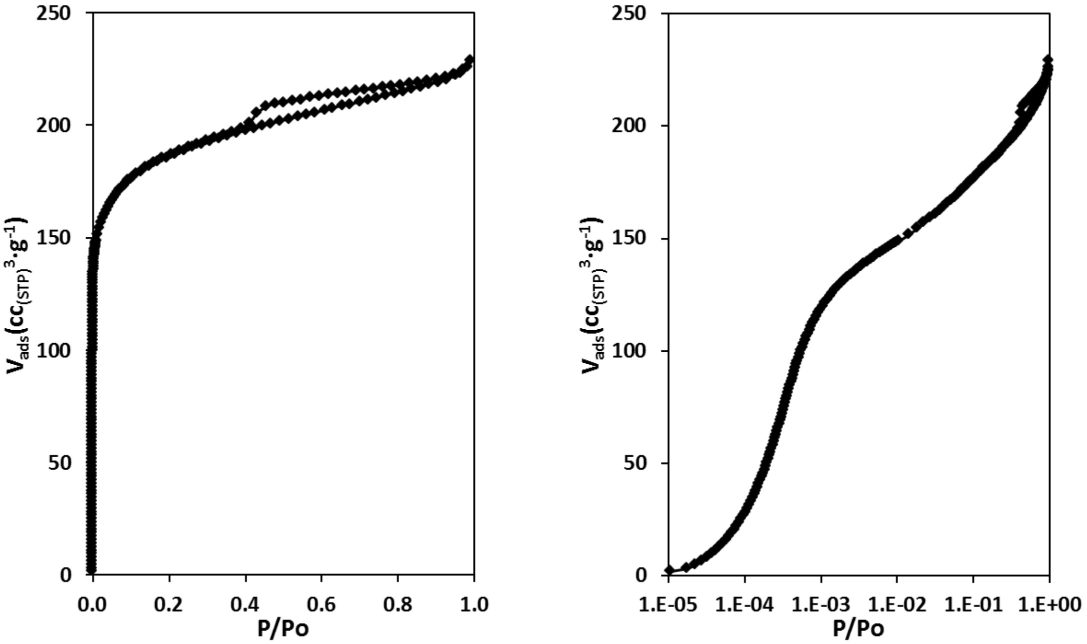

Figure A12 Ar adsorption isotherm (87 K) for Na-Sn-Beta-100.

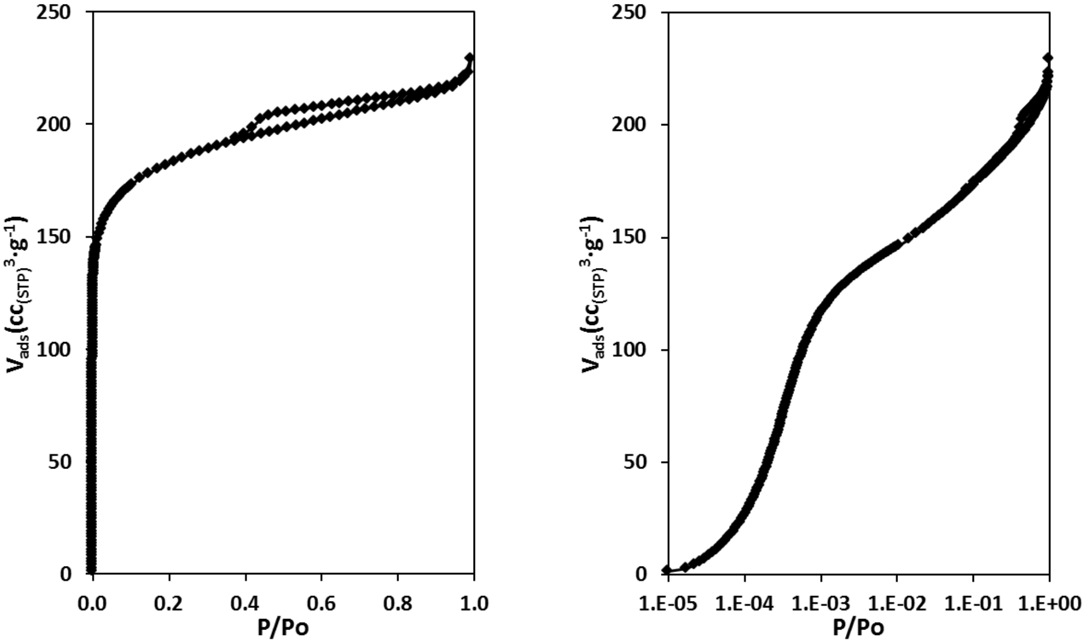

Figure A13 Ar adsorption isotherm (87 K) for Na-Sn-Beta-60.

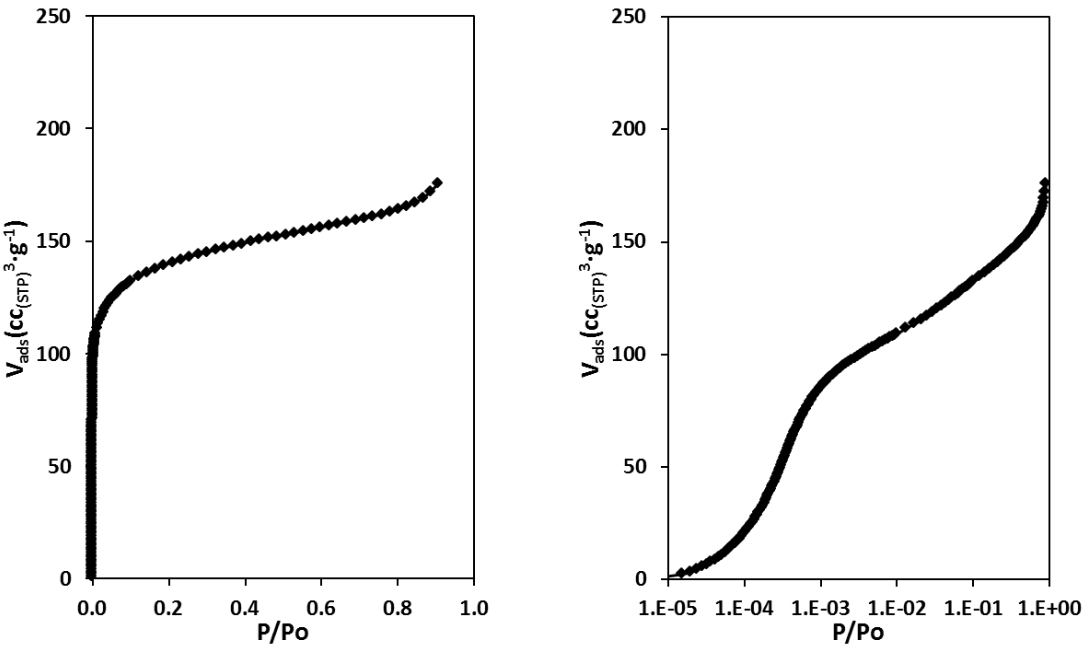

Figure A14 Ar adsorption isotherm (87 K) for Na-Sn-Beta-30.

A4. Infrared Spectroscopy

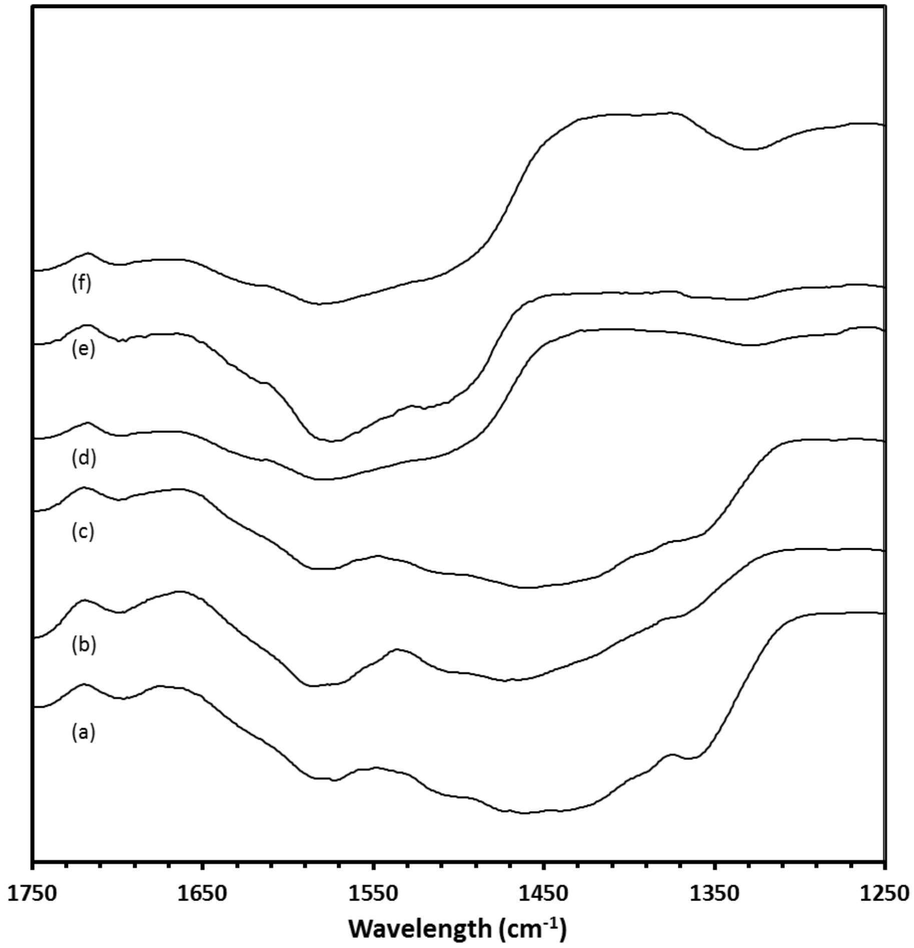

Figure A15 IR spectra of (a) Sn-Beta, (b) Sn-Beta-AW, (c) Sn-Beta-NH_3-Cal, (d) Sn-Beta-1Ex, (e) Sn-Beta-2Ex, and (f) Sn-Beta-3Ex showing the presence or absence of a broad nitrate ion absorption band in the 1300 cm^{-1} -1500 cm^{-1} range.[1]

(1) Miller, F. A.; Wilkins, C. H. *Anal. Chem.* **1952**, *24*, 1253–1294.

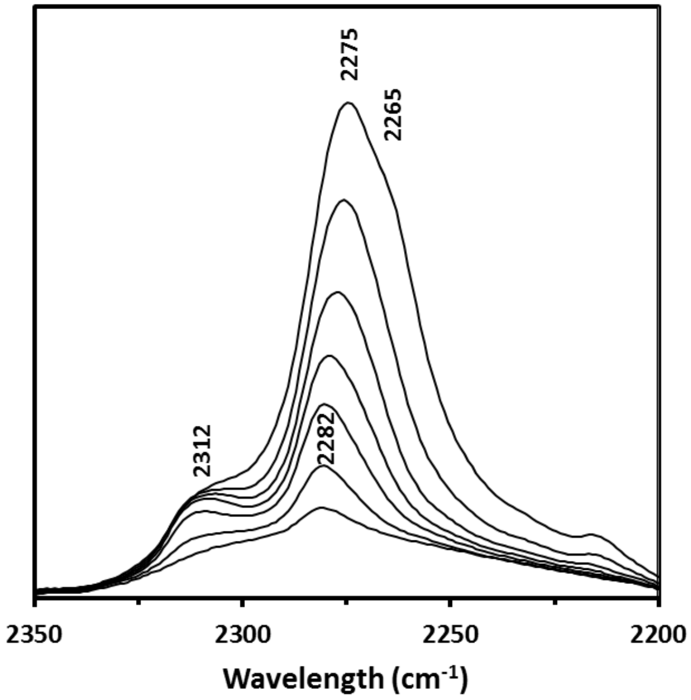

Figure A16 Baseline-corrected IR spectra with decreasing CD_3CN coverage on Sn-Beta-1Ex.

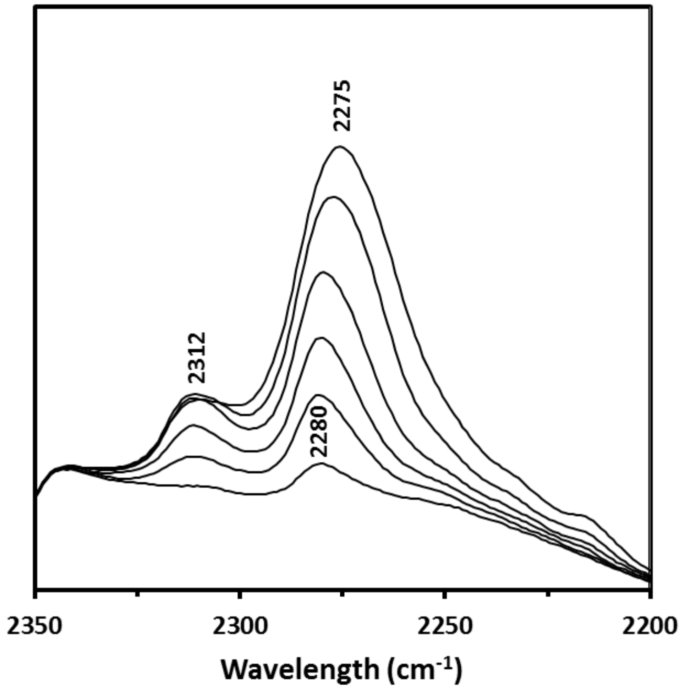

Figure A17 Baseline-corrected IR spectra with decreasing CD_3CN coverage on Sn-Beta-2Ex.

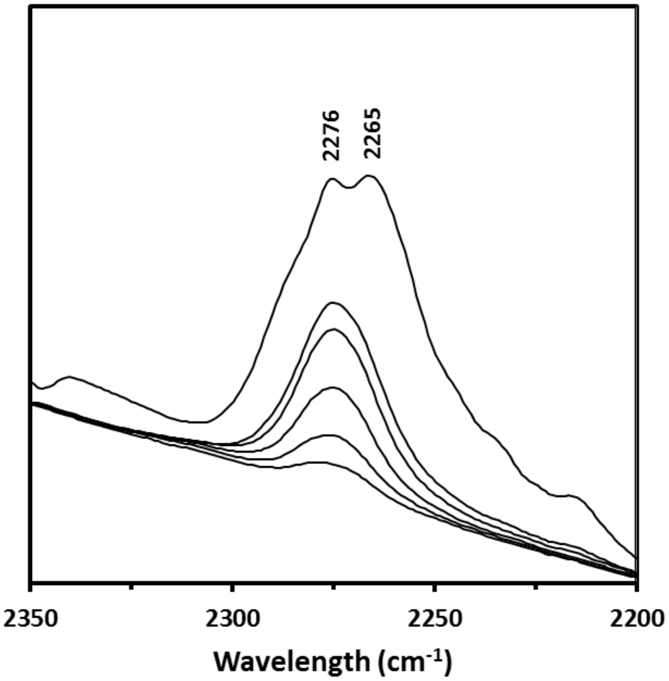

Figure A18 Baseline-corrected IR spectra with decreasing CD_3CN coverage on Si-Beta-3Ex.

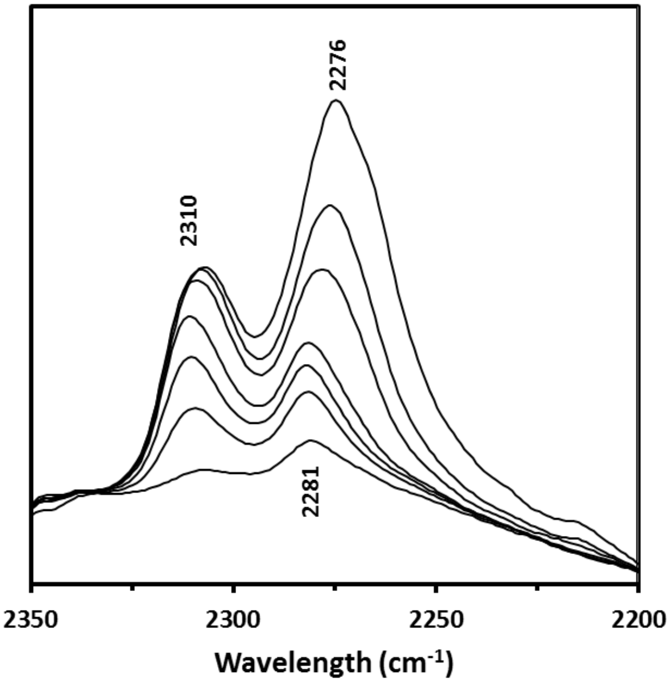

Figure A19 Baseline-corrected IR spectra with decreasing acetonitrile coverage on Na-Sn-Beta-30. This spectrum was collected after a 2h 773 K vacuum activation

A5. Solid-State Magic Angle Spinning Nuclear Magnetic Resonance (SS MAS NMR)

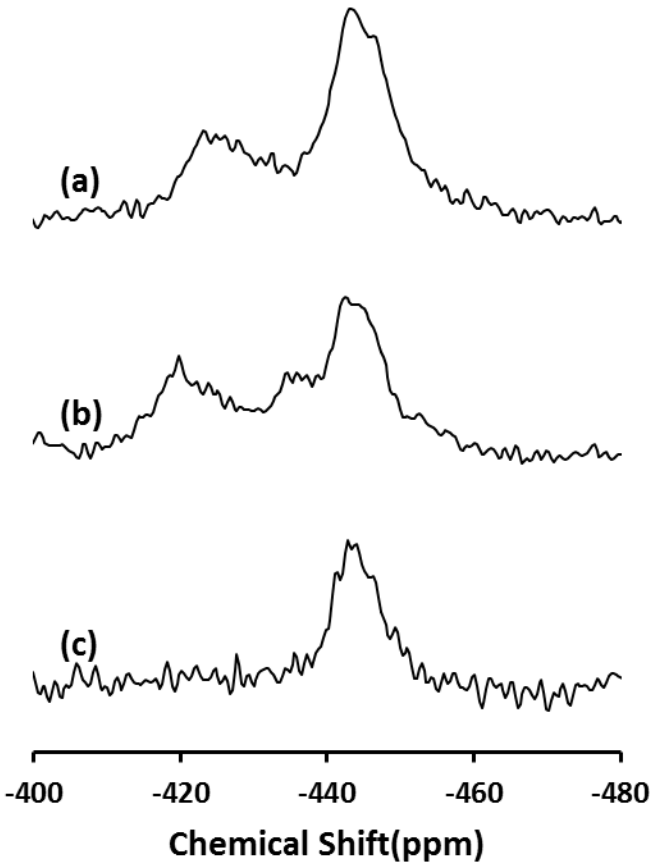

Figure A20 Expanded chemical shift range in the -400 to -480 ppm region of ^{119}Sn MAS Solid State NMR spectra of ^{119}Sn-Beta after different treatments: (a) dehydration after calcination, (b) dehydration after three Na-exchanges, and (c) dehydration after NH_3 adsorption.

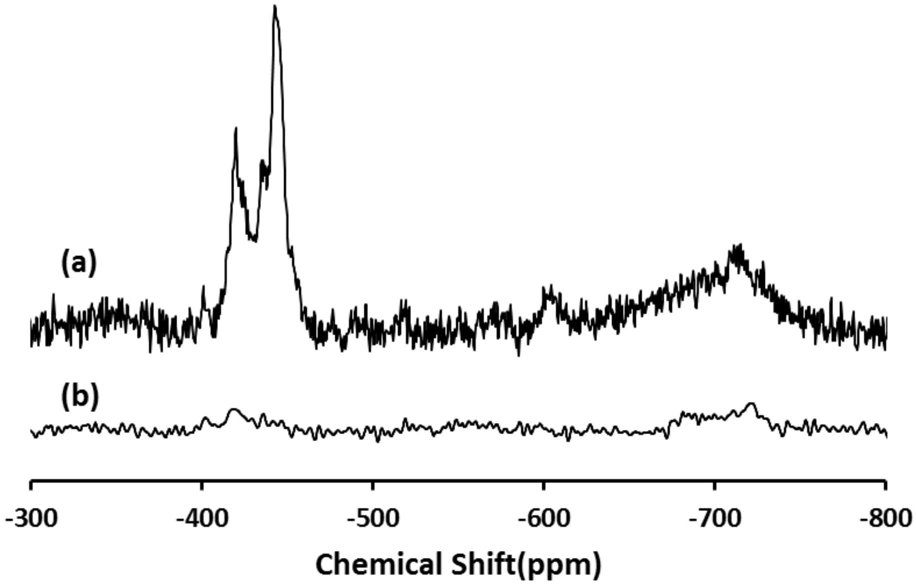

Figure A21 ^{119}Sn NMR of three times Na-exchanged ^{119}Sn-Beta dehydrated at 397 K for 2h: (a) MAS spectrum and (b) CPMAS spectrum with 2ms contact time.

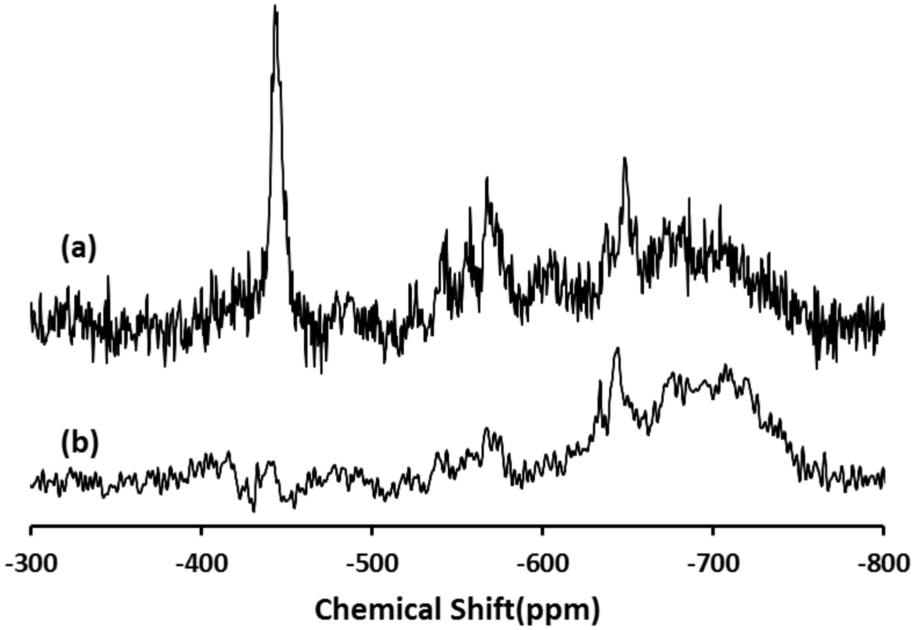

Figure A22 ^{119}Sn NMR of NH_3-dosed ^{119}Sn-Beta dehydrated at 397 K for 2h: (a) MAS spectrum and (b) CPMAS spectrum with 2ms contact time.

A6 Glucose conversion and fructose and mannose yields

Tables 2.2, 2.3, and 2.4 in Chapter 2 provide glucose conversion and fructose and mannose yields after 30 minutes of reaction. The following tables provide these data for 10 and 20 minutes time points.

Table A1 Glucose conversion (X) and fructose and mannose yields (Y) in H_2O and CH_3OH solvents.

		10 minutes			*20 minutes*		
Catalyst	**Solvent**	X_{Gluc} (%)	Y_{Fruc} (%)	Y_{Mann} (%)	X_{Gluc} (%)	Y_{Fruc} (%)	Y_{Mann} (%)
Sn-Beta	H_2O	1.0	1.0	0.0	3.4	2.9	0.4
	CH_3OH	12.0	4.8	0.0	20.4	9.1	1.8
Sn-Beta-1Ex	H_2O	2.9	0.0	1.0	3.6	0.8	1.6
	CH_3OH	8.9	0.0	2.3	10.6	2.8	3.6
Sn-Beta-2Ex	H_2O	2.2	0.0	0.8	4.9	0.0	2.4
	CH_3OH	7.9	0.0	2.4	10.5	0.0	4.4
Sn-Beta-3Ex	H_2O	4.4	0.0	1.3	5.8	0.0	3.2
	CH_3OH	8.2	0.0	2.7	11.7	0.0	5.0
Sn-Beta-AW	H_2O	2.4	0.0	0.0	3.8	2.3	0.0
	CH_3OH	9.9	2.2	2.2	12.1	4.7	2.7
Na-Sn-Beta-100	H_2O	2.8	0.0	1.5	4.1	2.9	1.1
	CH_3OH	9.2	3.2	2.1	14.0	6.3	2.7
Na-Sn-Beta-60	H_2O	1.8	0.0	1.3	4.3	2.5	1.9
	CH_3OH	8.1	2.7	2.7	13.3	6.2	2.7
Na-Sn-Beta-30	H_2O	3.0	0.0	2.2	3.1	0.0	2.9
	CH_3OH	5.1	0.0	2.5	5.1	0.0	3.6
Sn-Beta-NH_3	H_2O	0.0	0.0	0.0	2.3	0.0	2.0
	CH_3OH	2.7	0.0	1.4	2.7	0.0	1.5
Sn-Beta-NH_3-Cal	H_2O	1.7	0.0	0.0	2.8	1.7	0.0
	CH_3OH	11.0	2.5	1.7	14.8	5.0	2.5

Reaction conditions: 1% (w/w) glucose solutions, 1:100 metal:glucose ratio, 353 K, 10 and 20 min.

Table A2 Glucose conversion (X) and fructose and mannose yields (Y) with 0.2g NaCl/g H_2O.

Catalyst	**Solvent**	*10 minutes*			*20 minutes*		
		X_{Gluc} (%)	Y_{Fruc} (%)	Y_{Mann} (%)	X_{Gluc} (%)	Y_{Fruc} (%)	Y_{Mann} (%)
Sn-Beta	H_2O-NaCl	5.1	1.9	2.1	9.6	3.4	3.2
Sn-Beta-1Ex	H_2O-NaCl	3.5	0.0	3.0	6.3	1.5	4.4
Sn-Beta-2Ex	H_2O-NaCl	4.0	0.0	3.0	5.8	1.4	5.0
Sn-Beta-3Ex	H_2O-NaCl	3.7	0.0	3.6	9.6	0.0	6.4

Reaction conditions: 1% (w/w) glucose solutions, 1:100 metal:glucose ratio, 353 K, 10 and 20 min.

Appendix B: Supplementary Information for Chapter 3

B1. Product identification by fractionation and NMR

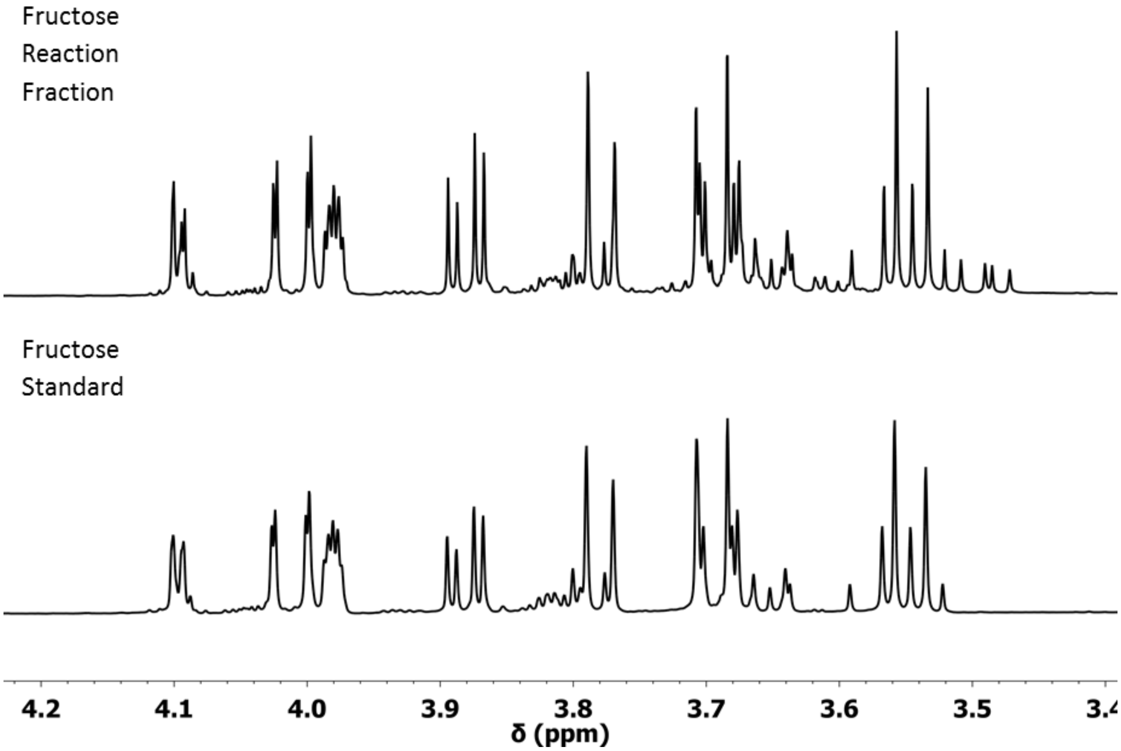

Figure B1 ^{1}H NMR spectra of D-fructose standard solution (bottom) and of the fructose-containing fraction (top) isolated after reaction of D-fructose with MoO_3 in water at 100 ^{0}C for 4 h. Sorbose is present in the collected fraction.

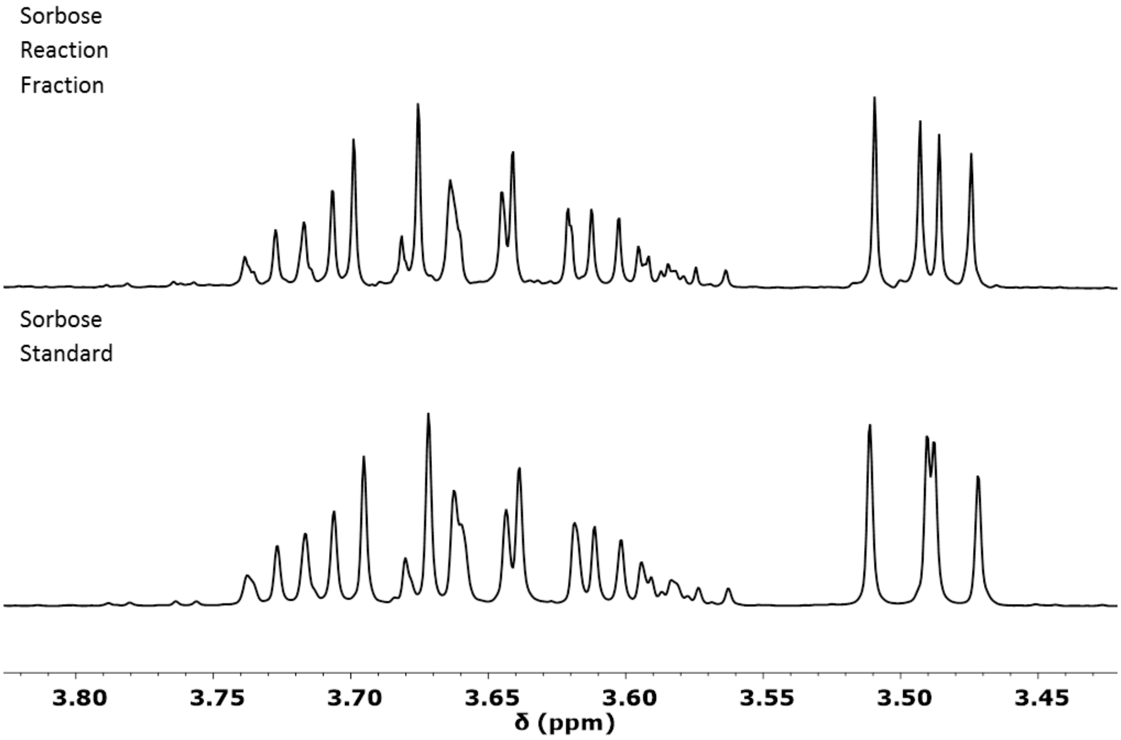

Figure B2 ^{1}H NMR spectra of L-sorbose standard solution (bottom) and of the sorbose-containing fraction (top) isolated after reaction of D-fructose with MoO_3 in water at 100 ^{0}C for 4 h.

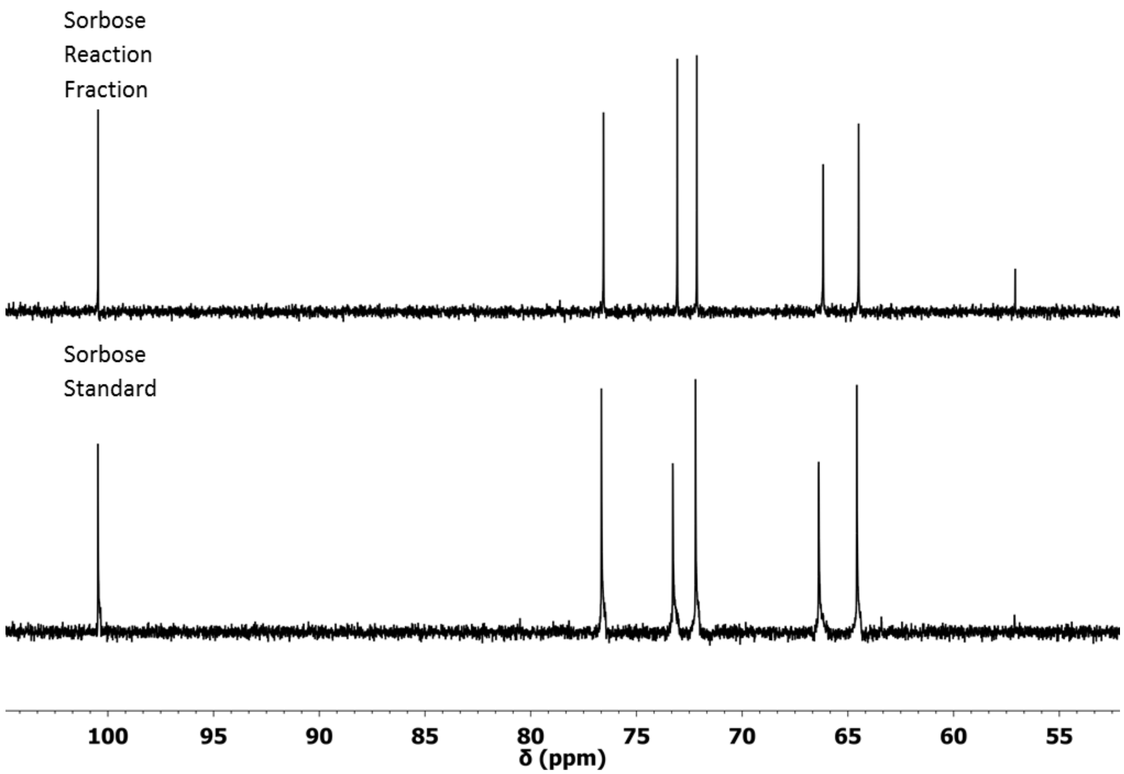

Figure B3 ^{13}C NMR spectra of L-sorbose standard solution (bottom) and of the sorbose-containing fraction (top) isolated after reaction of D-fructose with MoO_3 in water at 100 ^{0}C for 4 h.

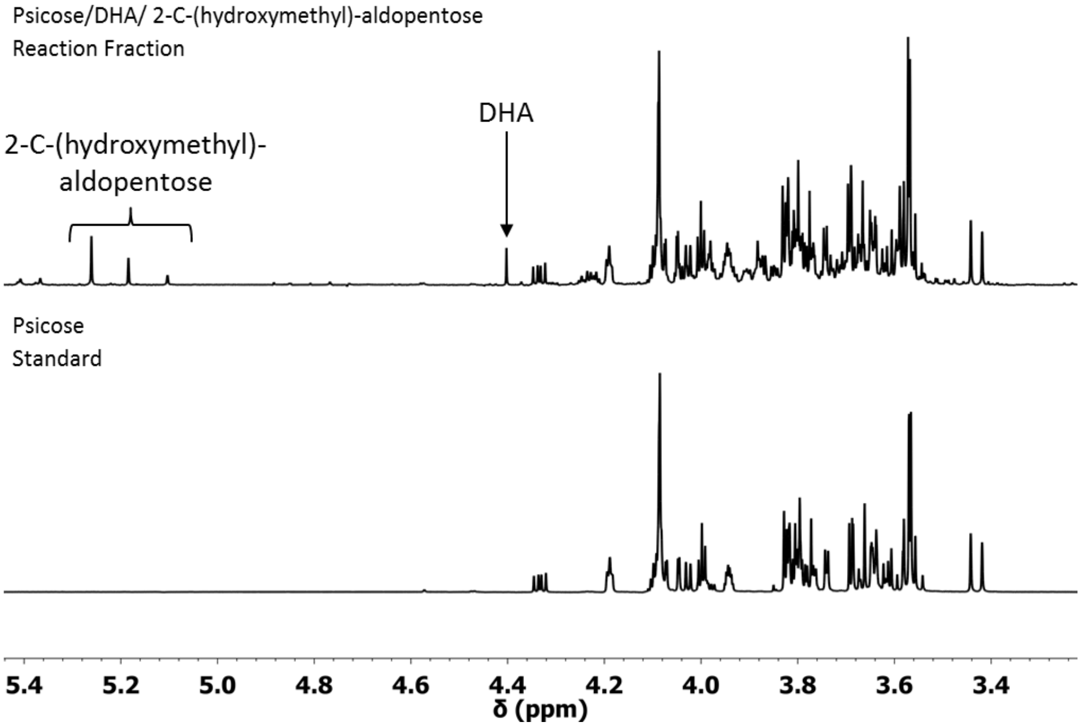

Figure B4 ^{1}H NMR spectra of D-psicose standard solution (bottom) and of the psicose-containing fraction (top) isolated after reaction of D-fructose with MoO_3 in water at 100 ^{0}C for 4 h. DHA and a 2-*C*-(hydroxymethyl)-aldopentose are present in the collected fraction. HDO peak ca. 4.8 ppm is digitally suppressed for clarity.

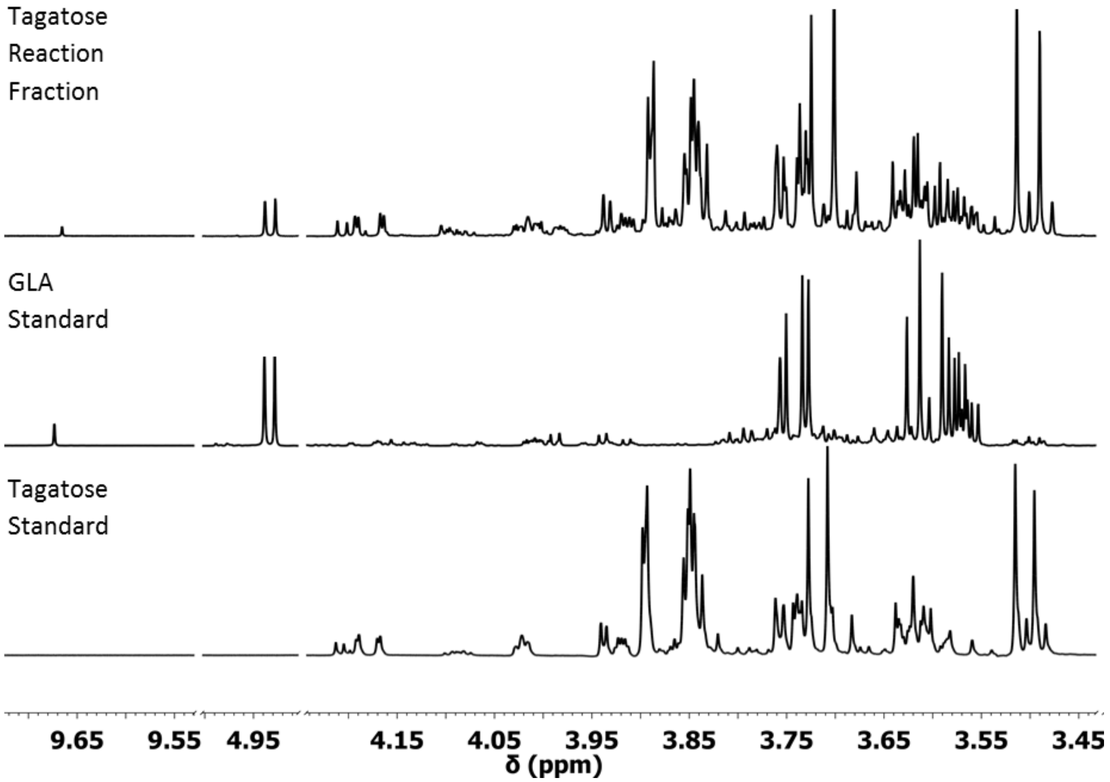

Figure B5 ^{1}H NMR spectra of D-tagatose and GLA standard solutions (bottom and middle, respectively) and of the tagatose-containing fraction (top) isolated after reaction of D-fructose with MoO_3 in water at 100 ^{0}C for 4 h. Glyceraldehyde is present in the collected fraction.

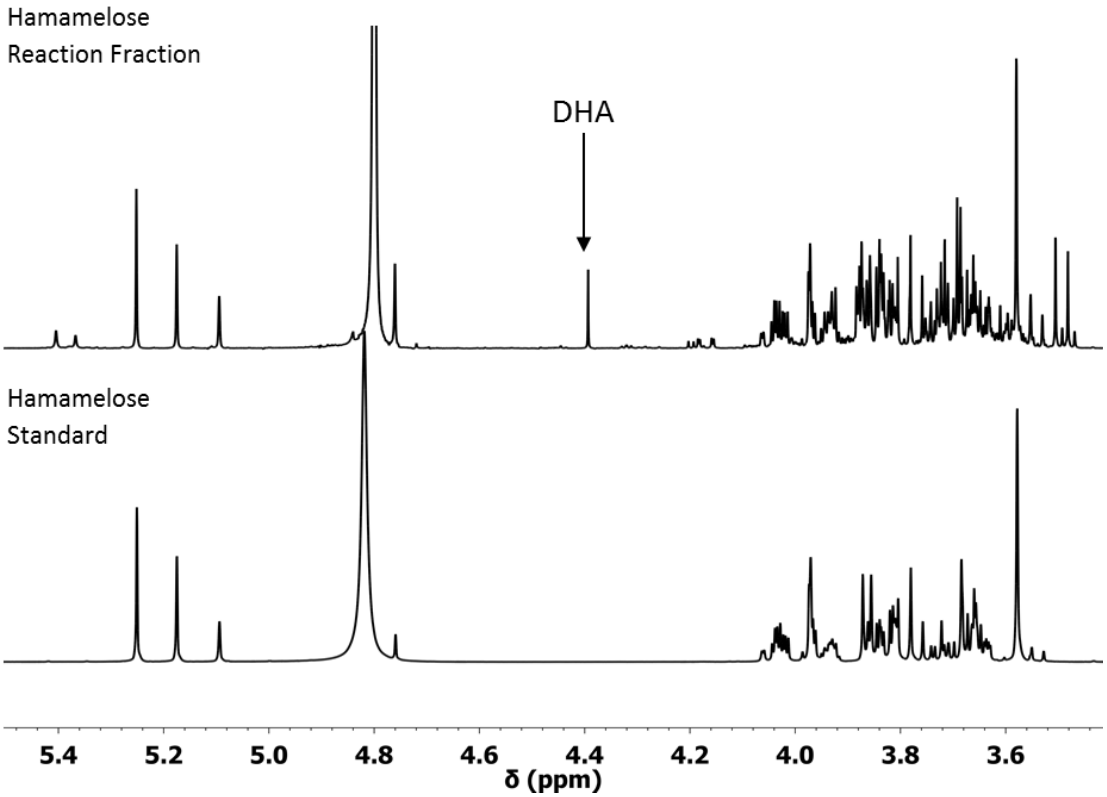

Figure B6 ^{1}H NMR spectra of D-Hamamelose standard solution (bottom) and of the hamamelose-containing fraction (top) isolated after reaction of D-fructose with MoO_3 in water at 100 ^{0}C for 4 h. DHA and an unknown are present in the collected fraction.

B2. ^{1}H NMR evidence of lactate production by combination of MoO_3 and Sn-MFI

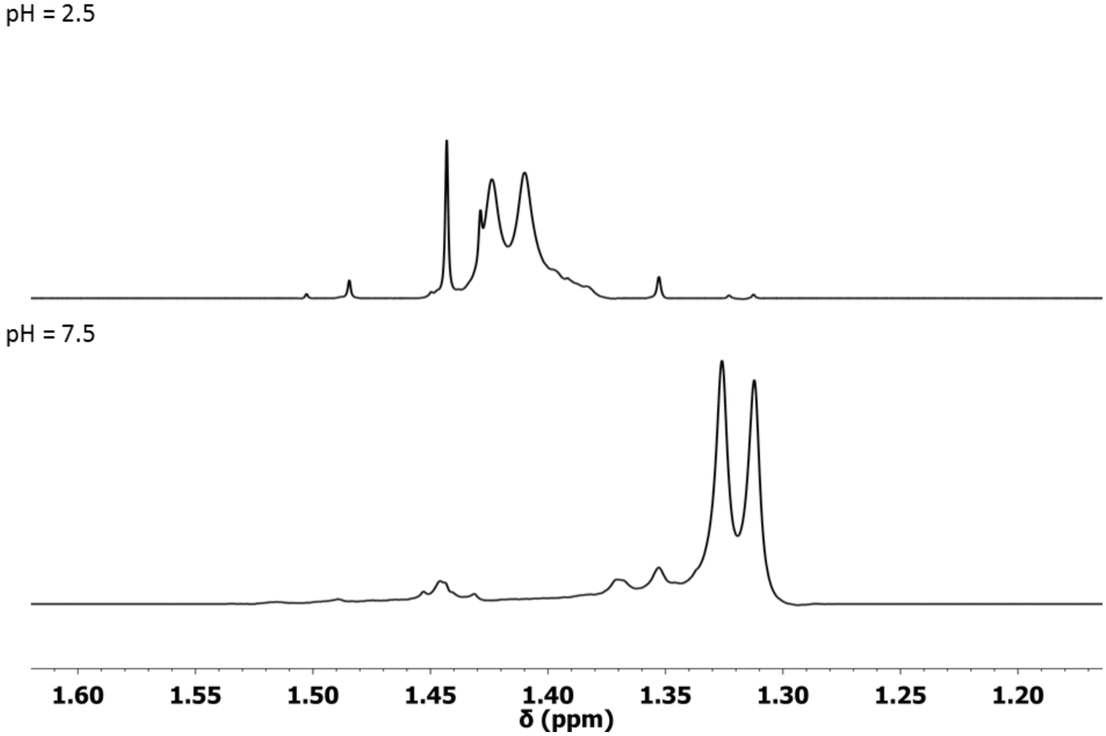

Figure B7 ^{1}H NMR spectra of methyl group in molybdate-lactate complex formed in the reaction of D-fructose with MoO_3 and Sn-MFI in water at 100 ^{0}C for 16 h (ca. 25% yield). Top spectrum (pH =2.5) is of a reaction aliquot prior to pH adjustment to 7.5 (bottom spectrum) by addition of sodium bicarbonate.

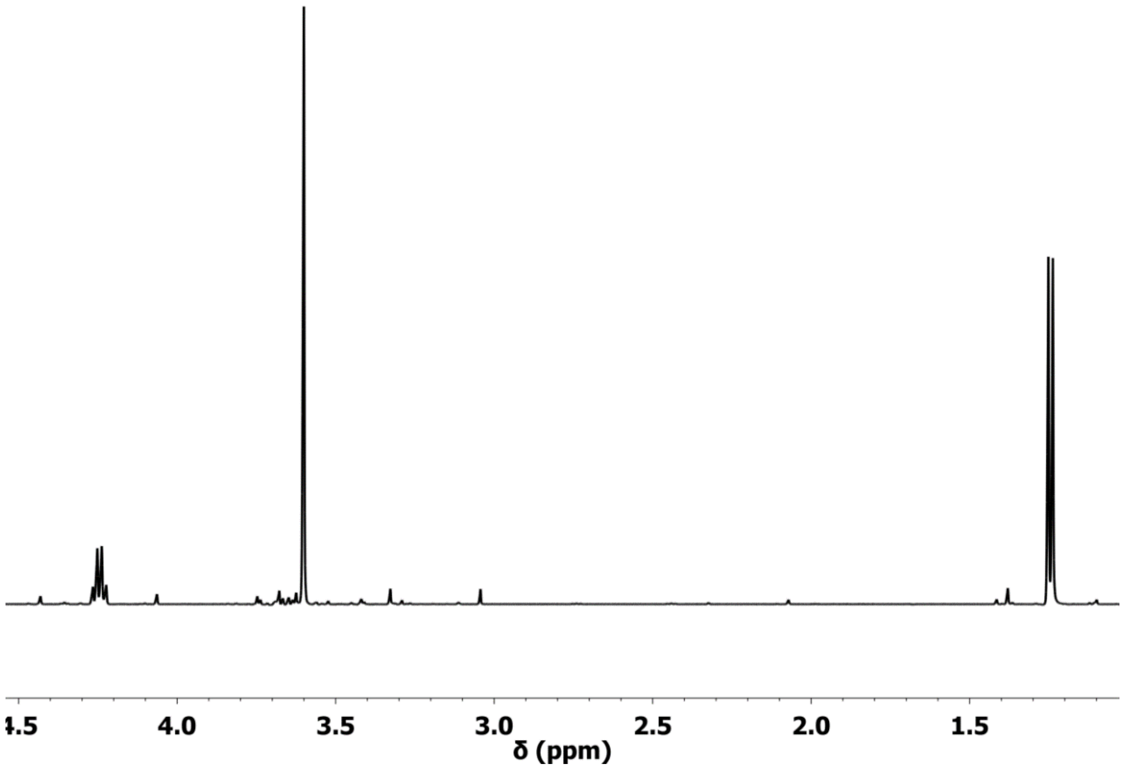

Figure B8 ^{1}H NMR spectra of reaction solution of D-fructose with MoO_3 and Sn-MFI in MeOH at 100 ^{0}C for 30 h (ca. 68% methyl lactate yield) showing the three intense resonances of methyl lactate (ca. 1.25, 3.60, and 4.25 ppm) and small peaks associated with by-products. MeOH peak ca. 3.19 ppm is digitally suppressed for clarity.

B3. Reaction profiles for tandem reactions

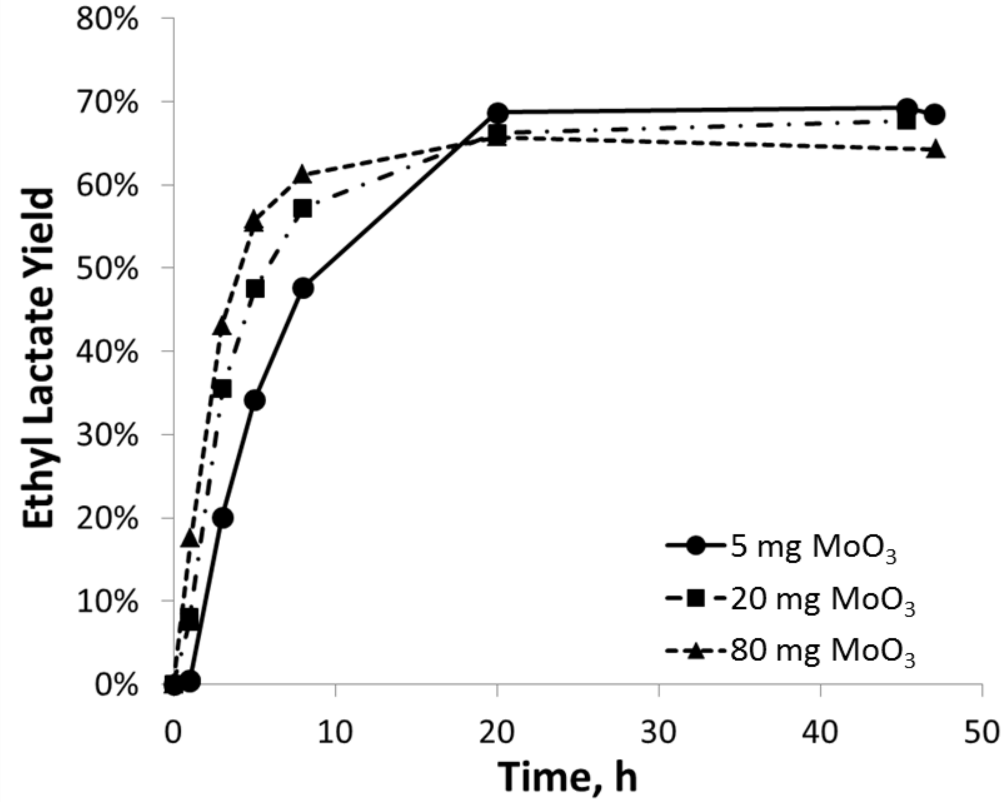

Figure B9 Ethyl lactate yield as a function of time for varying MoO_3 catalyst amounts (indicated in legend). Reaction conditions: 100 ^{0}C; 100 mg Sn-MFI; 50 mg D-fructose; 4.9 g EtOH; 50 mg naphthalene as internal standard.

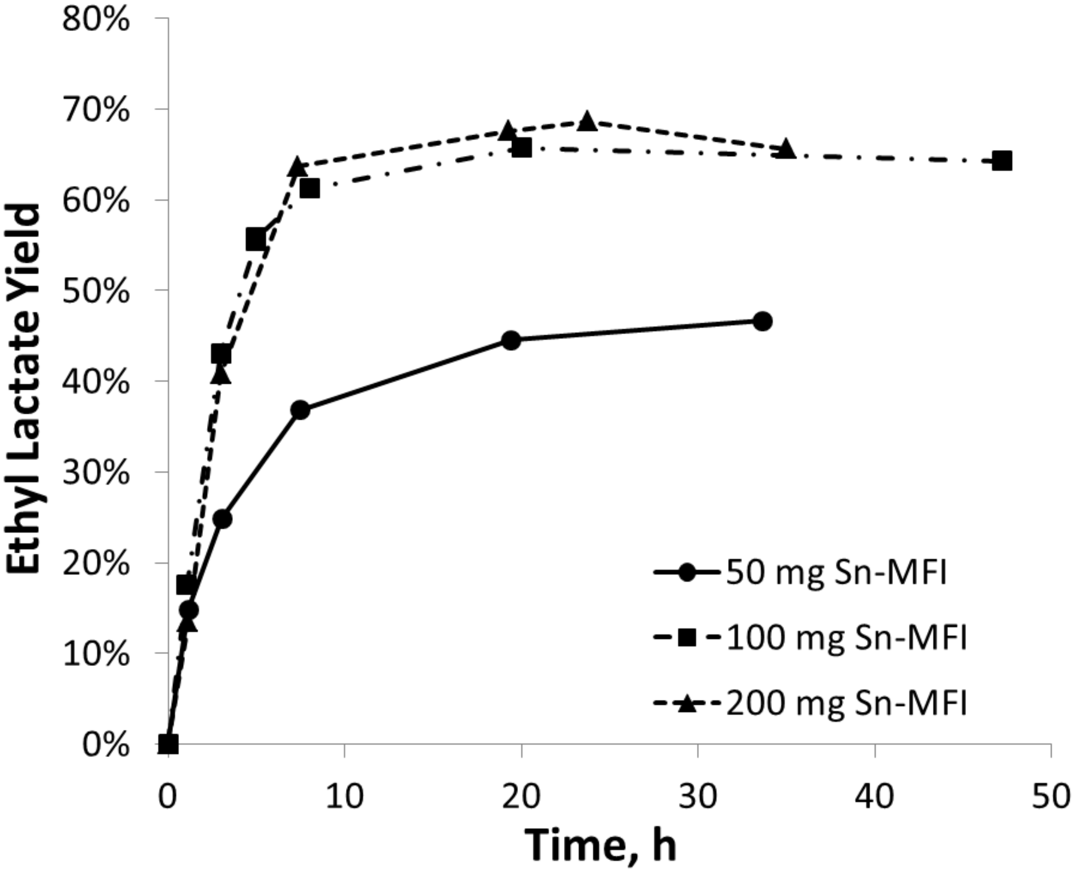

Figure B10 Ethyl lactate yield as a function of time for varying Sn-MFI catalyst amounts (indicated in legend). Reaction conditions: 100 ^{0}C; 80 mg MoO_3; 50 mg D-fructose; 4.9 g EtOH; 50 mg naphthalene as internal standard.

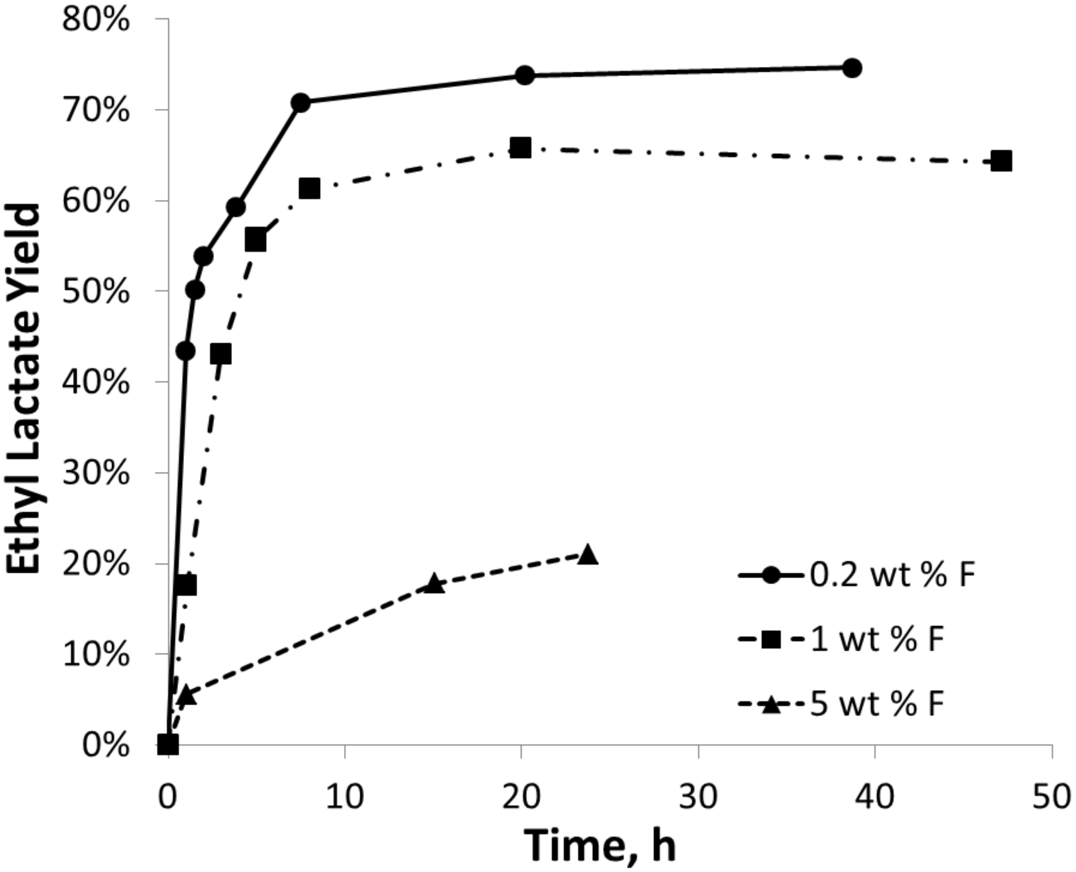

Figure B11 Ethyl lactate yield as a function of time for varying concentrations of fructose (indicated in legend). Reaction conditions: 100 ^{0}C; 80 mg MoO_3; 100 mg Sn-MFI; 4.9 g EtOH; 50 mg naphthalene as internal standard.

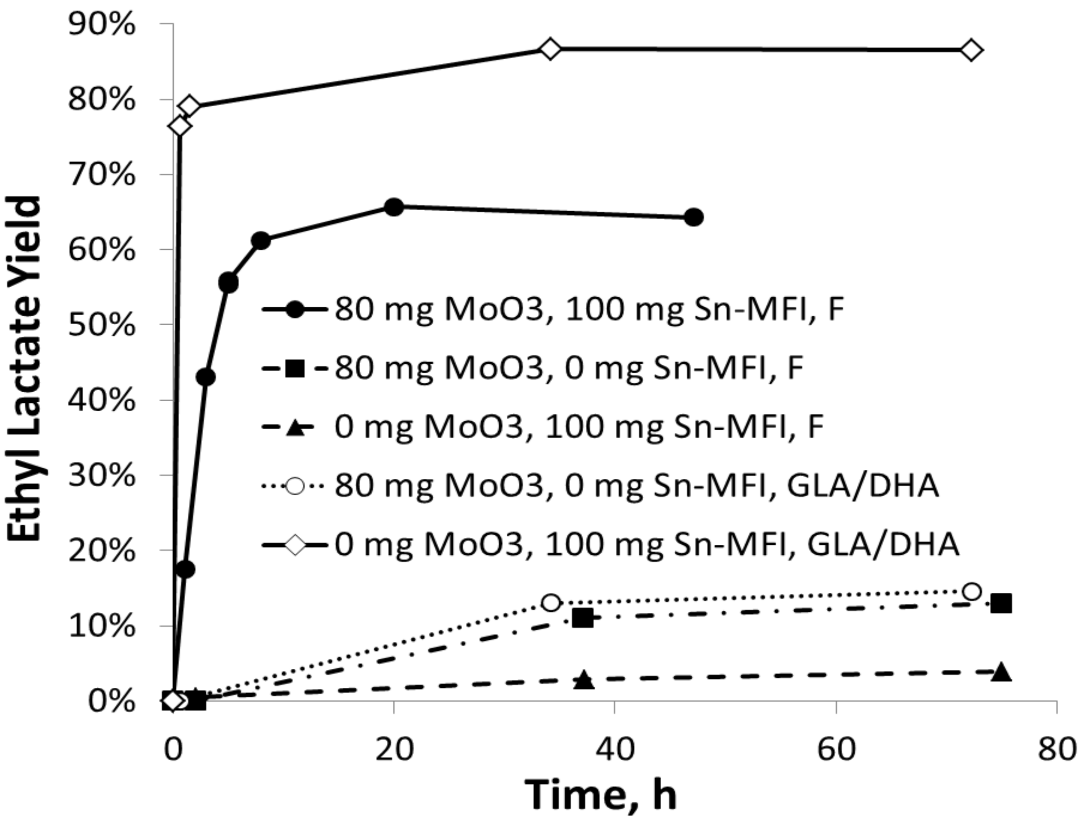

Figure B12 Ethyl lactate yield as a function of time for control runs illustrating the necessity of catalyst. Reaction conditions: 100 ^{0}C; catalyst amounts specified in legend; 50 mg of D-fructose (F) or mixture of 25 mg of GLA and 25 mg DHA (GLA/DHA) 4.9 g EtOH; 50 mg naphthalene as internal standard.

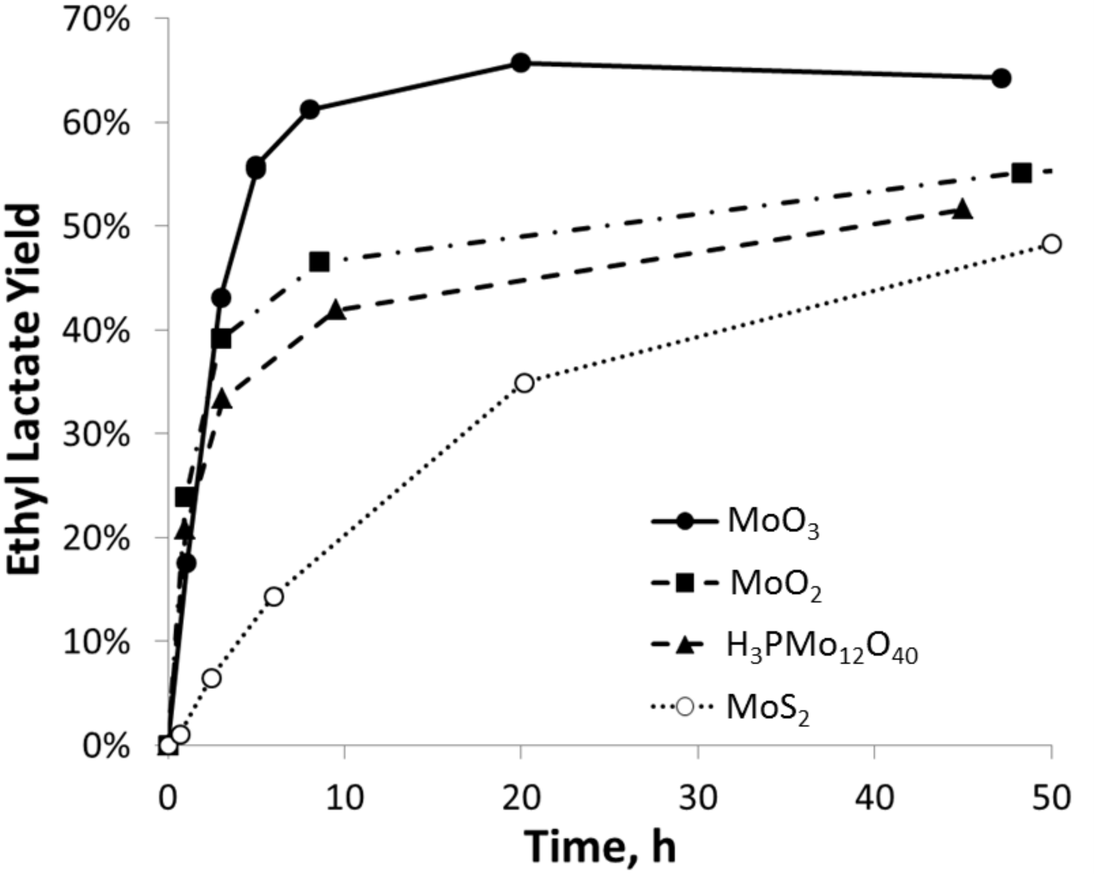

Figure B13 Ethyl lactate yield as a function of time for varying Mo-containing retro-aldol catalysts (indicated in legend). Reaction conditions: 100 ^{0}C; 100 mg Sn-MFI; 50 mg D-fructose; 4.9 g EtOH; 50 mg naphthalene as internal standard.

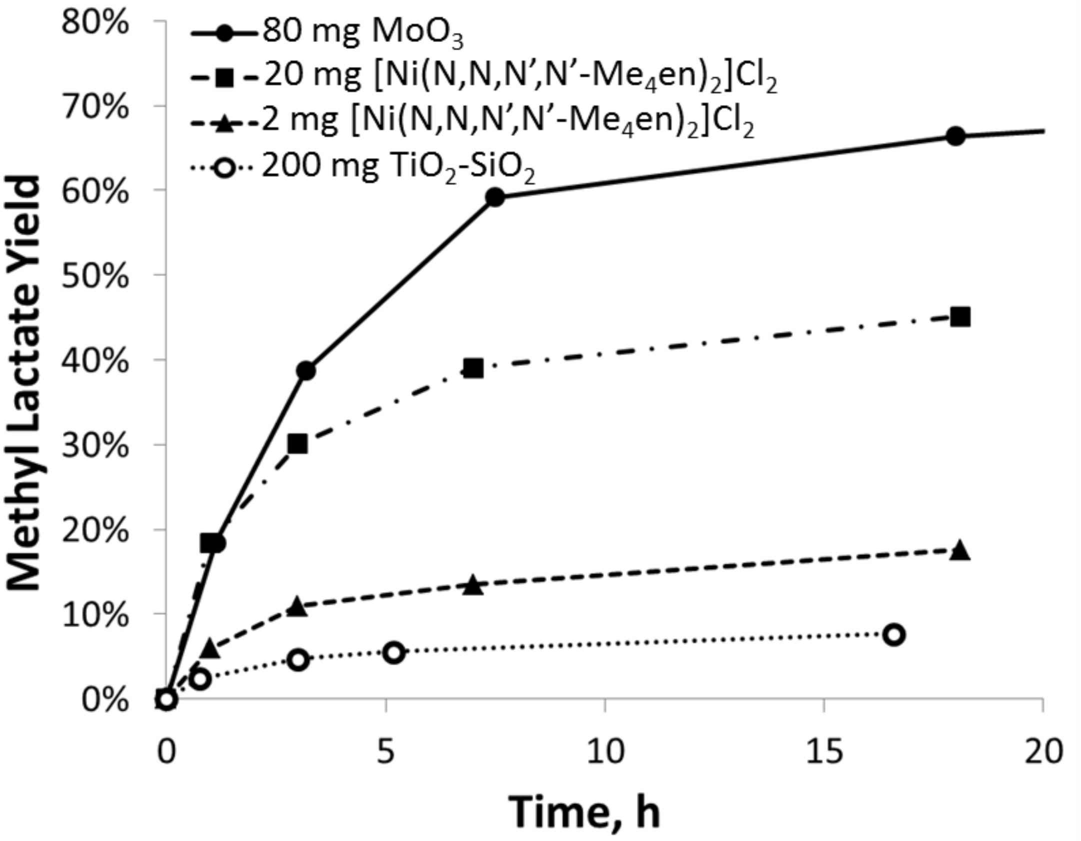

Figure B14 Methyl lactate yield as a function of time for MoO_3 and [Ni(N,N,N',N'-Me_4en)$_2$]Cl_2 catalysts (amounts indicated in legend). Reaction conditions: 100 ^{0}C; 100 mg Sn-MFI; 50 mg D-fructose; 4.9 g MeOH; 50 mg naphthalene as internal standard.

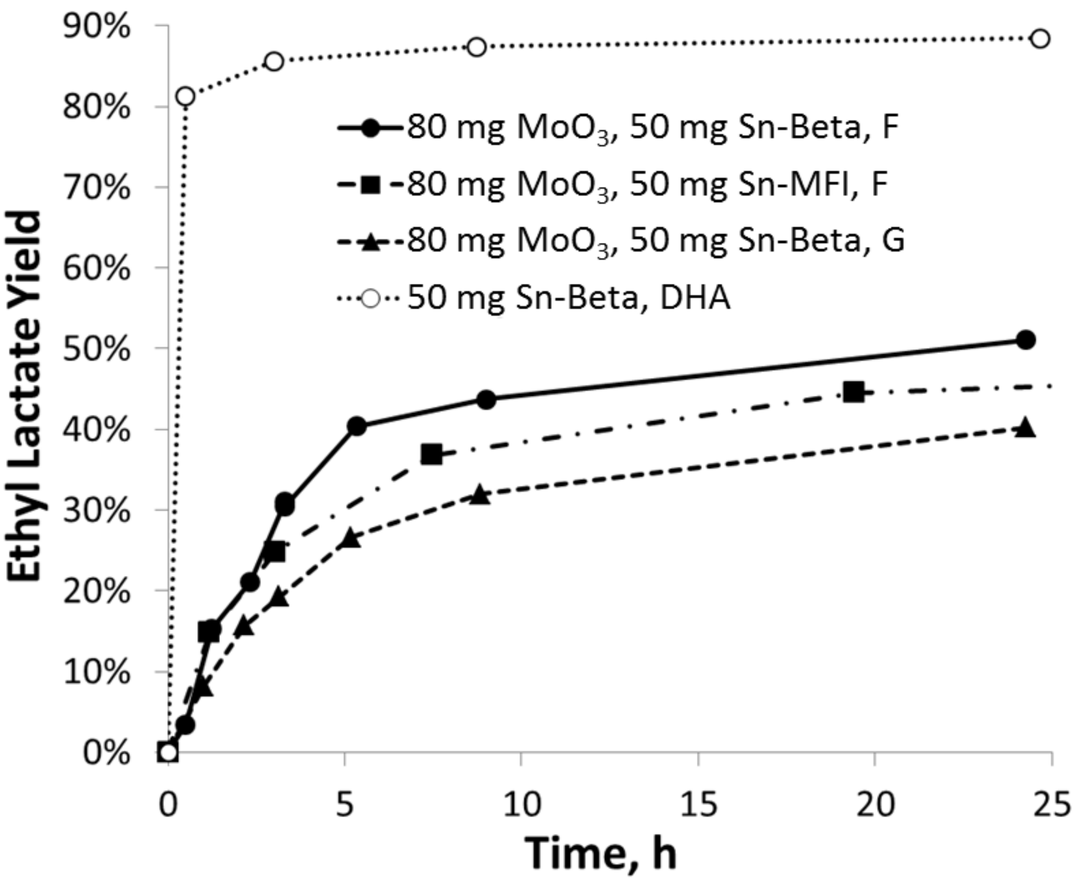

Figure B15 Ethyl lactate yield as a function of time for Sn-Beta/Sn-MFI comparison. Reaction conditions: 100 ^{0}C; 80 mg MoO_3; Sn-Beta or Sn-MFI amount specified in legend; 50 mg of D-fructose (F), D-Glucose (G), or DHA; 4.9 g EtOH; 50 mg naphthalene as internal standard.

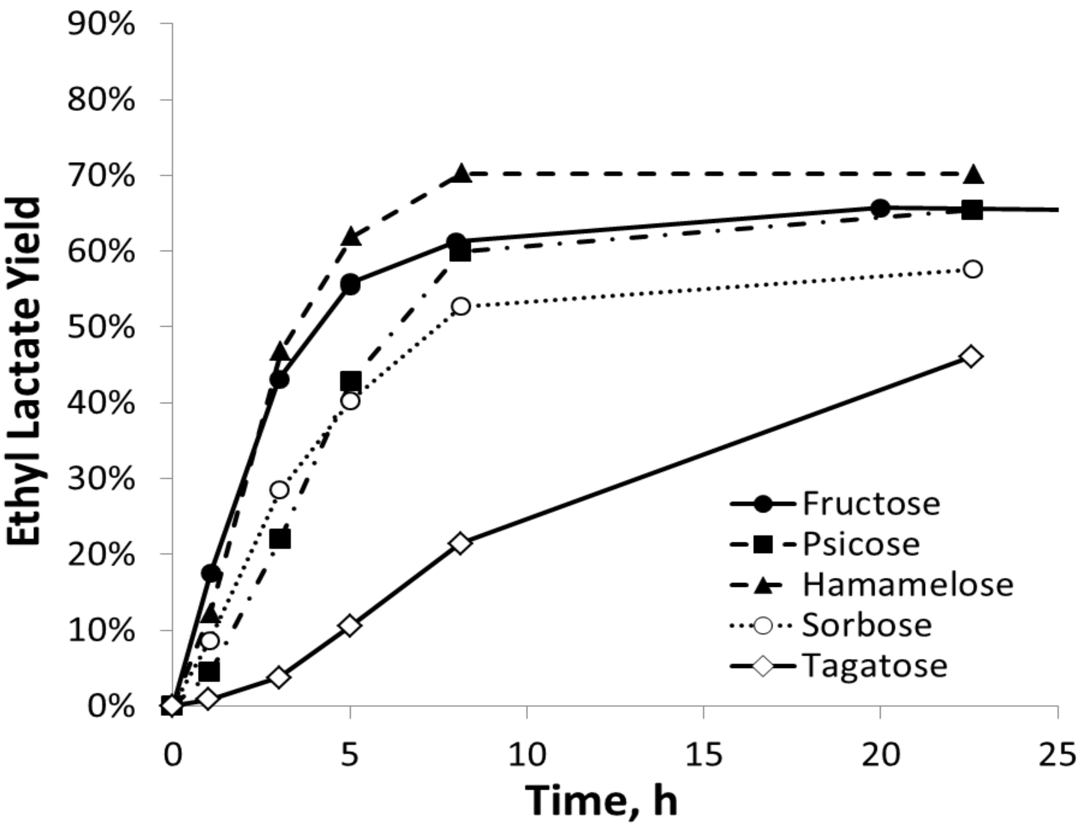

Figure B16 Ethyl lactate yield as a function of time for different ketohexoses and a 2-C-(hydroxymethyl)-aldopentoses (hamamelose) as substrates. Reaction conditions: 100 ^{0}C; 80 mg MoO_3; 100 mg Sn-MFI; 50 mg of D-fructose, D-psicose, D-hamamelose, L-sorbose, or D-tagatose; 4.9 g EtOH; 50 mg naphthalene as internal standard.

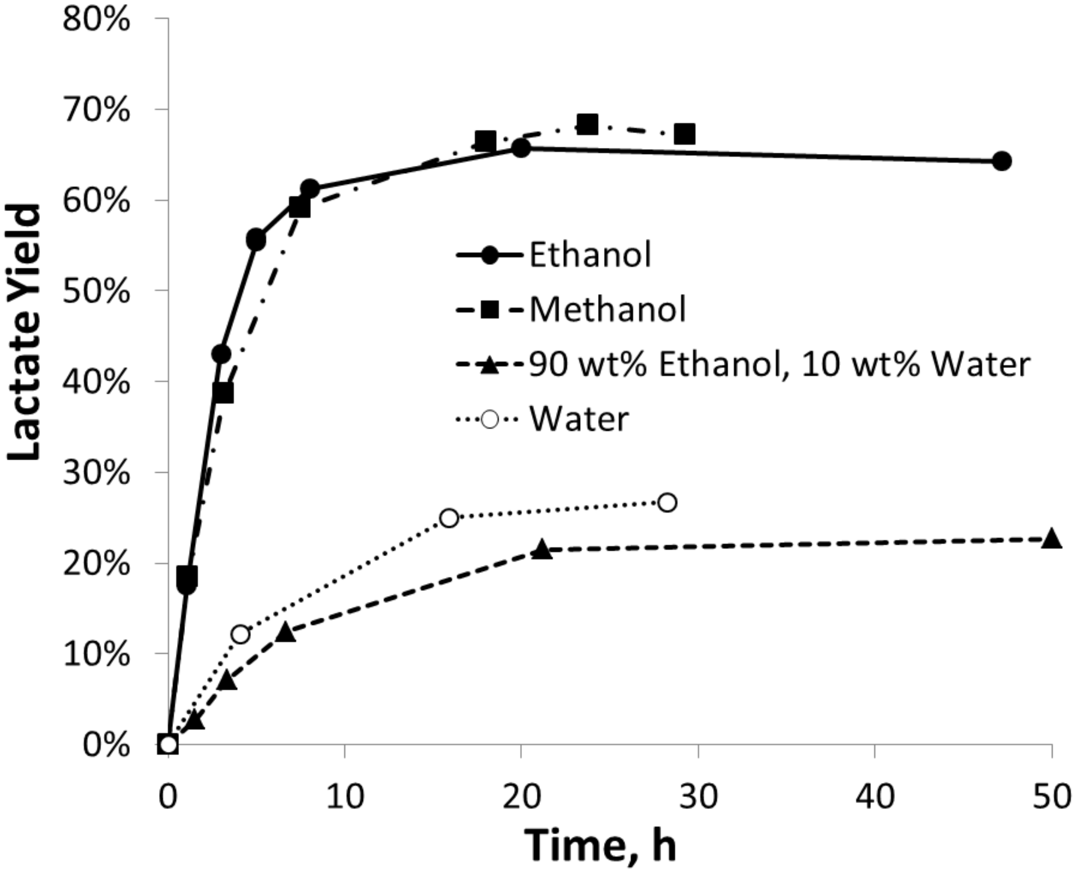

Figure B17 Lactate yield as a function of time for different solvents (specified in legend): 100 ^{0}C; 80 mg MoO_3; 100 mg Sn-MFI, 50 mg of D-fructose (F); 4.9 g solvent; 50 mg naphthalene as internal standard. In case of water, external standard (DSS) was used for ^{1}H NMR quantification instead of naphthalene.